The Dissertation Committee for Stephen Edward Fosdick certifies that this is the approved version of the following dissertation:

Bipolar Electrodes for the Screening of Electrocatalyst Candidates

Committee:

Richard M. Crooks, Supervisor

Allen J. Bard

Arumugam Manthiram

C. Buddie Mullins

Keith J. Stevenson

Bipolar Electrodes for the Screening of Electrocatalyst Candidates

by

Stephen Edward Fosdick, B.S.

Dissertation

Presented to the Faculty of the Graduate School of

The University of Texas at Austin

in Partial Fulfillment

of the Requirements

for the Degree of

Doctor of Philosophy

The University of Texas at Austin

May 2014

Dedication

To my parents, Larry and Marla,

and my fiancée, Christina.

Acknowledgements

I wish to thank my research advisor, Prof. Richard M. Crooks, for his guidance and support over the past few years. His direction and leadership made it possible for me to achieve the work presented here and have shaped my abilities as a scientist.

I would like to thank my committee members, Prof. Allen J. Bard, Prof. Arumugam Manthiram, Prof. C. Buddie Mullins, and Prof. Keith J. Stevenson for their counsel and assistance during my graduate career.

My group members have greatly aided me during my studies. I would like to thank Dr. Kwok-Fan Chow, Dr. Ioana Dumistrescu, and Dr. Brian Zaccheo for helping me during my first years in the group. I thank Kyle Knust, Morgan Anderson, and James Loussaert for the deluge of ideas during our brainstorming sessions. I also thank my collaborator, Dr. Sean Berglund, for all of his help and humor.

I thank my father, Larry, who always encouraged my curiosity and has supported me in all my endeavors. I thank my mother, Marla, who I miss greatly and who will continue to guide me. And finally, I thank my fiancée and best friend, Christina, who always laughs at my jokes and keeps me sane.

Bipolar Electrodes for the Screening of Electrocatalyst Candidates

Stephen Edward Fosdick, Ph.D.

The University of Texas at Austin, 2014

Supervisor: Richard M. Crooks

Advances in the application of bipolar electrodes (BPEs) for screening of electrocatalysts, localized activation of a single conductive electrode, the optical tracking of single particles interacting with an active electrode, and the introduction of microwires in paper-based analytical devices are described.

In an original proof of concept study arrays of BPEs were used to determine the relative activity of model nanoparticle systems for the oxygen reduction reaction (ORR) by a simple optical readout: the electrodissolution of Ag microbands. The number of bands that dissolved during the screening procedure determined the relative activity of the materials. These screening results for model nanoparticle systems were related to traditional electrochemical experiments and showed a strong correlation.

Building on that initial study, the BPE platform for screening ORR electrocatalyst candidates was improved so

that more materials could be evaluated simultaneously by increasing the density of electrodes in the array, controlled compositional variations were prepared with the implementation of piezodispensing, and a different reporter, Cr, replaced Ag at the BPE anodes which reduced the risk of contamination and improved reliability of screening experiments. Further studies into the versatility of the screening platform have been carried out using non-noble metal systems for the hydrogen evolution reaction (HER), which has a long history of interest for electrochemists.

A single conductive electrode material can be made to act as an array of electrodes by confining it at the intersection of two orthogonal microfluidic channels. By manipulating the direction and magnitude of the electric field in the device, faradaic reactions can be selectively localized on the BPE.

An approach for optically tracking individual, insulating microparticles interacting with an active UME has been achieved. This approach brings new insight and understanding of single particle electrochemical studies.

Finally, a method for incorporating microwires and mesh electrodes into paper-based electroanalytical devices is reported. This has many advantages over traditional screen-printed carbon electrodes that are traditionally used in paper-based devices.

Table of Contents

List of Figures

List of Illustrations

Chapter 1: Introduction

1.1 History and Examples of Bipolar Electrochemistry

The properties of bipolar electrochemistry offer many interesting and unique advantages to many disciplines of science. These include the difficulty of making direct electrical contact to nanoscale electrodes, maintaining control over and reading out very large arrays of electrodes simultaneously, controlling electrodes that are mobile in solution, maintaining a non-uniform potential difference over the surface of an electrode, and using electrodes to control local solution potentials. This dissertation will focus on the use of bipolar electrodes (BPEs) in sensing and screening applications.

Scheme 1.1 shows a typical experimental configuration used for carrying out bipolar electrochemistry. Here, the driving electrodes apply a uniform electric field across the electrolyte solution, and the resulting faradaic electrochemical reactions at the BPE are shown occurring at the anodic (blue arrow) and cathodic (red arrow) poles of the BPE. As discussed later, the interfacial potential difference between the solution and BPE is highest at the ends of the electrode, so faradaic processes are always observed there first.

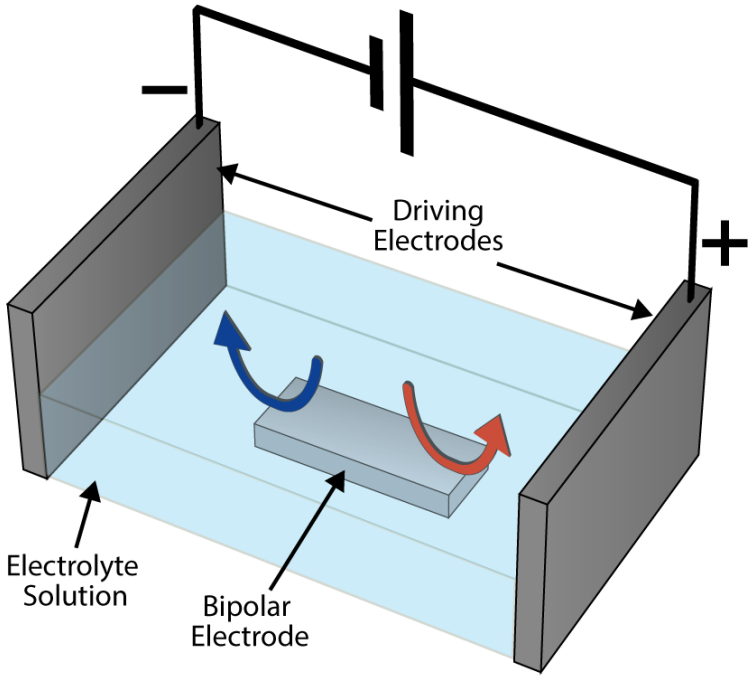

Scheme 1.1. Schematic illustration of a simple bipolar electrochemical cell.

Consider the following simple thought experiment based on the electrochemical cell shown in Scheme 1.1, a Pt BPE, and an aqueous solution containing a dilute, inert electrolyte. When the power supply is turned on to, for example, 1 V, no faradaic reactions are observed at either the driving electrodes or the BPE. However, at a critical voltage that depends on a number of experimental factors, bubbles are observed at the poles of the BPE. Analysis would show that those at the cathodic pole are hydrogen and those at the anodic pole are oxygen. In other words, even though the BPE is an equipotential surface (or nearly so), the electrolysis of water is occurring at its two poles. Importantly, charge must be conserved at the BPE, and therefore the rates of formation of $½O_2$ and H_2 are the same. Faradaic reactions might also occur at the driving electrodes, but although this is usually a nuisance it does not directly affect the BPE. I wish to emphasize that this is an oversimplified view of bipolar electrochemistry and more details will be introduced in later chapters and sections.

The main focus of this dissertation is on interesting fundamentals and applications of bipolar electrochemistry that have emerged since about the year 2000, but it is important to note that bipolar electrochemistry has been around for many years. Beginning in the 1960s, Fleischmann,

Goodridge, Wright, and co-workers described fluidized bed electrodes, where a voltage applied between two driving electrodes enables electrochemical reactions at discrete conductive particles.[1-6] Since these early studies, bipolar fluidized bed electrodes have been used in applications ranging from improving the efficiency of electrosyntheses,[7-9] photoelectrochemical cells,[10,11] and even batteries.[12] Bipolar plate technology is critical for polymeric-electrolyte-membrane (PEM) fuel cells where the plates form a series of BPEs.[13,14] Additionally, neuronal behavior can also be mimicked using short-circuited microbands which act as a BPE, forming logic gates.[15]

During the past 15 years or so, many interesting bipolar electrochemical experiments have been presented in the literature. The Crooks group has explored a number of fundamental aspects and applications of bipolar electrochemistry. For example, Chow et al. demonstrated that a microfabricated BPE array consisting of 1000 electrodes could be powered simultaneously.[16] When a sufficiently large driving voltage is applied to the array, electrogenerated chemiluminescence (ECL) is produced at the anodic pole of each BPE. The important result of this experiment is that the wireless capabilities of BPEs allow arbitrarily large arrays of electrodes to be powered in a very simple setup.

A number of groups have shown that bipolar electrochemical reactions can be used to induce motion in objects.[17-20] An illustrative example from Kuhn's group shows that sufficient propulsion to induce the movement of small BPEs can be achieved using bubbles produced by electrochemical reactions (i.e., H_2 or O_2).[21-23] Compositional or chemical gradients can be synthesized on BPEs, as has been elegantly demonstrated by Inagi, Fuchigami, and co-workers, who carried out position-dependent doping of electroactive polymers.[24,25] The Crooks group has also investigated BPEs as a means of enriching and separating charged species electrokinetically. For example, a single Au BPE is used to locally enrich several different charged markers in a single microchannel.[26] This general approach makes it possible to concentrate analytes up to 500,000 fold in a highly controlled zone.[27-33] Additionally, this method can also be applied to achieve desalination.[34] Finally, arrays of BPEs can be used for a variety of sensing and screening applications,[16,35-45] which will be discussed in later chapters.

1.2 Fundamentals of Bipolar Electrochemistry

A key point for understanding wireless bipolar electrochemistry is that the poles of a BPE are oriented in the opposite polarity of the driving electrodes (Scheme

1.2a). This was clearly demonstrated by Manz and co-workers who placed a Pt wire in a weighing boat filled with a pH indicator solution.[46] The application of 30 V between the driving electrodes causes the pH of the solution at the positive driving electrode to decrease due to water oxidation and concomitant production of H^+. Likewise, water reduction at the negative driving electrode leads to formation of OH^- and an increase in pH. A U-shaped Pt wire (BPE) was inserted between the driving electrodes, and the change in color of the indicator demonstrates that water electrolysis occurs at its ends, even though it is not in direct electrical contact with the power supply. Moreover, the relative positions of the colors reveal the poles of the BPE are oriented in the opposite polarity of the driving electrodes.

Cells for carrying out bipolar electrochemistry can be configured to accommodate a range of applications from preparative-scale electrosynthesis to microanalysis. For example, Scheme 1.2a is an illustration showing a simple microscale cell design. In this case, a BPE, or an array of BPEs, is embedded within a microchannel or microfluidic space. Potential contaminants generated at the driving electrodes do not interfere with the BPE in this design, because of the macroscale length of the channel.

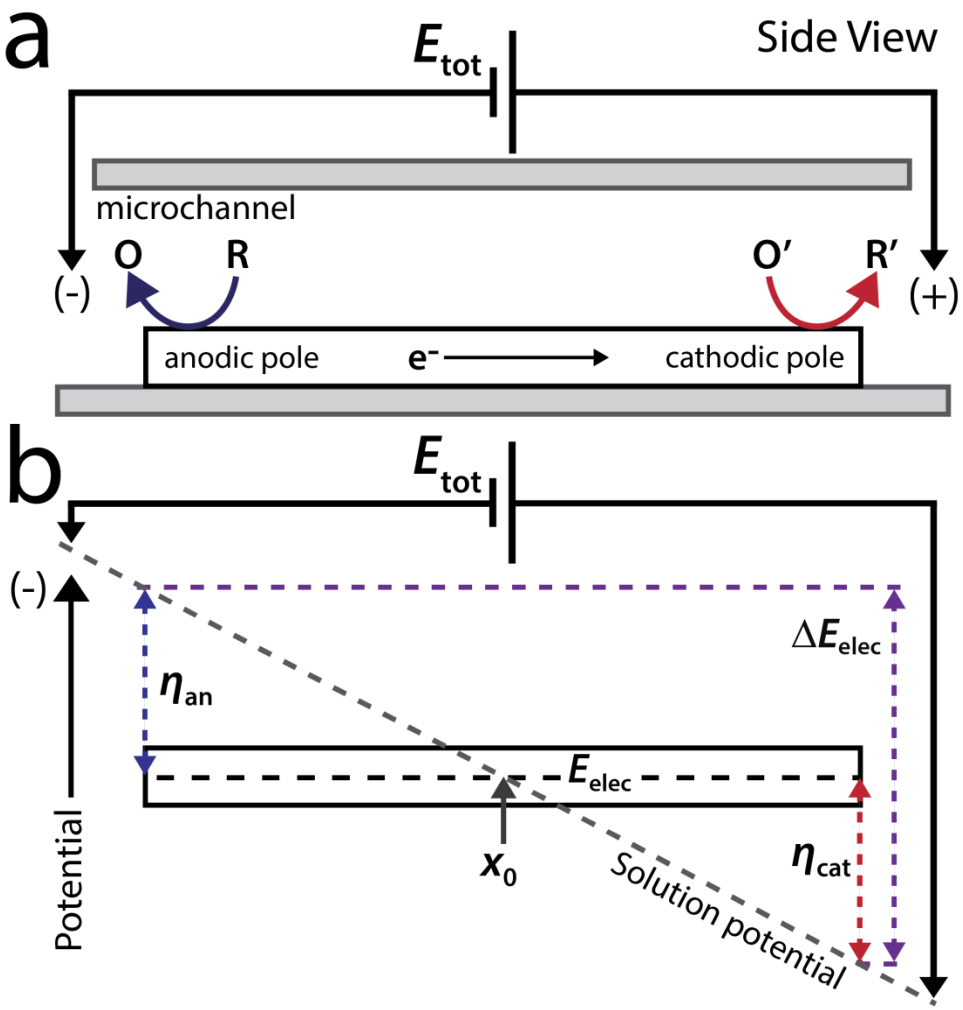

Scheme 1.2. (a) Side view of a BPE within a microchannel. (b) Representation of the distributions of potential in the cell shown in (a).

Potential Differences in Bipolar Electrochemistry. The voltage applied between the two driving electrodes (E_{tot}) results in an electric field in solution that causes the BPE to float to an equilibrium potential (E_{elec}) that depends on its position in the field and the composition of the electrolyte solution. Because the electrode is a conductor, its potential (E_{elec}) is the same (or nearly so) everywhere on its surface. However, the interfacial potential difference between the BPE and the solution varies along its length due to the presence of an electric field in solution. It is these anodic and cathodic overpotentials,[37] η_{an} and η_{cat}, respectively, that drive electrochemical reactions at the poles of a BPE. Scheme 1.2b shows that the magnitudes of the overpotentials depend on just two experimental variables: the magnitude of E_{tot} and the length of the BPE. The location on the BPE that defines the boundary between its two poles, and therefore itself has zero overpotential with respect to the solution, is defined as x_0. Although x_0 is represented as being at the center of the BPE in Scheme 1.2b, its actual location depends on the nature of the faradaic processes occurring at the poles.[37]

As mentioned earlier, the magnitudes of the overpotentials vary along the length of the BPEs, with the highest overpotentials occurring at its extremities. This is in contrast to the working electrode in a traditional three-

electrode cell configuration, wherein the interfacial potential difference is generally considered to be uniform (although this depends on how the cell is designed, the placement of the three electrodes relative to one another, and the resistivity of the electrolyte solution).[47] In either case, however, it is this interfacial potential difference that drives electrochemical reactions.[48] Importantly, the non-uniformity of the interfacial potential differences along the length of a BPE can be quite beneficial.

Controlling the Electric Field and Current Paths. The electric field that powers bipolar electrochemistry is typically applied by a pair (or more) of driving electrodes, which can be metallic (e.g., Au, Ag, Pt, or stainless steel), carbonaceous (e.g., glassy carbon or graphite), or nonpolarizable (e.g., Ag/AgCl reference electrode). The nature of the electric field formed between the driving electrodes depends on the cell geometry and the conductivity of the electrolyte solution. In some cases a linear electric field is generated by restricting the cross-sectional area of the solution between the driving electrodes, thereby increasing its resistance. This can be achieved by embedding the BPE in a microchannel having a small cross-sectional area (e.g., Scheme 1.2a) or by limiting the volume of

electrolyte solution over a BPE in an open channel. We,[37,49] along with Duval and co-workers, have discussed many of the parameters that control bipolar electrochemical processes.[48,50-54] As alluded to earlier, these parameters include E_{tot}, the distance separating the driving electrodes, $l_{channel}$, and the length of the BPE, l_{elec}. The fraction of E_{tot} that is dropped over a BPE, which we refer to as ΔE_{elec}, can be estimated using eq 1.1.[35,48,49]

$$\Delta E_{elec} = E_{tot}\left(\frac{l_{elec}}{l_{channel}}\right) \qquad (1.1)$$

The value of ΔE_{elec} is a critical parameter for analyzing electrochemical processes at BPEs. The simple relationship expressed in eq 1.1 incorporates a number of assumptions that may be possible to ignore for a particular system, but not others. For example, it assumes that an active BPE does not significantly affect the electric field in the solution, which is often not the case.

The foregoing point can be understood in terms of the equivalent circuits shown in Scheme 1.3, which are reasonably good approximations of the resistances present in the type of cell shown in Scheme 1.2a. In the absence of a BPE, the current flowing between the driving electrodes is entirely ionic (Scheme 1.3a).[55] The magnitude of the ionic current moving through the electrolyte is then governed by

the magnitude of the applied potential (E_{tot}) and the resistance of the solution (R_S). When faradaic reactions occur at a BPE, a second path for current, in the form of electrons moving through the BPE, is available (Scheme 1.3b).

We now define the parameter R_{elec}, which is the total resistance to electronic current posed by the BPE, hence, incorporating the charge transfer resistance (R_{ct})[55] and relevant aspects of mass transfer. If the resistance of the solution above the BPE (R_{S2}) is much lower than R_{elec}, then most of the current in the cell passes through the solution rather than the BPE. In this case, the electric field is not significantly perturbed by the BPE. However, when $R_{S2} > R_{elec}$, which can be achieved by lowering the concentration of the electrolyte, substantial current flows through the BPE. This alters the local electric field in solution, which is proportional to $i_{tot}R_{S2}$ (i_{tot} is the total current flowing in the cell), thus resulting in a nonlinear electric field in the solution above the BPE. Duval and co-workers call this effect faradaic depolarization, and its magnitude depends on the strength of the electric field, the concentration of the supporting electrolyte, and the electrochemical properties of the electroactive species in the system.[50-54] It is also important to note that eq 1.1 does not account for any potential dropping at the driving electrodes. The fractional

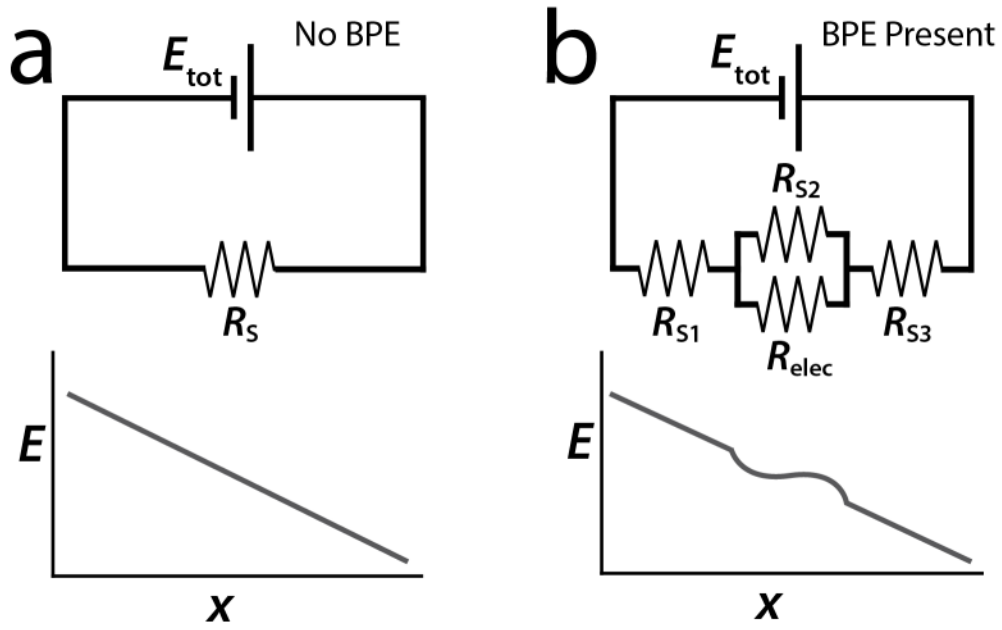

Scheme 1.3. (a) Simple equivalent electrical circuit diagram for a voltage being applied across an electrochemical cell and the resulting potential (*E*) across the length of the cell. (b) Simple equivalent electrical circuit diagram for the same cell shown in (a), but with the incorporation of a BPE and the effect of the BPE on the potential across the length of the cell.

loss of E_{tot} within the electrochemical double layers can, under some circumstances, be substantial.[37] Other electrochemical process can also mitigate eq 1.1, but these are far more minor than the two discussed here and are, therefore, beyond the scope of this dissertation.

Open and Closed BPEs. The majority of this dissertation focuses on the use of "open" BPEs, where current can flow through both the electrolyte and the BPE. As discussed earlier in the text, these types of devices are defined by the existence of two possible current paths: electronic and ionic. However, several interesting reports describe the use of "closed" BPEs (Scheme 1.4a).[56-58] In a closed BPE system the solutions contacting the BPE anode and cathode are physically separated from one another, and the only current path between the two half cells is through a BPE (Scheme 1.4b). One very interesting example of closed BPEs was recently demonstrated by Zhang and co-workers.[59,60] They showed that certain types of carbon microfiber electrodes, which are commonly used in several subfields of bioelectrochemistry, actually function as closed BPEs. This was an important discovery, because it accounts for numerous measurement artifacts that have been observed over the last ~30 years.

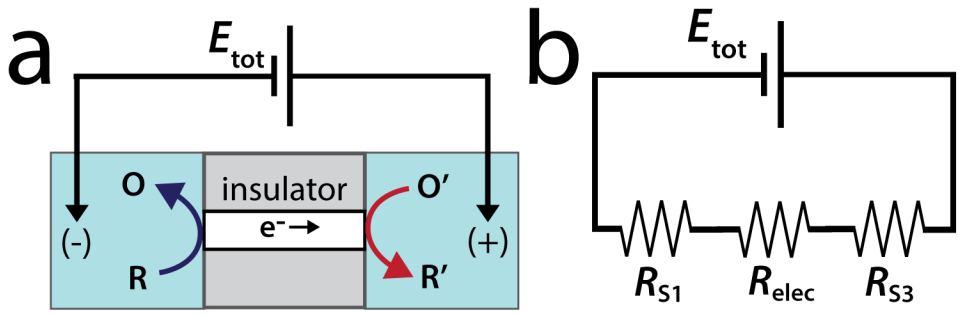

Scheme 1.4. (a) Schematic illustration of a "closed" bipolar electrochemical cell where the BPE is the only current path between the two half cells. (b) Simple equivalent electrical circuit for the closed BPE cell.

1.3 BPEs for Sensing and Screening

Principles of BPE-Based Sensing and Screening. BPEs have only recently been used as electroanalytical sensors, probably because it is not easy to directly measure the current flowing through them. However, the Crooks group recently solved this problem. Consequently, the advantages of using BPEs for sensing and screening applications have become more compelling. Within the context of sensing and screening, these advantages include: (1) no direct electrical connection is required; (2) many electrodes can be controlled simultaneously with a single DC power supply; (3) the sensing electrodes can have micron-scale, or even nanoscale, dimensions.

The basic operating principle of BPE sensing and screening devices relies on electrical coupling between the sensing and the reporting poles (the reporting pole is the end of the BPE signaling the state of the sensing pole). In other words, the current passing through the two poles of the BPE must be equal (i.e., $i_{cat} = -i_{an}$). For example, and as shown in Scheme 1.5a, if the sensing reaction is an electrochemical reduction, then the electrons required at the cathodic pole originate from a proportional oxidative reporting reaction at the anodic pole. In the absence of the analytical target species, no oxidation occurs. Most

reporting reactions that have been discussed in the literature are oxidations that generate an easily observable optical signal at the anodic pole of a BPE. Optical readouts include ECL, fluorescence, and anodic dissolution (or change in refractive index) of a metal film. The advantage of these approaches is that they are easily implemented in parallel and are thus amenable to simultaneous readout of large arrays of BPEs. When employing these arrays, it is important to consider that sensing and screening experiments typically require each electrode to act independently of others, and therefore the amount of diffusion layer overlap between electrodes and the extent of faradaic depolarization should be minimized.

Amperometric Detection using Split Microband BPEs. It is also possible to directly measure the current passing through a BPE by inserting an ammeter between its poles (Scheme 1.5b). This method is useful for calibrating optical signals for a small number of BPEs, but it is impractical for large arrays because an ammeter would be required for each electrode. An early demonstration of directly measuring the current flowing through a BPE was introduced by Nyholm and Klett, who used BPEs for amperometric detection in CE.[61] For this purpose, they used the split BPE configuration shown in Scheme 1.5b, which consists of two separated poles

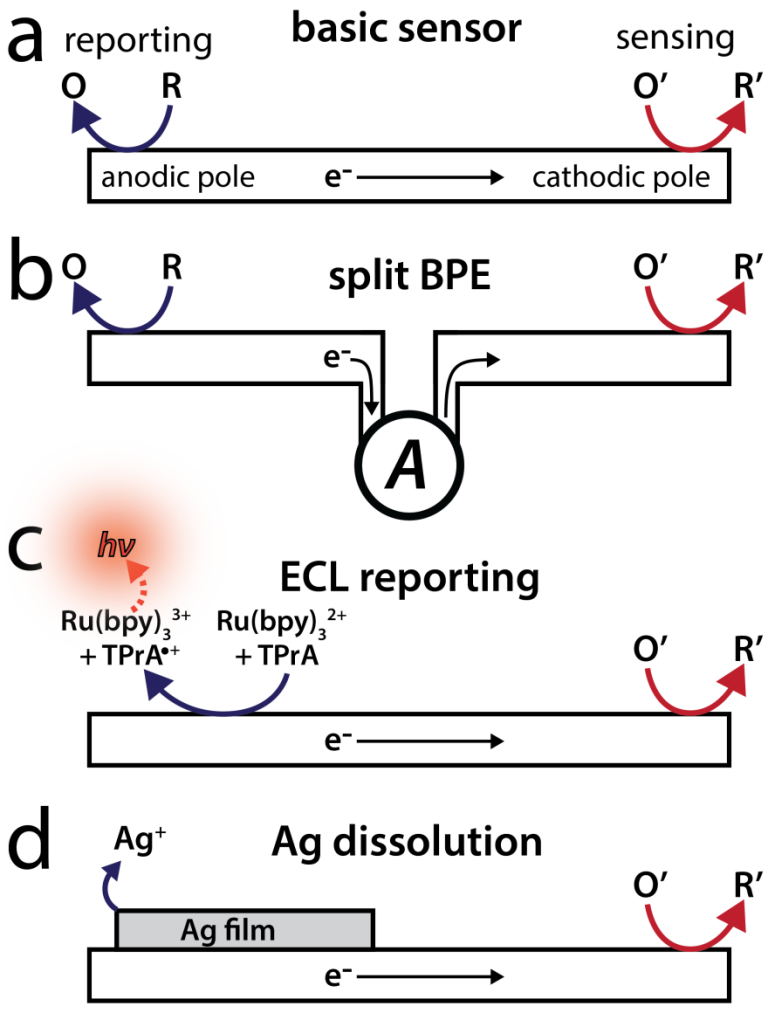

Scheme 1.5. Schematic illustrations of the basic sensing and screening methods typically used in bipolar electrochemical systems.

connected external to the capillary with an ammeter. By taking advantage of the electric field inherent to CE, this approach avoids the need for a potentiostat. Note, this high field is a nuisance when one tries to integrate traditional three-electrode electrochemical detection into CE.[62] The authors demonstrated that a split BPE produces results similar to those obtained using cyclic voltammetry. Nyholm and co-workers later expanded this work to include an array of 20 Au microbands so that analytes with different E^{o} values could be detected simultaneously.[63]

Sensing and Reporting by ECL at a Single BPE Pole. To avoid making a direct electrical contact to the BPE, Manz and co-workers introduced ECL as an optical signal transduction method (Scheme 1.5c).[46] Briefly, ECL occurs when an excited state molecule, generated from a series of charge-transfer reactions, relaxes to the ground state and emits a photon.[64] ECL is highly sensitive, with near zero-background signal, because no excitation light source is required to drive it. One of the most effective and widely used ECL reactions involves the co-oxidation of tris(bipyridine)ruthenium(II) ($Ru(bpy)_3^{2+}$) and tri-*n*-propylamine (TPrA). Manz and his colleagues used this type of ECL reaction to detect $Ru(phen)_3^{2+}$ and $Ru(bpy)_3^{2+}$ following electrophoretic separation. In this case, TPrA was present in the separation

column, and the electric field required for CE separations energized the BPE. When both detection and readout occur at the same pole of the BPE, as in this example, then the accessible analytes are limited to species that participate or compete with the ECL-producing reaction. A competition reaction was recently demonstrated in which mRNA sequences associated with breast cancer cells displaced a second strand labeled with a $Ru(bpy)_3^{2+}$-laden silica particle resulting in a reduction in ECL intensity.[65]

Electrically Coupled Sensing using ECL. The Crooks group introduced a sensing scheme in which the reporting and sensing reactions occur on different poles. The important innovation here is that the sensing and reporting poles are decoupled, but their electrochemical relationship is preserved *via* conservation of charge (Scheme 1.5c). This new approach eliminated the previous requirement that analytes be capable of direct participation in the ECL reaction sequence, and hence opened the door to BPE sensing of a wide variety of analytes.

In the initial study, Zhan et al. showed that the detection of benzyl viologen (BV^{2+}) at the BPE cathode was electrically coupled to ECL emission occurring at the anode (Scheme 1.5c). Moreover, the effect of electrode length and geometry on ECL emission were investigated.[35] With Duval's

work as a foundation, Mavré et al. described a semi-empirical approach for predicting E_{elec}, in addition to ΔE_{elec} as a function of E_{tot}, and showed that the intensity of ECL emission can be directly correlated to the magnitude of current flowing through the BPE.[37] During a sensing or screening experiment using BPEs as illustrated in Scheme 1.2, which are referred to as "open" BPEs, it is critical that each electrode experiences a uniform electric field. As alluded to earlier, this means that only a small fraction of the total current, typically less than 1%, is permitted to pass through the BPE with the remainder traversing the solution as an ionic flux (Scheme 1.3b).[37] Closed BPEs do not have this requirement because the only path for current flow between driving electrodes is *via* electron transfer through the BPEs (Scheme 1.4).

On the basis of these simple operating principles, BPE sensors have been employed to detect myriad analytes. For example, Chow et al. demonstrated a DNA sensor with ECL readout following a design similar to that shown in Scheme 1.5c, except the cathodic pole of a Au BPE was modified with a thiol-terminated probe single-stranded DNA (ssDNA) sequence.[36] In a control experiment, with E_{tot} = 22 V, no ECL was observed because ΔE_{elec} was insufficient to drive significant faradaic reactions at the modified Au BPE. However, when the target ssDNA labeled with a Pt

nanoparticle (NP) hybridized with the electrode, E_{tot} = 22 V was sufficient to drive the ORR at the Pt NP surface. The lowering of the required η_{cat}, and thus ΔE_{elec}, by the Pt catalyst then activated ECL emission at the anode. This experiment also clearly demonstrated a basic principle of many BPE sensing platforms: the sensing reaction must facilitate or catalyze a reaction to enhance the current flowing through the BPE.

As previously mentioned, one of the main virtues of bipolar electrochemistry is that many BPEs can be driven simultaneously using a single power supply and two driving electrodes. Chow et al. demonstrated that 1000 individual BPEs can be powered using a simple power supply and a pair of driving electrodes.[16] When a sufficiently high E_{tot} is applied through the two driving electrodes spanning the array, ECL emission was observed at the anode of each of the electrodes. The most important design rule for large arrays of this sort is that the potential dropped over each electrode (ΔE_{elec}) be the same.

In some cases, the solution conditions required for sensing and reporting reactions may be incompatible with one-another, and hence it is necessary to place the anodic and cathodic poles of the electrodes into spatially isolated compartments. To address this requirement, Chang et al. developed a bipolar electrochemical cell in which a BPE, or

multiple BPEs, span two microchannels.[44] When the same E_{tot} is applied across the two channels, the sensing and reporting reactions are electrically coupled through the BPE but remain otherwise separated. This approach has been used to follow ECL emission coupled to the reduction of $Fe(CN)_6^{3-}$, which can be used for the indirect detection of glycated hemoglobin.[44] Chen and co-workers recently used a similar two-channel design to detect prostate-specific antigen (PSA). In their approach, PSA guides the deposition of Ag NPs to the space between two microbands. Eventually the two microbands become electrically connected, and the resulting BPE has sufficient length to generated ECL at the applied value of E_{tot}.[66]

Interestingly, new functionality has been introduced to ECL reporting by changing the shape of the BPE. A single triangle acts just like an array of individual BPEs having different lengths, which means that each location on the edge of a triangular BPE experiences a different overpotential. Hence, a single luminescence micrograph can be used to extract kinetic information using a technique called "snapshot voltammetry".[40] Multiple channels and BPEs can be configured to yield logic functions like NOR, OR, and NAND with optical readout.[38,67] These could eventually be useful for sensing and signaling applications. Foret, Manz, and co-workers recently demonstrated that floating Au

platelets can act as BPEs in a CE separation, where ECL might be used to follow a cathodic sensing reaction.[68] The important result is that the platelets are easily replaced because they move in the separation volume.

Detection Using Anodic Dissolution of a Metal Film. In addition to ECL readout, the Crooks group has pioneered the use of metal film electrodissolution as a reporting reaction for bipolar electrochemistry.[39] When E_{tot} is applied, the electrodissolution of thermally deposited Ag is electrically coupled to a reduction reaction occurring at the cathodic pole of the BPE (Scheme 1.5d). Because η_{an} is highest at the extreme edge of the BPE anode, Ag first begins to dissolve at the distal edge of the electrode and then continues to dissolve towards x_0. The dissolution will continue until it reaches a critical point, where ΔE_{elec} cannot drive the two types of faradaic processes. This approach has a number of advantages over the ECL signaling method. First, it eliminates the need for detection of light, because the change in length of the electrode can be read with the naked eye. Second, it eliminates the need for solution-phase reagents like $Ru(bpy)_3^{2+}$. Third, the amount of charge stored in the Ag as a function of its length depends only on the thickness of the film, and therefore a very broad dynamic range of sensitivities is available for sensing

applications. Fourth, Ag dissolution is associated with a single redox process, whereas ECL relies on two redox processes which can compromise the limit of detection for sensing applications.[37]

Chow et al. demonstrated the idea of using the Ag electrodissolution reaction for chemical sensing by immobilizing a probe ssDNA sequence on the cathodic pole of a BPE.[39] When a target sequence labeled with horseradish peroxidase (HRP) hybridized to the probe, the HRP catalyzed the reduction of H_2O_2 to water *via* a mediator. The presence of the mediator, and hence the ssDNA target, was then signaled by a change in the length of the Ag thin film at the anodic pole of the BPE. In the absence of the target no change was observed.

Interestingly, a BPE can be activated without any external power source by using a phenomenon called streaming potential, which is essentially the opposite of electroosmosis because it is initiated by simply pushing an electrolyte solution through a microchannel having charged walls.[42] Streaming potentials resulted from the movement of counterions in the electrical double layer at the interface between the electrolyte solution and the charged walls of a poly(dimethylsiloxane) (PDMS)/glass microchannel. When the resistivity of the electrolyte solution is kept high (~MΩ·cm), streaming potentials of up to 8 V can be achieved.

As a proof of concept, benzoquinone was detected using Ag electrodissolution as a reporting mechanism. By eliminating the need for a power source, this type of detection scheme opens up the possibility to perform point-of-care sensing applications in resource-limited settings.

1.4 Combinatorial Electrocatalyst Screening

Methods for screening large arrays of electrocatalysts have emerged over the past ~15 years.[69] One approach for discovering effective electrocatalysts is to rapidly evaluate large libraries of potential candidates.[70,71] Promising materials identified during this preliminary screening step can then be subjected to more extensive and quantitative testing.[72,73] Several techniques have been reported for rapid electrocatalyst screening. One of the first high-throughput methods was reported by Smotkin, Mallouk, and co-workers to screen for methanol-oxidation electrocatalysts. They used ink-jet printing to define candidate materials on carbon paper and a pH-sensitive fluorescent indicator to reveal the most effective catalysts.[74] Other approaches make use of individually addressable working electrodes where the current passing through each electrode is monitored more or less simultaneously.[75-78] The advantage of this method is that electrochemical parameters, such as kinetics, can be

measured directly, but the cost for this additional information is increased complexity and smaller libraries.[75,77] An approach pioneered by Bard and co-workers uses scanning electrochemical microscopy (SECM) to identify potential catalysts.[69,72] Similar scanned-probe techniques have been reported for identifying photoelectrocatalysts by using either a rastered laser beam or optical fiber.[79,80] These scanned probe techniques can be information rich, but they are usually rather slow as each array element is evaluated in serial rather than parallel. Finally, Tao and co-workers recently reported an approach that takes advantage of changes in the local refractive index of the electrolyte solution that arise from products of electrocatalytic reactions (for example, HER) which can be measured using SPR microscopy.[81] Additional discussion of related screening techniques can be found in later chapters.

1.5 Single Particle Collisions and Paper-Based Devices

Chapters 7 and 8 describe advances in electroanalysis that are not immediately related to the bipolar electrochemical techniques described in the previous sections. Details regarding my contributions to these areas of research are described in the respective chapters.

1.6 Research Summary and Accomplishments

My dissertation focuses on the development of BPEs as a screening platform for electrocatalyst candidates, the development of an array of BPEs from a single conductive substrate, the optical tracking of single insulating particles with an active ultramicroelectrode, and the incorporation of microwires, meshes, and fibers into paper-based electroanalytical devices.

Chapter 3 describes the initial proof of concept study for the electrocatalyst screening using BPEs where the performance of monometallic NPs made of Au and Pt were compared to the naked supporting electrode material, indium tin oxide (ITO).[43] The readout for this array was the removal of Ag microbands from the anodic poles of the BPEs. The number of microbands that were removed correlated strongly with the performance of the materials measured in a traditional 3-electrode electrochemical experiment.

Chapter 4 describes the expansion of the platform for testing bimetallic materials for the ORR.[45] First, the size of the array was expanded by over an order of magnitude. Second, bimetallic electrocatalyst candidates were prepared using piezodispensing. Third, the anodic reporter was changed from Ag to Cr, which requires a more positive oxidation potential to undergo electrodissolution. These

modifications allowed a series of Pd containing species to be evaluated: Pd-Au, Pd-Co, and Pd-W.

Chapter 5 demonstrates that the platform is applicable to other reactions of interest, such as the HER.[82] Several experimental parameters were adapted for the new reaction of interest. First, a small purge box was added to remove ORR background. Second, the density of the array was increased so that trimetallic compositions could be evaluated. Third, the experiment was ended while the materials were still active. 231 different materials were tested based on bi- and trimetallic combinations of Co, Fe, Ni, Mo, and W.

Chapter 6 describes the control of electric fields in microfluidic spaces to localize faradaic reactions on different regions of a single electrode.[41] This was accomplished by placing the BPE at the intersection of two orthogonal microchannels and applying two different values of E_{tot}. The vector sum of these two applied potential differences could be mapped out using an array of BPEs and finite element simulations.

Chapter 7 describes the optical tracking of discrete insulating particles as they interact with an operating UME.[83] The interesting new result is that the behavior of these particles that are electrostatically attracted to the operating electrode can be directly visualized and several interesting features that appear in chronoamperometric

traces (*i*-*t* curves) can be correlated directly to optical results.

Chapter 8 describes the incorporation of wires, fibers, and meshes as working electrodes in paper-based analytical devices.[84] The important new result is that the wire-based approach has many advantages over traditional electrode architectures and provides means of selecting the electrode material to fit the electroanalytical need.

Chapter 2: Experimental

2.1 Chemicals

All chemicals used in this work are described in the individual chapters.

2.2 Techniques

Photolithography and Etching Techniques. The devices used in this work were microfabricated using photolithography and a variety of etching techniques. Photolithography is a process that uses light to create a pattern of a material on a supporting substrate. Contact-mode photolithography was used here, meaning that a photomask makes direct contact with the photoresist to be patterned.

Scheme 2.1 shows the general photolithographic steps for the preparation of BPEs for metal film electrodissolution. For the production of Au, ITO, and FTO patterned supports, a thin layer of photoresist (PR1) is spin-coated onto a slide having the desired material already deposited. The PR1-coated slide is then covered by the photomask and exposed to UV light. The exposed PR1 is removed during a development step. The pattern is then transferred to the material during an etching process, which depends on the material used. Once the pattern has been transferred and residual PR1 has been removed,

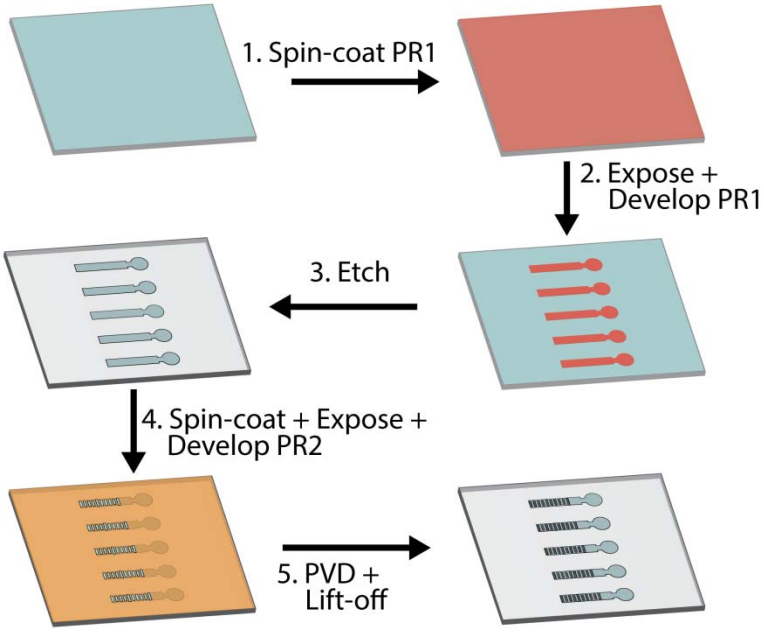

Scheme 2.1. Schematic illustration of the general micro-fabrication procedure to prepare BPE devices.

a second photoresist (PR2) is spin-coated onto the previously patterned device and exposed to UV light when in contact with a second photomask. PR2 is patterned in such a way as to only expose a small portion of each BPE in the array, such that an array of microbands can be prepared. The devices with the patterned photoresist are then placed into a vacuum chamber used to evaporate the metal film of interest, Ag or Cr, by physical vapor deposition (PVD). Once the metal is deposited, PR2 and the metal film atop it are lifted off the surface of the device by sonication in an appropriate solvent, such as acetone. More specific procedures can be found in the individual chapters.

Microchannels used in the work were constructed in several ways. For screening experiments, a silicone gasket spacer was sandwiched between glass slides to prepare a microfluidic space and will be described in later chapters. PDMS microchannels were used in the 2D-BPE work and were prepared using soft lithography,[85] where a patterned photoresist film acts as a mold for the PDMS. The PDMS is poured over the mold and heat cured resulting in an elastomeric product. Reservoirs used to inject solution and house driving electrodes are punched into the end of the channels through the entire PDMS layer. The PDMS is then attached to the slide containing the BPEs by an air plasma pretreatment followed by heating at 80 °C for 1 min.

Materials Characterization. Several materials and objects studied in this dissertation were examined using scanning electron microscopy (SEM). SEM uses a beam of electrons to image materials and surfaces. The incident electrons can eject secondary, inner-shell electrons from the surface atoms of the material, which can then be collected by a suitable detector to generate an image of the materials surface. Additionally, if the energy of the incident electrons is sufficiently high, X-rays may be generated from the sample material and analyzed in a process known as energy dispersive X-ray spectroscopy (EDS). The X-rays produced are characteristic of the elements present in the sample based on the energy released during the transition of an electron from an outer, high energy shell to a hole in a lower energy shell that was produced by the incident electron beam. The X-rays can be collected by a detector to produce an entire spectrum simultaneously and specific energies can be assigned to various elements and/or their respective transitions. The relative amounts of the elements present in each sample can be determined from EDS spectra by the integration of the respective peak areas of the transitions for each element.

Materials were also evaluated using X-ray photoelectron spectroscopy (XPS). XPS uses a beam of monochromatic, incident X-rays to irradiate the surface of a sample, which

produces photoelectrons with energies characteristic of the atoms present at the surface of the material. XPS is a very sensitive surface analytical technique that gives information not only about which elements are present at the surface of the material, but also their oxidation state and chemical environment. Typically, the incident X-rays effect the ejection of photoelectrons from several electron shells, depending on the atomic number of the surface atoms. The photoelectrons produced by the surface atoms are detected based on their respective kinetic energies, but because the source produces X-rays of a specific energy (i.e., monochromatic), the kinetic energies can be easily converted to binding energies. By selecting specific binding energy windows, specific elements can be detected with high spectral resolution.

Piezodispensing. Piezodispensing is a technique where very small volumes of solution (pL to nL) are ejected from a small tip onto a substrate of interest using small DC voltage programs applied to a piezoelectric material in the tip. The array dispenser used in these works consisted of a printhead assembly with 4 piezoelectric microdispensing devices that were fed by 2 mL fluid reservoirs. The pressure of the reservoirs was adjusted by a pneumatic controller and a vacuum/pressure pump. To achieve spatially-resolved

dispensing onto BPEs defined photolithograpically, the printhead assembly was mounted onto an *x,y,z* robotic positioner, which was controlled by a PC. The alignment of the devices on the spotter stage was achieved using a USB-microscope mounted under the stage.

Chapter 3: Bipolar Electrodes for Rapid Screening of Electrocatalysts

3.1 Synopsis

In this chapter we report a method for rapidly screening arrays of electrocatalyst candidates. The approach is based on simultaneous activation of the ORR and Ag electrodissolution at the cathodic and anodic poles, respectively, BPEs. Because the electrochemical activity of the two poles is directly coupled *via* the BPEs, the extent of Ag electrodissolution is directly related to the ORR activity. The screening process lasts ~12 min. Because Ag dissolution provides a permanent record of catalyst activity, the screening results can be determined by simple optical microscopy after the electrochemical experiment. The method has the potential to provide quantitative information about electrocatalyst activity.

3.2 Introduction

In this chapter we report a new and potentially powerful method for rapid screening of electrocatalysts. The principle is illustrated in Scheme 3.1, with specific reference to evaluation of the activity of electrocatalysts for the ORR. The top frame of Scheme 3.1a shows an array of three BPEs.[49] The ORR electrocatalyst candidates are

deposited onto the cathodic poles of the BPEs, while the anodic poles are comprised of parallel Ag microbands. The Ag microbands of each electrode are in electrical contact with one-another and with the ORR catalysts *via* an underlying ITO contact. When a sufficiently high potential (E_{tot}, Scheme 3.1b) is applied to the solution in the fluidic channel *via* a pair of driving electrodes, the ORR proceeds at the cathodic poles, and the Ag microbands undergo electrodissolution.[39] The efficiency of the ORR catalyst is then determined by counting the number of dissolved Ag microband electrodes: the more bands that dissolve, the better the catalyst. In fact, as we will show, there is a direct thermodynamic link between the overpotential required for the ORR (Scheme 3.1c) and number of Ag microbands remaining after the experiment (Scheme 3.1a). Although we demonstrate this screening method using just three BPEs, arrays of arbitrary size can be monitored in this way with very little additional technological overhead. This is because it is not necessary to make a direct electrical connection to each electrode, which is an intrinsic property of BPEs and the principal reason for using them in an array format.[16]

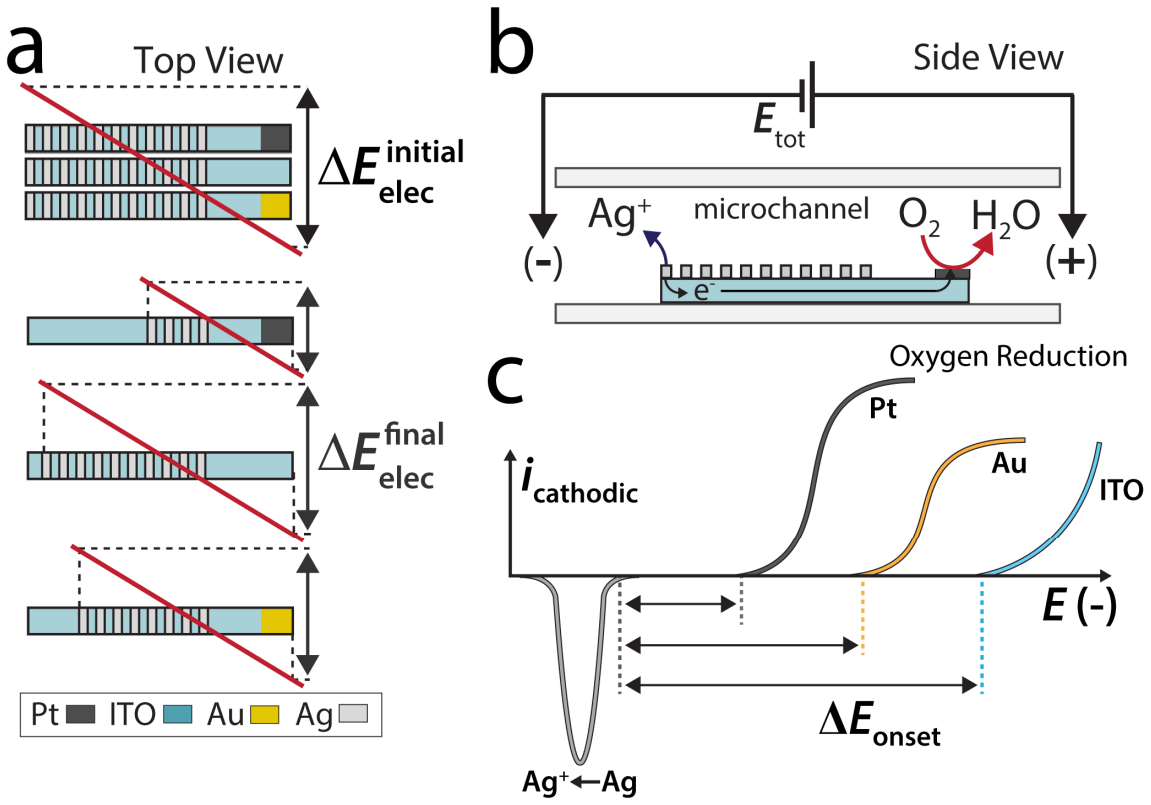

Scheme 3.1. Schematic illustration of the general screening experiment using BPEs. (a) Depiction of a BPE array where each electrode consists of an underlying ITO support and is modified with an array of Ag microbands at the anodic pole. The cathodes of three electrodes are modified with either Pt NPs, left as naked ITO, or modified with Au NPs. The BPEs are subjected to the same electric field and the relative performance of each catalyst candidate is determined based on the number of Ag microbands removed. (b) Side view of the microchannel used to house the BPE array depicted in (a). (c) Schematic illustration of the potential differences needed to drive the anodic reporting reaction (Ag oxidation) and the ORR at the NPs or the background process on naked ITO.

A driving voltage (E_{tot}) applied across a microchannel containing a conductive electrolyte solution (Scheme 3.1b) is dropped nearly linearly over the length of the microchannel.[37] If a conductive wire of sufficient length is present in the microchannel, it will function as a BPE.[49] Specifically, when the interfacial potential differences between the poles of the BPE and the electrolyte solution (ΔE_{elec}, Scheme 3.1a) are sufficiently high, faradaic processes occur simultaneously: a reduction at the cathodic pole and an oxidation at the anodic pole. Because the reactions are electrically coupled, the current passing at each pole must be the same. As mentioned earlier, a key advantage of bipolar electrochemistry is that electrochemical reactions proceed without the need for a direct electrical connection to each electrode. This means that large arrays of electrodes can be controlled simultaneously using a single voltage source.[16] Finally, the current flowing through a BPE can be monitored visually by ECL,[35] or, as implemented here, by following the electrodissolution of a Ag film.[39] Compared to some of the limitations discussed in Chapter 1.4, this approach combines the best attributes of these previously described methods: it is simple, catalyst hits are detected in parallel so it is fast, and it has the potential to provide as much kinetic and thermodynamic information as the earlier methods.

3.3 Experimental Section

Chemicals and Materials. Commercially available ITO-coated glass slides (~6 Ω/sq, Delta Technologies, LTD, Loveland, CO) were used to fabricate the BPEs. A silicone gasket (0.5 mm-thick, JTR-S-0.5, Grace bio-labs, Bend, OR) was used to create the microfluidic channel. A PDMS block served as the top of the microchannel. $HAuCl_4$, K_2PtCl_4, $NaBH_4$, sodium acetate, NaOH, and Ag wire (99.99 %) were obtained from Sigma-Aldrich. Glacial acetic acid was from Fisher Scientific. All above chemicals were used as received. Sixth-generation, hydroxyl-terminated dendrimers (G6-OH) were obtained from Dendritech Inc. (Midland, MI) as 10.0% (w/w) solutions in methanol. Prior to use, the methanol was removed under vacuum and the dendrimers were re-dissolved in Milli-Q water (18.2 MΩ-cm) water to yield a 100 µM solution.

Preparation of DENs G6-OH(Pt_{225}) dendrimer-encapsulated nanoparticles (DENs) were prepared by a previously described procedure.[86] 2.25 mM K_2PtCl_4 was added to a 10.0 µM solution of G6-OH in Milli-Q water. Pt^{2+} was allowed to complex with tertiary amines present within the dendrimer for 72 h before addition of a 10-fold excess of the reducing agent ($NaBH_4$ in Milli-Q water). After addition of the reducing agent, the solution vial was left tightly-capped for 24 h. G6-OH(Pt_{225})

DENs were dialyzed against Milli-Q water for 24 h. Figure 3.1a is a UV-vis spectra of the reduced G6-OH(Pt_{225}) DENs.

G6-OH(Au_{225}) DENs were also prepared by a previously described procedure.[87] Briefly, 450 µM $HAuCl_4$ was added to a 2.0 µM solution of G6-OH dendrimer, followed quickly (< 3 s) by a 10-fold excess of $NaBH_4$ in 0.3 M NaOH (the NaOH serves to slow the reduction process). The DEN solution was left open to the atmosphere for 24 h before use. Figure 3.1b shows the UV-vis spectra of the reduced G6-OH(Au_{225}) DENs.

Microfabrication and Preparation of Devices. ITO slides were cleaned by sonicating for 15 min in a ~1% Triton-X 100 solution in Milli-Q water. The slides were then sonicated for 15 min each in Milli-Q water and then ethanol. The slides were dried under a gentle stream of N_2. A thin layer of positive photoresist (~15 µm, AZ P4620, AZ Electronic Materials, Branchburg, NJ) was spin-coated onto each slide. The photoresist was patterned by exposure to UV light through a positive mask. The exposed photoresist was developed and the design was transferred to the ITO layer by plasma-assisted reactive ion etch (PlasmaLab 80+, Oxford Instruments, Bristol, UK). The protective photoresist was removed by sonication in acetone and the slides were cleaned by sonication as before.

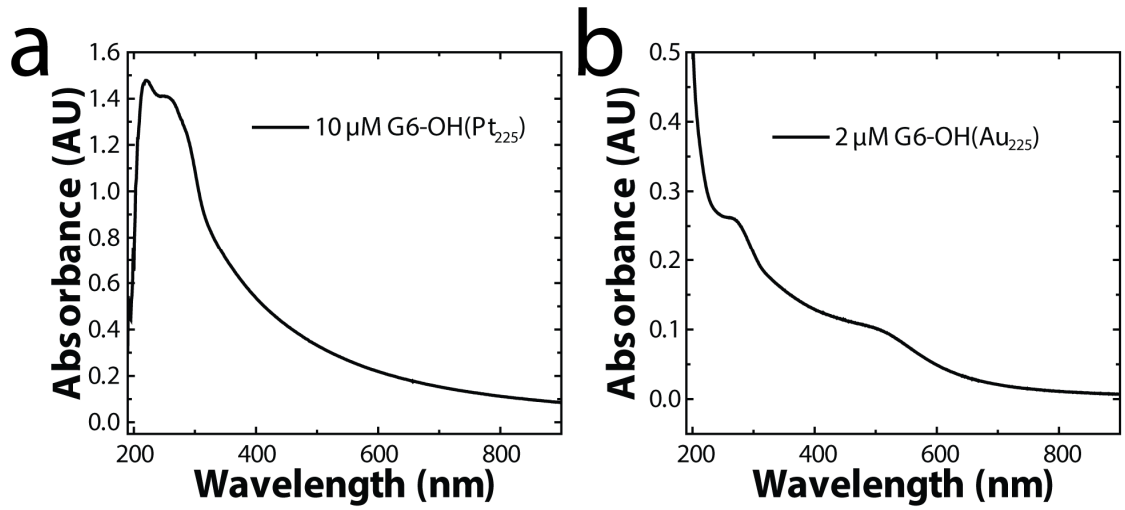

Figure 3.1. UV-vis spectra of the reduced metal DENs. A quartz cuvette having an optical path length of 0.2 cm was used. The spectra were blanked against a G6-OH solution of the appropriate concentration. (a) is the UV-vis spectrum of a dialyzed 10 µM G6-OH(Pt_{225}) solution. It exhibits monotonically increasing absorbance toward lower wavelengths, which is characteristic of small metal nanoparticles.[86] Characteristic ligand-to-metal-charge-transfer (LMCT) bands are present at 220 and 250 nm. This spectrum is consistent with others reported previously by our group.[86] (b) is the UV-vis spectrum of an undialyzed 2 µM G6-OH(Au_{225}) solution. It also shows increasing absorbance at lower wavelengths. This spectrum reveals a band at 290 nm associated with interactions between Au and the dendrimer and a small plasmon band at 510 nm. All of these characteristics are consistent with previous reports.[87]

A thin layer of negative, lift-off photoresist (~0.7 µm, ma-N 1405, MicroChem Corp., Newton, MA) was spin-coated onto the patterned ITO, and the lift-off features were defined by exposure to UV light through a negative mask. The photoresist was then developed and the slides were mounted in a PVD system (Explorer, Denton Vacuum, Moorestown, NJ). A 5 nm-layer of Cr was deposited onto the ITO (to improve adhesion of the Ag) and 20 nm of Ag was deposited onto the lift-off patterned slides. Lift-off was achieved by sonicating the slides in acetone for ~10 min or until all the Ag was removed. The devices were then sonicated sequentially for 15 min each in ~1% Triton-X 100 in water, Milli-Q water, and then ethanol. Finally, the slides were dried under a gentle stream of N_2. Approximately 10 nL of the DENs solution (10 µM for G6-OH(Pt_{225}) and 2 µM for G6-OH(Au_{225})) was delivered to the cathodic poles of the BPEs using a glass micropipette fitted to a plastic syringe.

Device Construction. The microchannel was formed by placing the 0.5 mm-thick silicone gasket (with the channel cut into it) onto the BPE slide. This was covered with a block of PDMS containing the reservoirs, which are used to fill the channel and hold the driving electrodes. The driving electrodes were prepared by the incorporation of agarose gels (~5 mm thick) containing 2 M KCl into glass tubes (~4

mm diameter). The glass tubes were then filled with saturated KCl and a chloridized Ag wire was placed into the filled tube.

A microscope (Nikon AZ 100, Nikon Co., Tokyo, Japan) with a CCD camera (Cascade, Photometrics Ltd., Tucson, AZ) was used to obtain the optical micrographs. Micrographs were processed using V++ Precision Digital Imaging software S3 (Digital Optics, Auckland, New Zealand). Cyclic voltammograms were collected in a 3-electrode cell using a computer-based potentiostat (Model CHI700D potentiostat, CH Instruments, Austin, TX). UV-vis absorbance measurements were acquired with a Hewlett-Packard HP8453 spectrometer.

3.4 Results and Discussion

As shown is Scheme 3.1b, when a sufficient driving potential (E_{tot}) is applied across the microchannel, faradaic reactions are driven simultaneously at the two poles of the BPE. The fraction of E_{tot} dropped over each BPE is approximately the ratio of the length of the BPE (l_{elec}) to the length of the microchannel ($l_{channel}$, eq 1.1).[49]

In the method discussed here, ΔE_{elec} drives both the ORR and the electrodissolution of the Ag microbands (Scheme 3.1b). The highest overpotentials are experienced at the ends of the BPEs, and therefore when the ORR is activated at the cathode the distal Ag microband will dissolve first.[37,39]

As more proximal Ag microbands dissolve, the effective length of the BPE decreases leading to a smaller ΔE_{elec} (bottom frames of Scheme 3.1a). This results in a decrease in the overpotential available to drive the ORR and Ag dissolution.[39,48]

As shown in Scheme 3.1a, if electrocatalysts requiring different overpotentials to drive the ORR (Scheme 3.1c) are present at the cathodic pole of each BPE, then the number of Ag microbands that dissolve will be different. That is, Ag dissolution will cease once the potential dropped over each electrode becomes insufficient to drive the electrically-coupled faradaic processes. This means there is a thermodynamic relationship between the final length of each BPE and the activity of the electrocatalytic material deposited at the cathodic pole.

Screening Electrocatalysts with BPEs. Figure 3.2a is an optical micrograph of an array of three BPEs having the designs and compositions illustrated in the top frame of Scheme 3.1a. Each BPE is a microfabricated ITO strip having a total length of 1.00 mm and a width of 0.25 mm. The 26 Ag microband electrodes deposited over the ITO foundation, which comprise the functional anode of each BPE, have a length of 15 μm and are spaced by 10 μm. To demonstrate proof of concept, three different cathode materials were

tested for their ORR activity. Pt and Au DENs[88] were drop-cast onto the cathodic poles of the top and bottom BPEs, respectively. These materials are denoted as G6-OH(Pt_{225}) and G6-OH(Au_{225}), respectively, to indicate that the individual catalytic nanoparticles consist of ~225 atoms and are encapsulated within sixth-generation poly(amidoamine) (PAMAM) dendrimers that are terminated with hydroxyl functional groups. The cathodic pole of the middle electrode in Figure 3.1 was not modified, and hence consists of ITO only. We have previously shown that Pt and Au DENs are catalytic for the ORR.[86,89] Moreover, it has been shown that PAMAM dendrimers terminated in hydroxyl groups form dense films on ITO surfaces.[90] Note that the onset of cathodic current on these ITO films has been attributed to partial reduction of surface metal oxides followed by either H^+ reduction or further reduction of the metal oxides.[91] The microchannel (Scheme 3.1b) containing the BPEs was filled with air-saturated, 0.10 M acetate buffer (pH 4.0). Acetate buffer was used instead of a strong acid like $HClO_4$ or H_2SO_4, because the former is more compatible with ITO and Ag. Figures 3.2b through 3.2e show the same device at times ranging from t = 60 s to t = 730 s after application of E_{tot}. Note that E_{tot} was set to 10.0 V for the first 60 s of the experiment (Frame 3.2b) and 4.0 V thereafter (Frames 3.2c-3.2f).

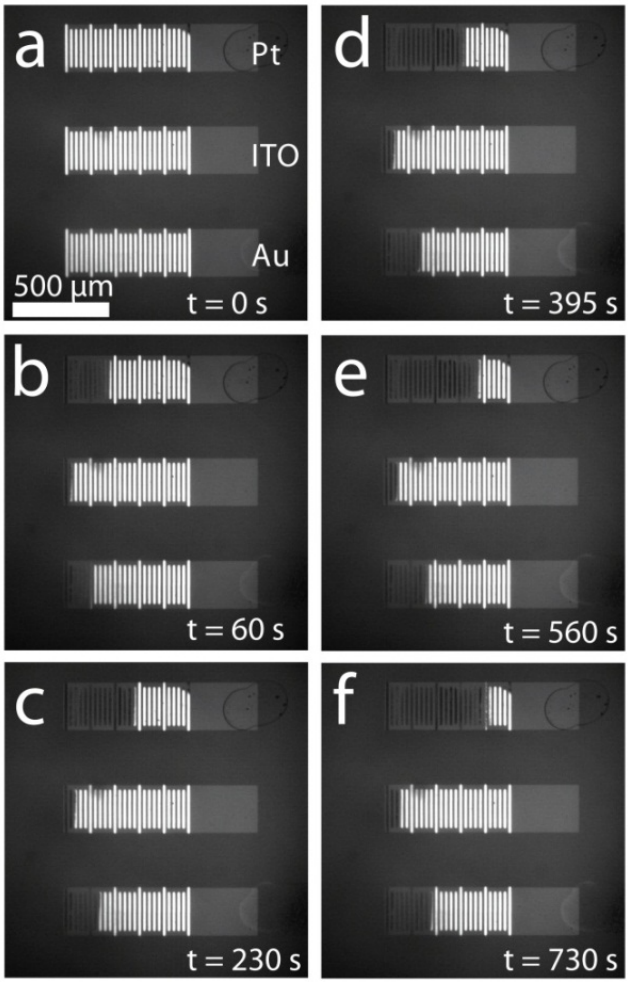

Figure 3.2. (a) Optical micrograph of 3 BPEs. The top BPE was spotted with G6-OH(Pt_{225}), the middle BPE was naked ITO, and the bottom BPE was modified with G6-OH(Au_{225}). The BPEs were placed in a microfluidic channel comprised of a silicone gasket and PDMS block. The channel was 12.5 mm long, 3 mm wide, and 0.5 mm tall and was filled with air-saturated, 0.10 M acetate buffer (pH 4.0). Two Ag/AgCl electrodes were used to apply E_{tot}. (b-f) Micrographs of the 3 BPEs after application of E_{tot} for the indicated times. E_{tot} = 10.0 V for the first 60 s of the experiment and 4.0 V thereafter. No further Ag electrodissolution was observed after 730 s (Frame f).

The higher initial E_{tot} reduces the time required for the analysis, but similar results are obtained when E_{tot} = 4.0 V throughout the duration of the experiment (Figure 3.3). No further Ag dissolution was observed after 730 s (Figure 3.2f). The key result is that the number of dissolved microbands depends on the activity of electrocatalyst present on the cathodic pole of the electrode. On the basis of four independent experiments, the number of the Ag microbands eliminated was 22 ± 1, 5 ± 1, and 8 ± 1, for the G6-OH(Pt_{225}), ITO, and G6-OH(Au_{225}) electrocatalysts, respectively. Compared to a continuous Ag anodic pole,[39] the Ag microbands simplify readout of the screening device because the number of discrete bands is easier to measure than the length. Of course, this digital readout approach comes at the expense of precision.

Comparing BPEs to Three-Electrode Experiments. The final numbers of Ag microbands dissolved for each electrocatalyst can be understood by comparing the results in Figure 3.2 with those obtained using a more typical 3-electrode electrochemical cell. The voltammograms shown in Figure 3.4a were collected using microfabricated ITO electrodes having dimensions of 250 x 250 µm, which is similar to the dimensions of the cathodic poles of the BPEs, and spotted with electrocatalysts in the same manner as for the BPE

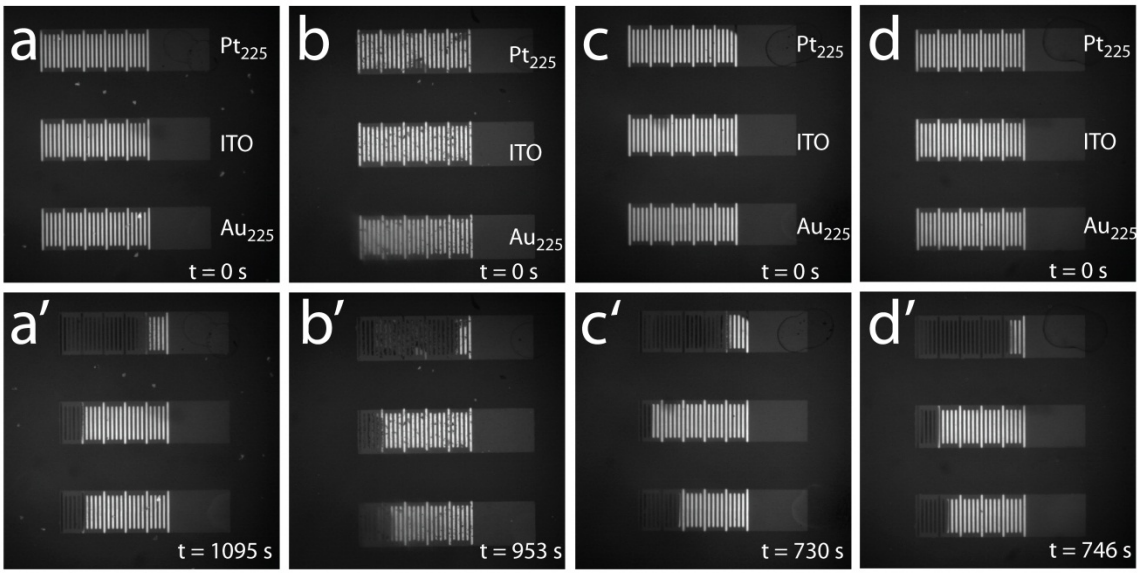

Figure 3.3. Four independent experiments like the one described for Figure 3.2 were carried out. The micrographs in this figure compare the results. The top row shows the electrode arrays before application of E_{tot}, and the bottom row shows the corresponding results at the end of the experiment. In all cases, the cathodic pole of the top electrode was modified with G6-OH(Pt_{225}) DENs, the middle electrode was naked ITO, and the cathodic pole of the bottom electrodes was modified with G6-OH(Au_{225}). Frames (a), (a'), (b), and (b') show the results when E_{tot} = 4.0 V during the entire experiment. Frames (c), (c'), (d), and (d') show results when E_{tot} = 10.0 V for the first 60 s of the experiment and E_{tot} = 4.0 V thereafter.

experiments. These data can be used to estimate the onset potentials (E_{onset}) required to drive the ORR on each of the three electrocatalysts. The values of E_{onset} for electrodes modified with G6-OH(Pt_{225}), G6-OH(Au_{225}), and Ag were determined from baseline-corrected CVs. They are defined as the potentials at which the current is 1% of that at the peak potential (measured from three independently prepared electrodes). The ITO electrode did not exhibit a local maximum in the current, so its value of E_{onset} was taken as the intersection of the extrapolated baseline and rising portion of the voltammogram. Because there is more uncertainty in this method, the average of ten electrodes was used. The values of E_{onset} for the G6-OH(Pt_{225}), ITO, and G6-OH(Au_{225}) electrocatalysts are 0.34 ± 0.01 V, -0.17 ± 0.03 V, and -0.06 ± 0.02 V (vs. Ag/AgCl, 1.0 M KCl). These values can be compared to the onset of oxidation (0.38 ± 0.02 V) of a thermally deposited, 20 nm-thick Ag film (black dashed line, Figure 3.4a). Figure 3.4b shows that there is a nearly linear relationship between the number of microbands dissolved and ΔE_{onset} ($E_{onset}^{ORR} - E_{onset}^{Ag\ Ox}$) for the electrocatalysts used here. This indicates that the number of microbands dissolved is directly related to the onset potential for the ORR.

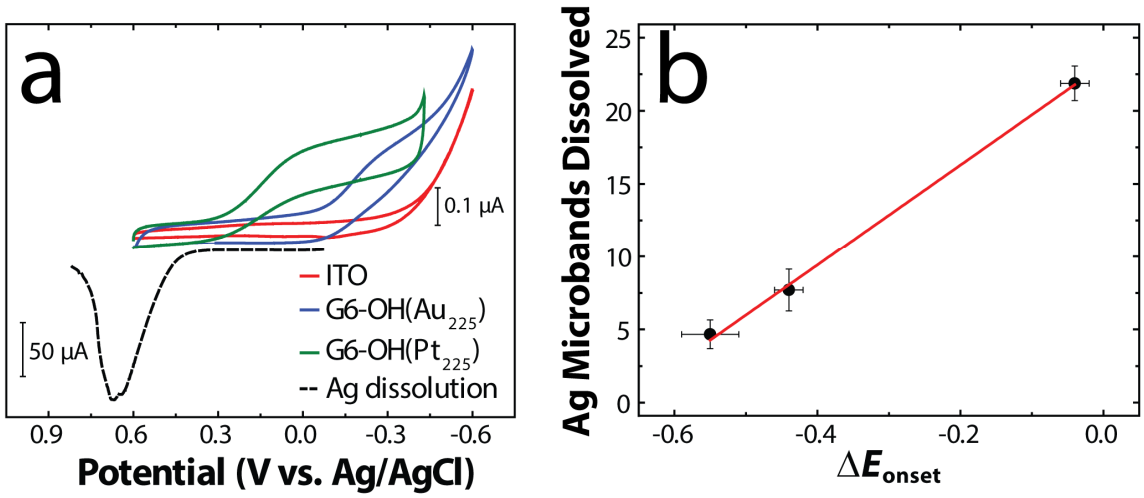

Figure 3.4. (a) The solid lines are CVs obtained using microfabricated ITO electrodes (250 x 250 µm) in a 3-electrode electrochemical cell. As indicated in the legend, one electrode was modified with Pt DENs, one with Au DENs, and one electrode was naked ITO. The cell contained 10 mL of an air-saturated, 0.10 M acetate buffer (pH 4.0), a Ag/AgCl reference electrode (1.0 M KCl, E = 0.222 V vs. NHE), and a Pt mesh counter electrode. The scan rate was 10 mV/s. The black dashed line is a linear sweep voltammogram of a thermally deposited, 20 nm-thick Ag film supported on a microfabricated ITO electrode (250 x 250 µm). The data were obtained using the same conditions as for the three CVs, except the scan rate was 50 mV/s. (b) Plot showing the number of dissolved Ag microbands versus ΔE_{onset} (as determined from the 3-electrode experiments) for the three catalysts. The red line is the best linear fit to the data, and the error bars represent one standard deviation from the average of the 3-electrode experiments (x-axis) and the BPE experiments (y-axis).

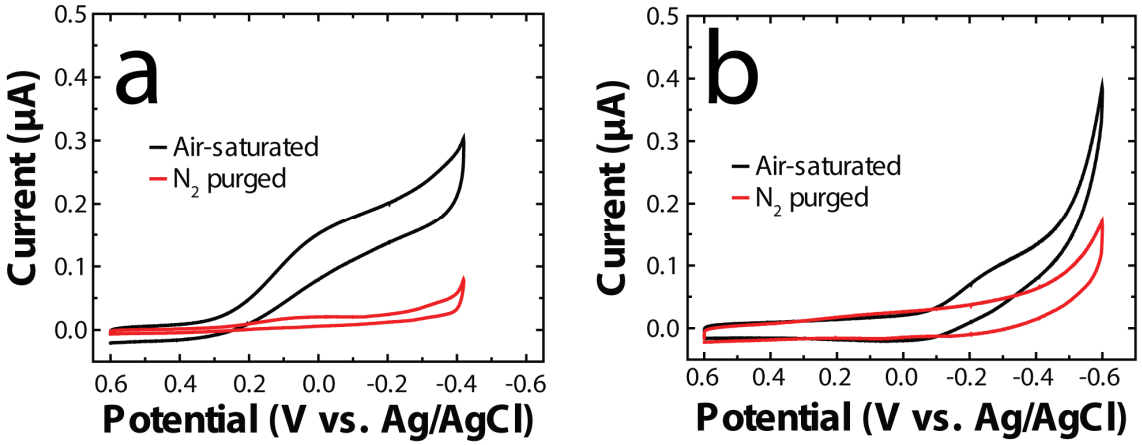

Figure 3.5. Cyclic voltammograms of dropcast (a) G6-OH(Au_{225}) and (b) G6-OH(Pt_{225}) on microfabricated ITO electrodes in air-saturated, 0.10 M acetate buffer (pH 4.0) (black) and the same solution after 20 min of N_2 purging (red).

To demonstrate that the ORR proceeded at more positive potentials than suspected background processes, microfabricated ITO electrodes were modified with Pt and Au DENS and then placed into air-saturated 0.10 M acetate buffer and a CV was collected (Figure 3.5). The solution was then purged with N_2 for 20 min and a second CV was collected.

3.5 Summary and Conclusions

In summary, the method reported in this chapter is suitable for rapid screening of large-scale arrays of electrocatalysts.[16] Importantly, there is a direct relationship between the activity of the electrocatalysts determined by voltammetry (Figure 3.4b) and the number of dissolved Ag microbands. This suggests that this method has the potential to provide quantitative kinetic information about electrocatalytic reactions. Finally, the Ag microband BPEs provide a permanent record of the electrocatalytic screen, which can be read out by simple optical microscopy.

Chapter 4: Parallel Screening of Electrocatalyst Candidates using Bipolar Electrochemistry

4.1 Synopsis

In this chapter we report simultaneous screening of bimetallic electrocatalyst candidates for the ORR using bipolar electrochemistry. The analysis is carried out by dispensing different bimetallic precursor compositions onto the cathodic poles of an array of BPEs, and then heating them in a reducing atmosphere to yield the catalyst candidates. Because BPEs do not require a direct electrical connection for activation, up to 33 electrocatalysts can be screened simultaneously by applying a voltage to the electrolyte solution in which the BPE array is immersed. The screening of the electrocatalyst candidates can be achieved in about 10 min. The current required to drive the ORR arises from oxidation of Cr microbands present at the anodic poles of the BPEs. Therefore, the most effective electrocatalysts result in oxidation (dissolution) of the most microbands, and simply counting the microbands remaining at the end of the screen provides information about the onset potential required to reduce oxygen. Here, we evaluated three Pd-M (M = Au, Co, W) bimetallic electrocatalysts. In principle, arbitrarily large libraries of electrocatalysts can be screened using this approach.

4.2 Introduction

In this chapter we report the rapid screening of bimetallic electrocatalyst candidates for the ORR using bipolar electrochemistry.[49] The important new result is that arrays of catalyst candidates can be screened in a highly parallel format that requires only simple instrumentation: a microscope and a DC power supply. As illustrated in Scheme 4.1a, the BPE screening devices consist of ITO electrodes having Cr microbands deposited at their anodic poles. Bimetallic catalyst candidates for the ORR are dispensed onto the cathodic poles. During a screening experiment, the BPE arrays are immersed in an acidic electrolyte solution, and a potential bias is applied between two driving electrodes positioned at either side of the array. The most effective catalyst candidates result in electrodissolution of the largest number of Cr microbands. Using this approach, we evaluated three potential bimetallic ORR electrocatalysts: Pd-Au, Pd-Co, and Pd-W.

Chapter 3 introduced a technique based on bipolar electrochemistry, where the electrodissolution of an array of thin metal microbands at the anodic pole of a BPE serves as an optical reporter of the performance of the catalyst immobilized on the cathodic pole.[43] BPEs have a number of desirable characteristics for parallel screening of electrocatalysts. First, because arbitrarily large arrays of

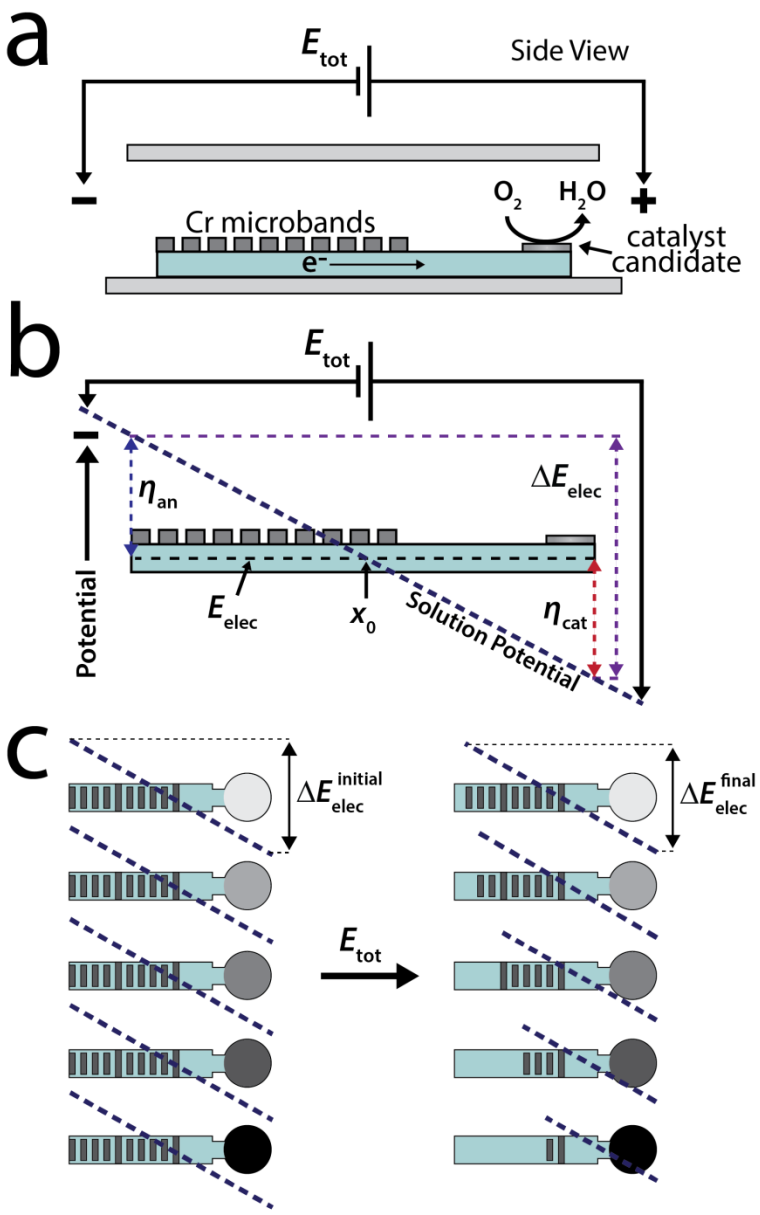

Scheme 4.1. (a) Side view of the bipolar electrochemical cell where the oxidation of Cr microbands is coupled to the ORR occurring at electrocatalyst candidates. (b) Schematic illustration of the distribution of potentials within the bipolar electrochemical cell. (c) Basic operating principle of the screening experiment and readout.

BPEs can be powered by a single pair of driving electrodes, individual electrodes in the array do not require a direct electrical connection.[16,35,46,49] Second, each BPE in an array can be selectively modified with a different electrocatalyst candidate.[36,43] Finally, the current passing through a BPE can be indirectly monitored using an optical readout based on either ECL[37,46] or electrodissolution of a thin metal film.[39,43,92]

After the report discussed in Chapter 3, other groups reported screening techniques based on bipolar electrochemistry, but they make use of "closed" bipolar electrodes (Scheme 1.4).[93] For example, Zhang and co-workers recently demonstrated a technique wherein an electrogenerated fluorescent probe is used to follow an electrocatalytic reaction.[60] In this configuration, BPEs provide the only electrical connection between two half cells.[59] Closed BPEs provide some advantages; for example, the two half cells may contain incompatible solutions, but it is difficult to ensure that the interfacial potential is the same for each electrode. The experiments reported in the present paper employ "open" BPEs, which reduce the magnitude of faradaic depolarization and minimize crosstalk between electrodes within the array.[37,50]

The selection of the bimetallic catalyst candidates used in this study is based on thermodynamic guidelines

proposed by Bard and co-workers.[72,73,94] This approach focuses on the direct mechanism of the ORR (eqs 4.1 and 4.2).

$$2M + O_2 \leftrightarrow 2MO \quad (4.1)$$

$$2M'O + 4H^+ + 4e^- \leftrightarrow 2M' + 2H_2O \quad (4.2)$$

In this scheme, molecular O_2 dissociates to yield adsorbed O (O_{ads}), and then O_{ads} is electroreduced to form H_2O. The guidelines suggest choosing a bimetallic system consisting of one metal (M) having a high $-\Delta G^\circ$ for the formation of a metal oxide (eq 4.1), and a second metal (M') that provides a positive standard potential for the reduction of the metal oxide (eq 4.2). Using these guidelines, we show that BPEs can be used to screen different ratios of three bimetallic compositions: Pd-Au, Pd-Co, and Pd-W. We chose these combinations for this study, because, within the context of these guidelines, they provide distinct cases. Pd-Au does not adhere to the basic guidelines proposed by Bard and co-workers, because both Pd and Au are both noble metals. Co and W represent species that readily form their respective oxides, with W having a more negative ΔG° for the reaction expressed by eq 4.1 than Co, -300 kJ/mol and -220 kJ/mol, respectively. Finally, combining Pd with Co or W adheres to the guideline, with Co and W facilitating eq 4.1 and Pd promoting eq 4.2. The standard potential of eq 4.2 for Pd is 0.92 V vs. NHE.[95]

4.3 Experimental Section

Chemicals. The following chemicals were used as received unless otherwise noted in the text: $(NH_4)_2PdCl_4$ (99.995%, Sigma Aldrich), $HAuCl_4 \cdot 3H_2O$ (99.9%, Sigma Aldrich), $Co(NO_3)_2 \cdot 6H_2O$ (99%, Fluka), $(NH_4)_6H_2W_{12}O_{40} \cdot xH_2O$ (≥ 98.5%, Fluka), H_2SO_4 (≥95%, trace analysis grade, Fluka), and ethylene glycol (99+%, Fisher Scientific). All aqueous solutions were prepared using Milli-Q water (18.2 Ω·cm). The concentration of the metal precursor solutions was 0.30 M (metal equivalent) and they were prepared in ethylene glycol.

Device Fabrication. ITO-coated glass slides (4-8 Ω/sq) (Delta Technologies, Loveland, CO) were patterned using standard photolithographic methods as shown in Scheme 2.1. The slides were cleaned by sonication (15 min each in 1% Triton-X 100 in water, water only, and ethanol). A positive-tone photoresist layer (PR1) (~10 µm thick, AZ P4620) was then spin-coated onto the ITO-coated slides and exposed to UV light through a photomask. The unmasked PR1 layer was removed in a developer solution. The pattern was transferred to the ITO layer by a plasma-assisted reactive ion etch (Oxford Instruments PlasmaLab 80+). Next, the protective PR1 layer was removed using acetone, and the device was cleaned

by sonication in 1% Triton-X, water, and ethanol. A negative lift-off photoresist (PR2) (~0.5 µm-thick, ma-N 1405, MicroChem Corp., Newton, MA) was deposited by spin-coating, exposed to UV light under a negative mask, and developed to remove photoresist over portions of the BPE anode. A 5 nm-thick layer of Cr was deposited by physical vapor deposition (PVD) over the devices. The unwanted Cr was removed by lift-off (dissolution in acetone), leaving the microband array at each BPE anode. The devices were cleaned *via* sonication and dried under N_2 prior to dispensing precursor salts on the BPE cathodes. Each BPE is 2.50 mm long, with a 325 µm-diameter disk comprising the cathode. The lateral spacing of BPEs in the array is 750 µm center-to-center. The functional anode of each BPE consists of 70 individual Cr microbands (10 µm microbands and 10 µm edge-to-edge spacing, see Scheme 4.2). This device design was selected because crosstalk between neighboring electrodes was expected to result in less than 1% deviation in current flow at each electrode, as determined by finite-element simulations (Figure 4.1).

Catalyst Candidate Preparation. The preparation of electrocatalyst candidates is depicted in Scheme 4.3. Precursor solutions were dispensed onto the cathodic poles of the BPEs in the array using a robotic positioner / piezo-jet controller (CHI 1560A, CH Instruments, Austin, TX)

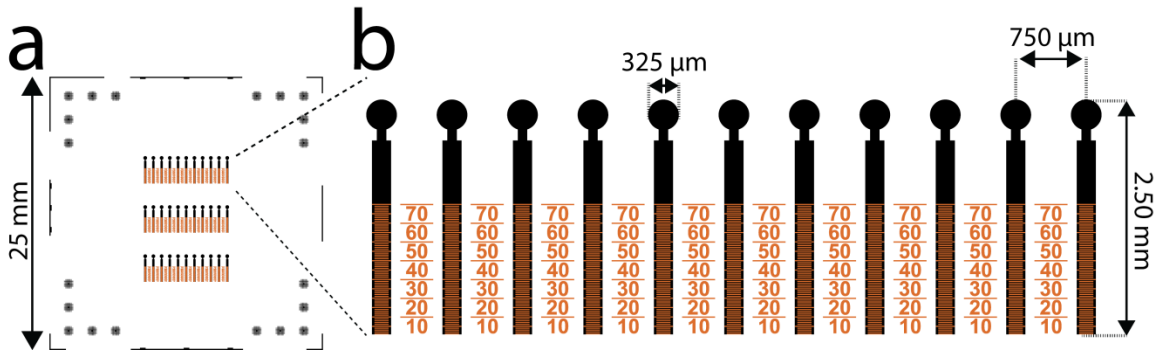

Scheme 4.2. (a) Schematic of the device design for screening bimetallic electrocatalyst candidates for the ORR using BPEs. The black portions of the design result in ITO and the burnt orange features result in Cr. The device design produces 3 rows of 11 electrodes (33 total). (b) Zoom in of one row of the device design. The electrodes within a row are spaced by 750 µm center-to-center. Each electrode in the array is 2.50 mm long, has a cathodic pad consisting of a 325 µm diameter circle, and is modified with an array of 70 individual Cr microbands. The microbands are 10 µm long and are spaced by 10 µm edge-to-edge. The schematic is drawn to scale in each frame.

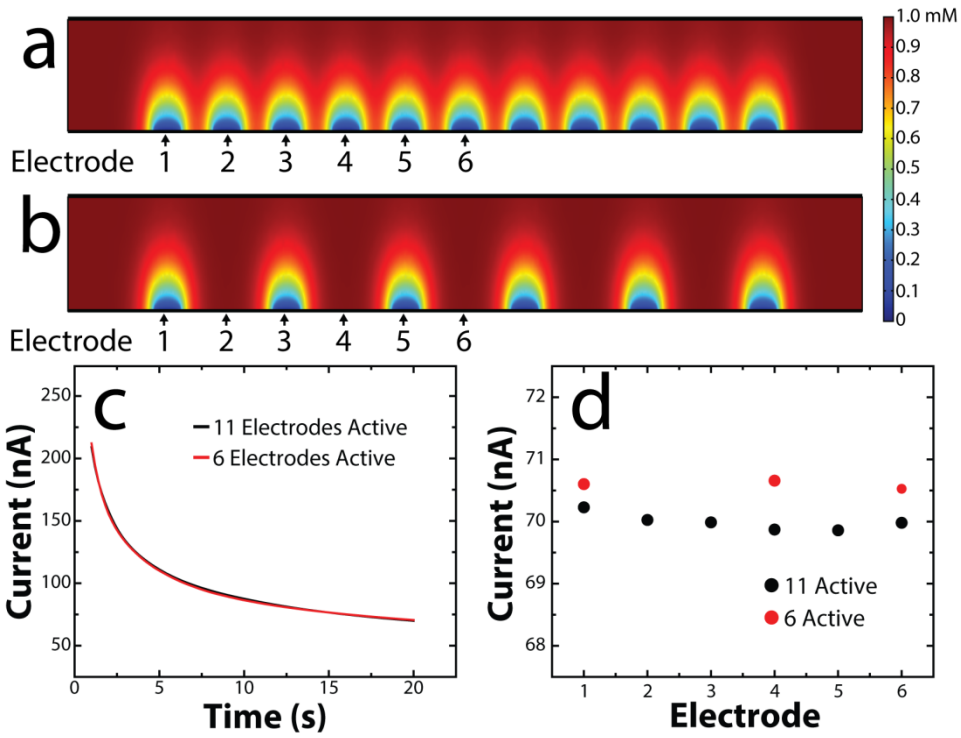

Figure 4.1. Evaluation of crosstalk in the array design. (a) 2D concentration profiles for the reversible reduction of a model species (O + e = R, C_O = 1 mM) after 20 s of operation under mass transport limited conditions in the same cell geometry used for the screening experiments discussed in the main text (cell height = 0.5 mm, cell width = 1 cm) when 11 electrodes (325 µm width, 750 µm center-to-center separation) are active. (b) 2D concentration profiles for the same geometry as (a), but with only 6 electrodes active. (c) Simulated current response vs. time for the electrodes in the model shown in (a) and (b). (d) Simulated current response at t = 20 s for the models shown in (a) and (b). The percent difference between the two models is less than 1%, demonstrating a low amount of electrochemical crosstalk between electrodes in the array.

fitted with a printhead assembly (PH046H-AT, Microfab, Plano, TX) containing 4 piezodispensers (80 µm tip diameter, Microfab).[96]

The electrodes were aligned under the printhead using an *x*,*y*,*z*-micropositioner and the dispensing alignment and progress were monitored *via* a USB microscope placed under the stage. The arrays were spotted using a total of 10 drops (~300 pL/drop) of the precursor solutions to maintain the total number of moles of metal constant on each electrode. The compositions were varied by changing the number of drops of each precursor solution (10-0, 9-1...1-9, 0-10). These compositional variations require 11 electrodes to produce the full range. Accordingly, each BPE device includes 3 rows of 11 electrodes, allowing each composition to be simultaneously screened in triplicate.

The dispensed precursor solutions were dried in a vacuum oven (70 °C) for 5 min to promote even coverage of metal precursors over the surface of the BPE cathode. The spotted materials were then reduced in flowing gas (5% H_2/95% N_2) for 1.5 h at 350 °C. The effects of heating to this temperature were determined to have no deleterious effects on the ITO substrates (Figure 4.2). Figure 4.3 shows the spotting accuracy achieved for 256 electrodes used in this study.

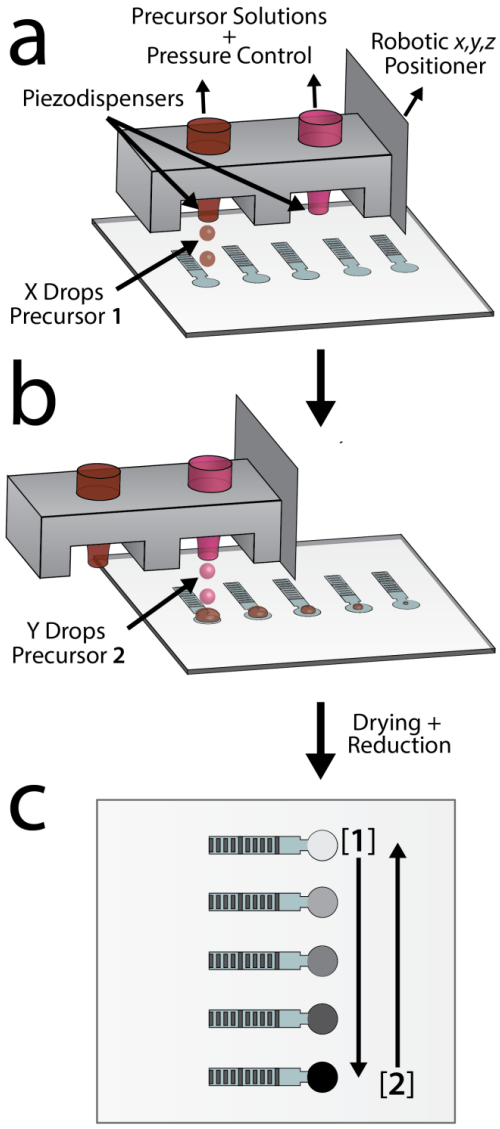

Scheme 4.3. Schematic illustration of the piezodispensing process. Two dispensers are used to create a bimetallic compositional variation across the BPE array. A varying number of drops of precursor 1 are dispensed onto the cathodic pads of the BPE array (a). Then the dispenser head is moved so that the second dispensing tip can add another set of drops of precursor 2 to the same BPE array. (c) The precursor droplets are dried and then reduced in a tube furnace.

BPE Array Screening. After chemical reduction of the precursor spots, the arrays were placed into a bipolar electrochemical cell (Figure 4.4). The cell uses two 0.5 mm-thick silicone gaskets as channel walls, which are placed between the slide containing the BPE array (top) and a microscope slide (bottom) (25 x 36 mm). Glassy carbon (GC) driving electrodes were placed on top of the bottom substrate and ~2.5 mm from the edge of the device to prevent bubbles from entering in the channel. A voltage was applied between the two GC driving electrodes to produce the electric field in the bipolar electrochemical cell. The width of the microfluidic space was 1 cm for all experiments and the volume of the resulting cell was ~125 µL. Screening of the BPE arrays was started within 5-6 min of the addition of air-saturated, 0.10 M H_2SO_4 electrolyte solution. E_{tot} = 15.0 V was applied for 5 min using a DC power supply (Lambda LLS9120, TDK-Lambda, Neptune, NJ). Finally, the cell was disassembled and the BPEs were gently rinsed with water and dried under N_2.

The arrays were imaged using a Canon EOS Rebel T3i digital single-lens reflex (DSLR) camera connected to a Nikon AZ100 microscope using a Varimag II adapter (CNC Supply, Cape Coral, FL). The DSLR camera provides greater spatial resolution (full frame = 5824 x 3456 pixels) than a traditional CCD camera, but at the expense of rapid image

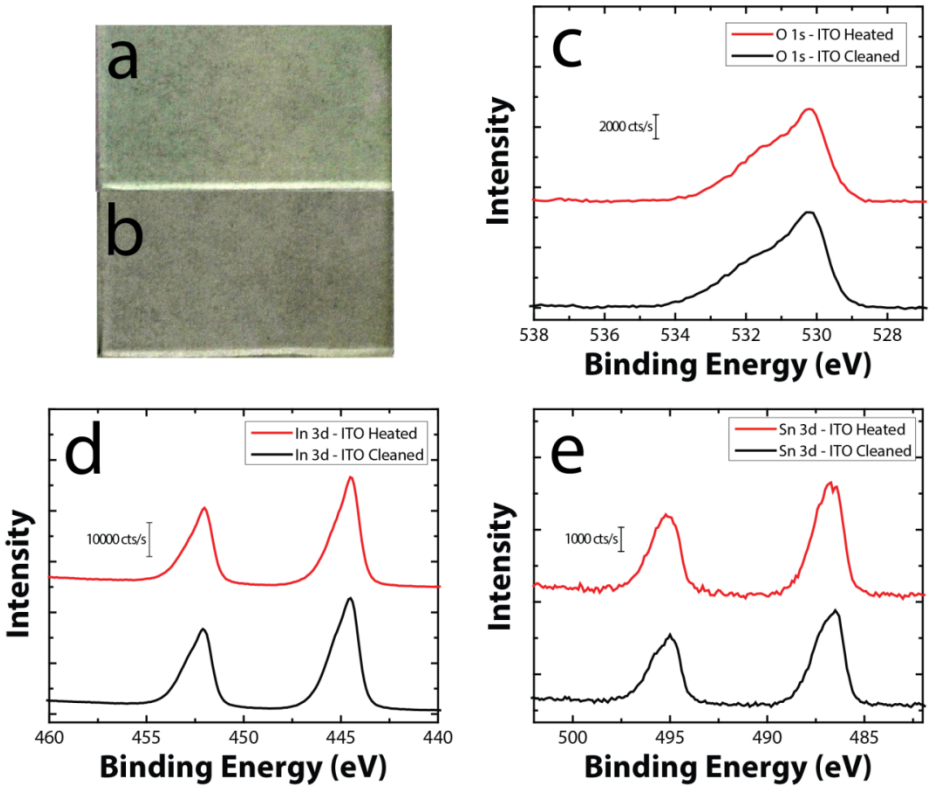

Figure 4.2. Effect of heating ITO to 350 °C 1.5 h in an atmosphere of 5% H_2 / 95% N_2. This is required to produce the electrocatalyst candidates. Optical images of an ITO-coated glass slide as received (a) and after heating (b). A slight color change is apparent, and four-point probe measurements of the two ITO coatings indicated a decrease of about 10% in sheet resistance after heating (before = 4.8 Ω/sq, after = 4.4 Ω/sq). (c-e) High-resolution X-ray photoelectron spectra of the ITO surface before (black) and after (red) heating: (b) O 1s, (c) In 3d, and (d) Sn 3d.

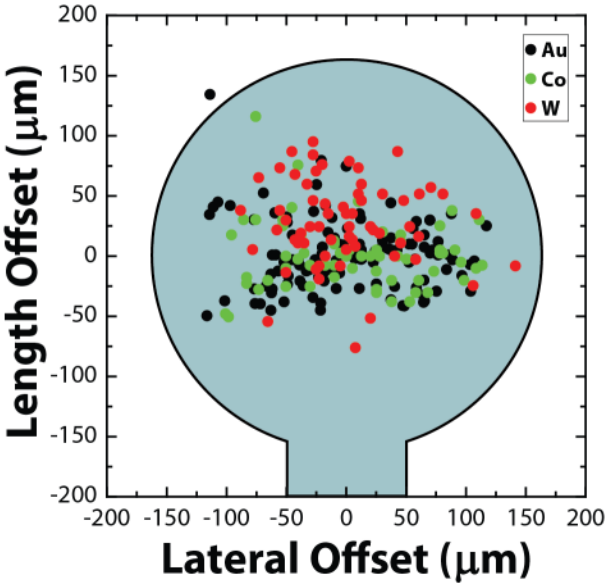

Figure 4.3. Spotting accuracy for 256 individual electrodes as determined from optical micrographs of BPE cathodes. The position indicates the centroid of the piezodispensed catalyst candidate relative to the center of the BPE cathodic pad.

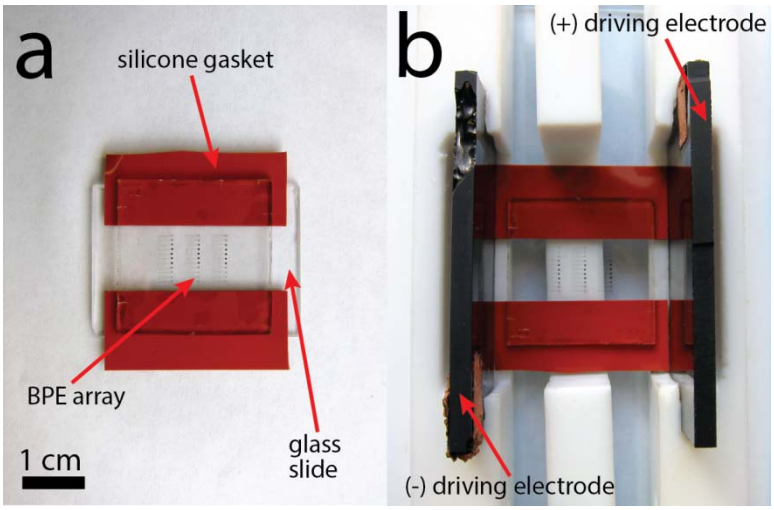

Figure 4.4. Photographs of the bipolar electrochemical cell used in these experiments. (a) The basic components of the cell that define the fluidic space. (b) The fully assembled cell, including the GC driving electrodes.

capture (1-3 fps). With this system, 10 μm features can be resolved over a field of view of ~9 x 5 mm. Images were processed using ImageJ software (NIH, Bethesda, MD).

Compositional Analysis. The elemental compositions of deposited materials were determined using a Quanta 650 FEG ESEM system with a Bruker XFlash 5010 EDS detector. Bimetallic spots were first prepared on naked ITO to ensure reproducible dispensing. Examples of the resulting test spots are shown in a series of micrographs in Figures 4.5-4.7. SEM-EDS analysis of screened materials was achieved by grounding the BPEs to the SEM sample holder with a thin strip of carbon tape.

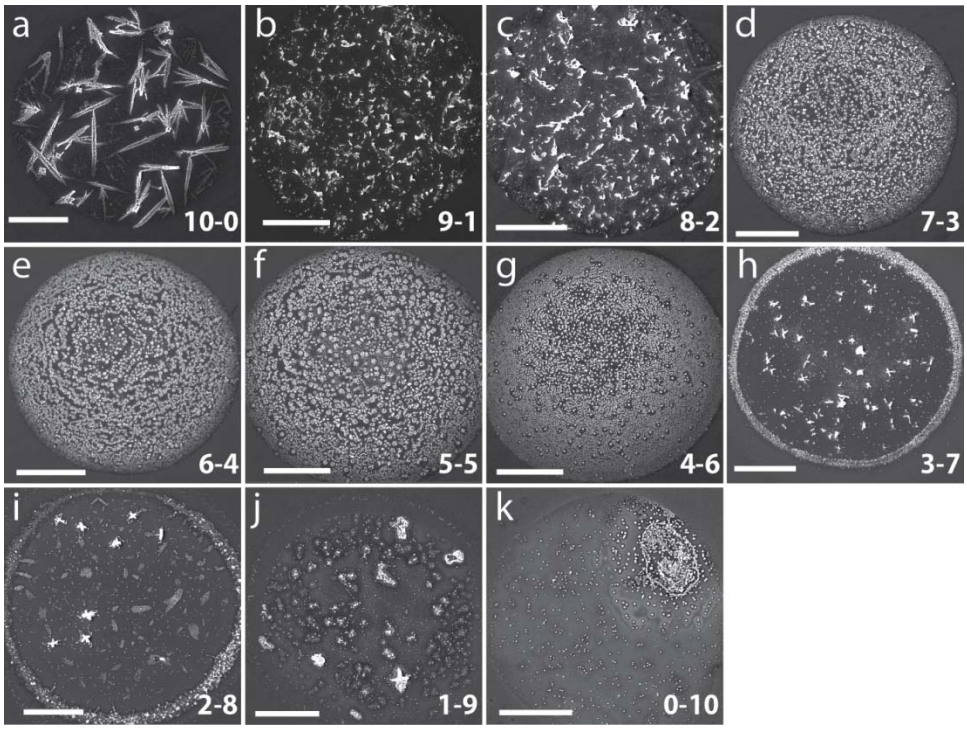

Figure 4.5. SEM micrographs of varying compositions of Pd-Au. The first number in the lower right of each frame indicates the number of drops of Pd precursor and the second number indicates the number of drops of Au precursor. The compositions range from (a) Pd_{10}-Au_0 to (k) Pd_0-Au_{10}. The white scale bars represent 100 µm. The precursor solutions used for piezodispensing were 0.30 M $(NH_4)PdCl_4$ and 0.30 M $HAuCl_4 \cdot 3H_2O$ in ethylene glycol. The films were reduced in flowing 5% H_2 / 95% N_2 at 350 °C for 1.5 h.

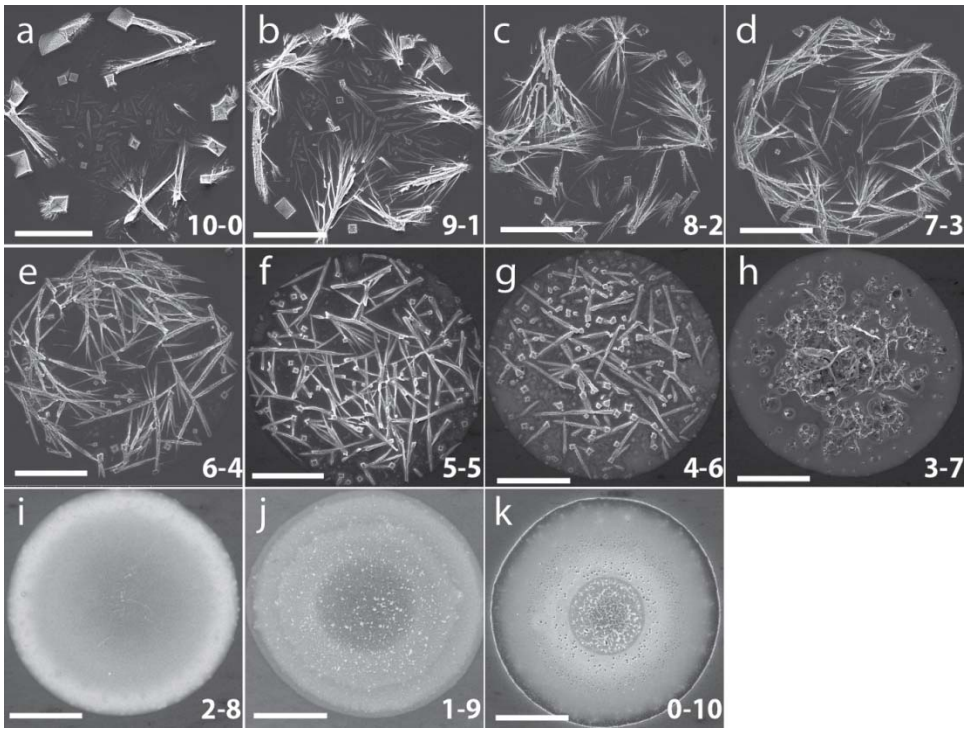

Figure 4.6. SEM micrographs of varying compositions of Pd-Co. The first number in the lower right of each frame indicates the number of drops of Pd precursor and the second number indicates the drops of Co precursor, from Pd_{10}-Co_0 (a) to Pd_0-Co_{10} (k). The white scale bars indicate 100 µm. The precursor solutions used for piezodispensing were 0.30 M $(NH_4)PdCl_4$ and 0.30 M $Co(NO_3)_2 \cdot 6H_2O$ in ethylene glycol. The films were reduced in flowing 5% H_2 / 95% N_2 at 350 °C for 1.5 h.

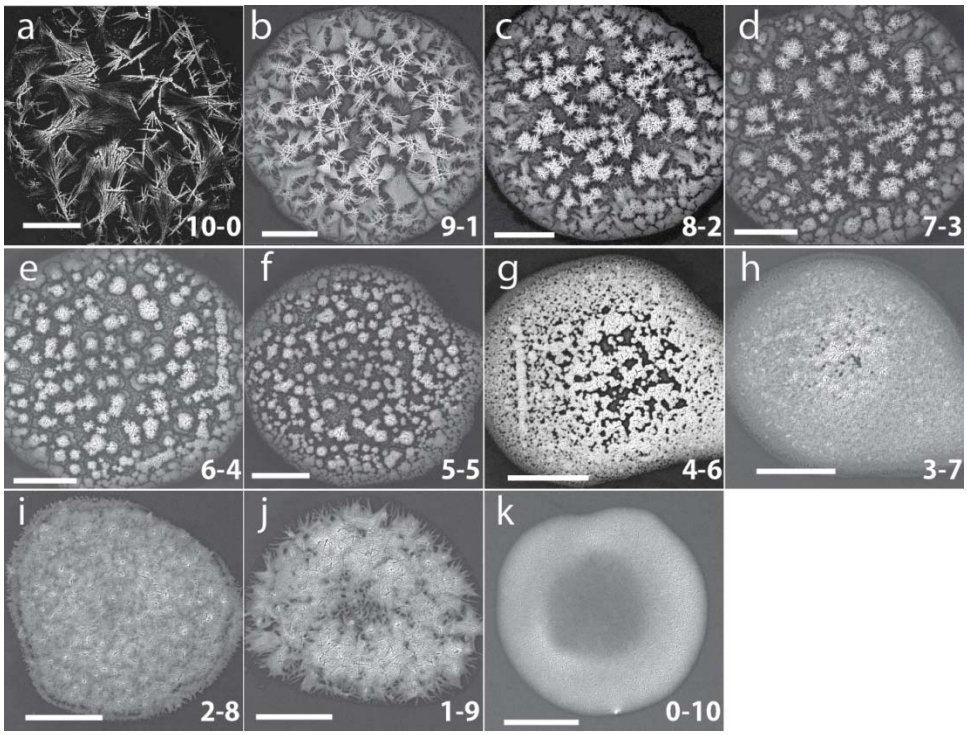

Figure 4.7. SEM micrographs of varying compositions of Pd-W. The first number in the lower right of each frame indicates the number of drops of Pd precursor and the second number indicates the drops of W precursor, from Pd_{10}-W_0 (a) to Pd_0-W_{10} (k). The white scale bars indicate 100 µm. The precursor solutions used for piezodispensing were 0.30 M $(NH_4)PdCl_4$ and 0.30 M $(NH_4)_6H_2W_{12}O_{40}\cdot xH_2O$ in ethylene glycol. The films were reduced in flowing 5% H_2 / 95% N_2 at 350 °C for 1.5 h.

4.4 Results and Discussion

Operating Principles of the BPE Screening System. The operating principles of BPEs have been described in earlier chapters, but will be reviewed briefly here. A BPE is an electrically conductive material that responds to an electric field applied to an electrolyte solution by an external power supply (E_{tot}, Scheme 4.1a). In the absence of a direct electrical connection the BPEs float to an equilibrium potential (E_{elec}) which is equal to the solution potential above the BPE at a certain point (x_0) along the electrode's length. When the electric field in solution is sufficiently high, faradaic reactions occur at the poles of the BPE. This is because the interfacial potential differences, or overpotentials (η), between the electrode and solution vary across the length of the electrode. The BPE experiences both anodic (η_{an}) and cathodic (η_{cat}) overpotentials, with the highest overpotentials appearing at the extremities (Scheme 4.1b). The fraction of E_{tot} that is dropped over each electrode (ΔE_{elec}) depends on the length of the BPE relative to the length of the fluidic channel ($l_{channel}$, eq 1.1).

In the experiments reported here, we take advantage of this relationship to evaluate electrocatalyst candidates. As shown in Scheme 4.1a, the application of a sufficiently high

E_{tot} powers electrically-coupled faradaic reactions at the BPE: the electrodissolution of Cr microbands and the ORR at the catalyst candidates. The highest overpotentials occur at the extreme ends of each BPE (Scheme 4.1b), meaning that the first microband to dissolve is the one closest to the edge of the BPE anode. In a microband dissolution experiment, the effective length of each BPE decreases as the number of microbands eliminated increases.[39,43,92] This means that the overpotentials available to drive the two electrochemical reactions decrease over the course of the experiment and the rate of dissolution (and current) becomes very small, such that it effectively ceases. Because the electrochemical behavior of Cr oxidation is the same for each microband in the array, it is possible to estimate the relative onset potentials (E_{onset}^{ORR}) for each catalyst candidate by counting the number of Cr microbands that dissolve over the course of the experiment. The use of Cr microbands, rather than a continuous Cr film, is used to simplify analysis of the experimental results.

Preliminary Testing of the BPE Array. For meaningful results to emerge from this type of screening study, it is essential that the electric field within the device be uniform. Accordingly, we carried out the following experiment to test this important point. First, a naked

electrode array (no catalyst candidates) was configured within the bipolar electrochemical cell. Second, the cell was filled with 5.0 mM *p*-benzoquinone (BQ), which is readily reduced on unmodified ITO BPEs. BQ is a convenient species for control studies as the onset potential difference between BQ reduction and Cr oxidation is nearly 1 V (Figure 4.8). Third, E_{tot} = 15.0 V was applied to the cell for 5 min. No additional electrodissolution of Cr was observed after this time, because at this point the BPEs have shortened such that E_{elec} is insufficient to drive additional faradaic processes.

The results of this experiment are shown in Figure 4.9. Before application of the driving voltage (Figure 4.9a), all 70 Cr microbands are visible on each of the 11 BPEs shown. However, after the external voltage is applied, Figure 4.9b shows that a number of microbands at the bottom of each ITO strip have oxidized and dissolved. If the field is uniform, then the same number of Cr microbands should be removed from each BPE. Figure 4.9c is a histogram showing the number of Cr microbands removed from each of the 33 BPEs in the array. The average number of bands eliminated is 20.9 ± 0.5, which corresponds to a precision of 2%. The key conclusion is that each of the 33 electrodes behaves nearly identically. Another important outcome of this experiment is that because the E_{onset} for BQ reduction and Cr electrodissolution, $E_{onset}^{Cr\ Ox}$,

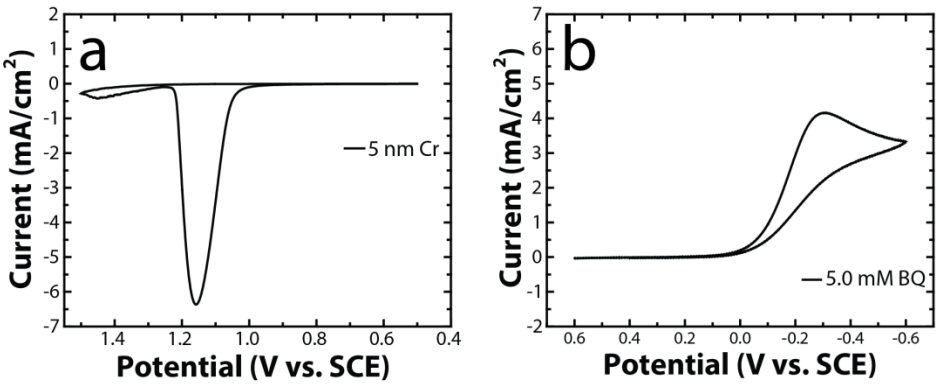

Figure 4.8. (a) Stripping voltammogram for a 5-nm thick Cr film deposited onto an ITO electrode. The electrolyte was 0.10 M H_2SO_4 and the scan rate was 50 mV/s. The onset potential (E_{onset}) is here defined as the potential when the current is 1% of the peak current, and it was determined to be 0.98 V vs. SCE. (b) Cyclic voltammogram for 5.0 mM BQ. The electrolyte solution was 0.10 M H_2SO_4 and the scan rate was 100 mV/s. E_{onset} for BQ reduction was determined to be 0.07 V vs. SCE.

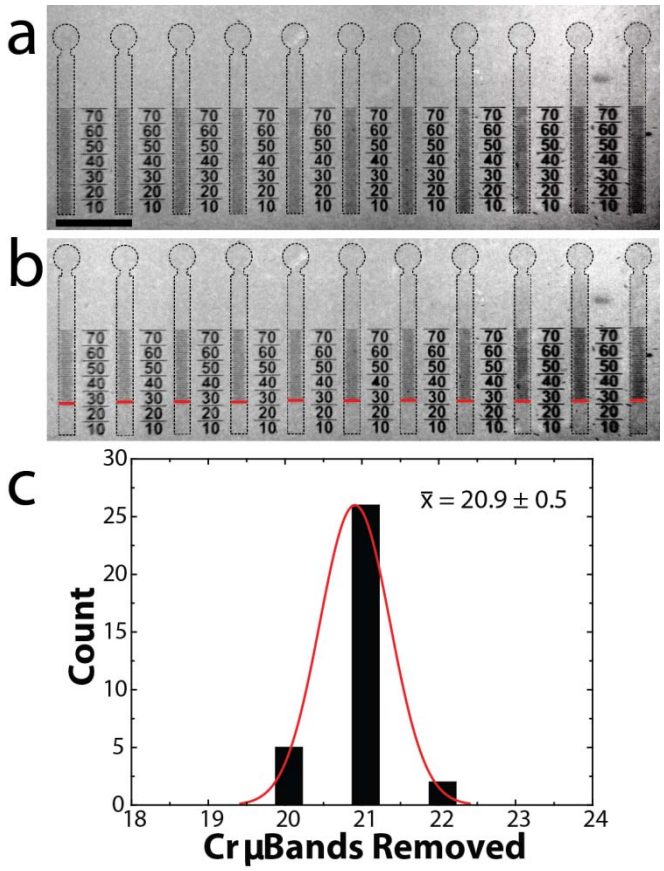

Figure 4.9. Results demonstrating the reproducibility of the BPE arrays used to screen catalysts. (a) Optical micrograph of a single row of 11 BPEs prior to electrochemical analysis. The black scale bar represents 1.0 mm. The ITO portions of the BPEs have been outlined (black dashed line) for clarity. (b) The array in (a) after application of E_{tot} = 15.0 V for 5 min. The BPE cell was filled with a solution containing 5.0 mM BQ and 0.10 M H_2SO_4. The red lines indicate the lowest microband on each BPE that did not undergo electrodissolution. (c) Histogram showing the number of Cr microbands dissolved for the 33 BPEs in the full array. The solid red line shows the normal distribution for this histogram.

can be determined independently using a traditional 3-electrode electrochemical cell, it is possible to estimate the onset potentials for the ORR in the bipolar electrochemical cell.

Using eq 1.1 and the strength of the electric field, the value of ΔE_{elec} at the end of the experiment, ΔE_{elec}^{final}, can be calculated by counting the number of Cr microbands eliminated and using the value of $E_{onset}^{Cr\ Ox}$ to determine E_{onset}^{ORR} for each catalyst composition (eq 4.3).

$$E_{onset}^{ORR} \approx E_{onset}^{Cr\ Ox} - \Delta E_{elec}^{final} \qquad (4.3)$$

This means that E_{onset}^{ORR} for each species is directly related to the number of Cr microbands that dissolve during the screening experiment. We have directly measured the electric field in the bipolar electrochemical cell using a series of Au microbands patterned within the microfluidic space (Figure 4.10). The field is quite uniform and has a value of 0.46 V/mm. It is important to note that the values of E_{onset}^{ORR} have been estimated using experimentally determined parameters. Therefore, these values are most reliable for *comparing* the ORR onset potentials for the catalyst candidates examined in this study rather than as absolute values.

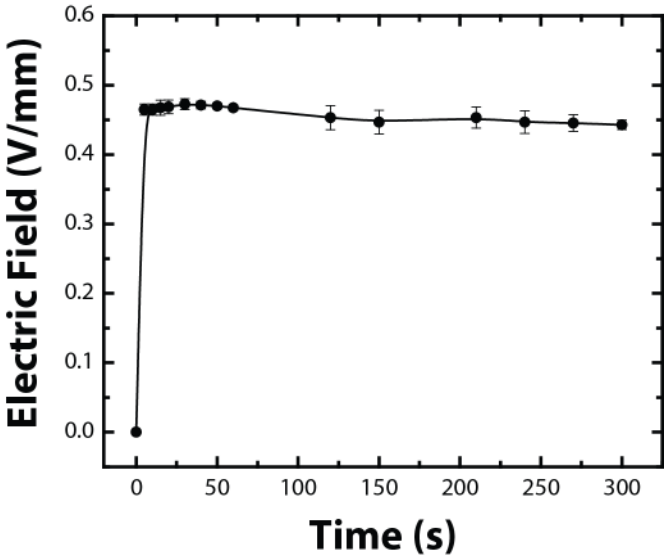

Figure 4.10. Electric field measurements showing the electric field strength within the bipolar electrochemical cell. A cell configured with ten 100 µm-wide Au microbands separated by 1.25 mm center-to-center was placed in the bipolar electrochemical cell shown in Figure 4.4. The electrolyte was 0.10 M H_2SO_4 (same as the screening experiments). E_{tot} = 15.0 V was applied using a pair of glassy carbon driving electrodes and the potential difference between two electrodes separated by 3.75 mm center-to-center was measured using a digital multimeter (Keithley 6517B). The error bars indicate one standard deviation from the mean for three replicate experiments.

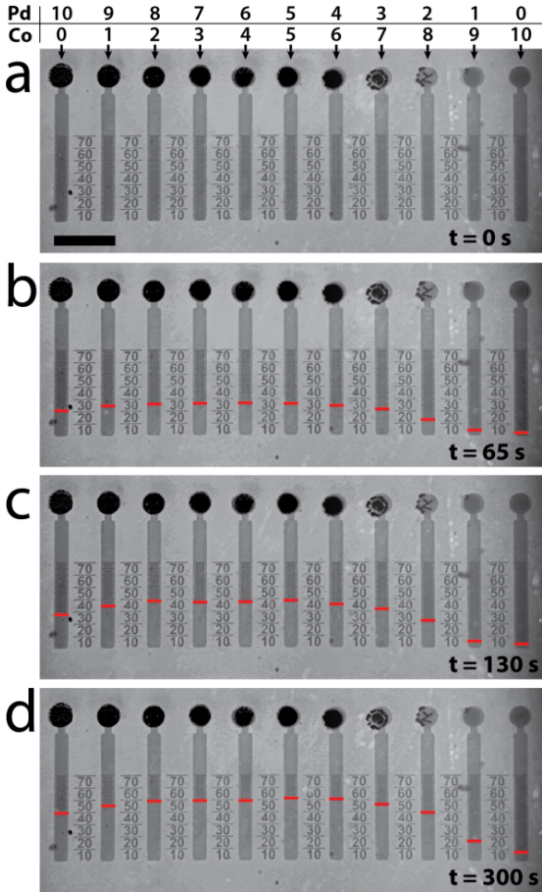

Figure 4.11. Optical micrographs representing a BPE ORR electrocatalyst screening experiment of different Pd-Co compositions. The electrode configuration is the same as that shown in Figure 4.9, except the cathodic poles of the BPEs have been modified with the different atomic ratios of Pd and Co indicated at the top of figure. The black scale bar represents 1.0 mm. The bipolar electrochemical cell was filled with ~125 µL of air-saturated 0.10 M H_2SO_4. (a) Prior to the application of a driving voltage. (b-d) After application of E_{tot} = 15.0 V for the times indicated in the bottom-right corner of each frame. The white lines show the position of the lowest microband on each BPE that did not undergo electrodissolution. Figure 4.6 shows a series of SEM micrographs of the Pd-Co system, like that tested on this array.

Screening Bimetallic Systems. Each BPE device is configured so that an array of bimetallic compositions can be screened in triplicate in <10 min. Figure 4.11 shows the outcome of a BPE screening experiment for 11 Pd-Co electrocatalyst compositions. Figure 4.11a is an optical micrograph of the array prior to the application of E_{tot}. The remaining frames show the evolution of the screening experiment at the times indicated in the individual frames. The red lines spanning the width of each BPE indicate the location of the bottom-most microband on each BPE that did not undergo electrodissolution. The histograms in Figure 4.12 show the average number of Cr microbands removed for each composition of the three bimetallic electrocatalyst candidates examined in this study. The error bars represent the standard deviation from the mean obtained for a minimum of 3 independently prepared devices. That is, a total of at least 9 screens for each composition. The number of Cr bands oxidized for the 33 independently tested Pd-only electrocatalysts was 36.2 ± 3.9. From this value, and using eq 4.3, we estimate E_{onset}^{ORR} = 0.46 ± 0.04 V vs. RHE. A similar analysis indicates that E_{onset}^{ORR} for pure Au is 0.17 ± 0.02 V vs. RHE. In the case of the bimetallic Pd-Au candidates (Figure 4.12a), only a few of the compositions exhibit enhanced ORR activity compared to Pd only.

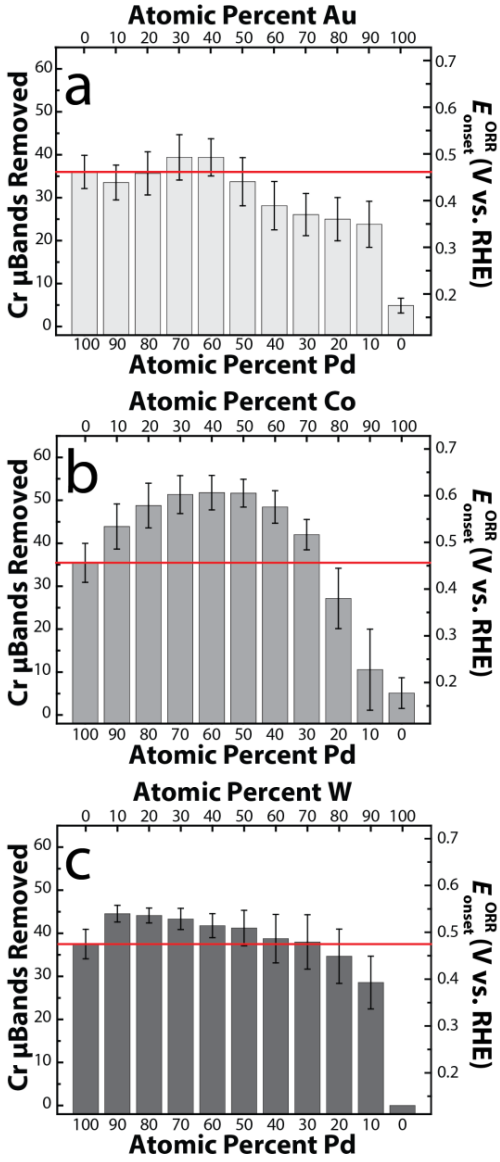

Figure 4.12. Histograms indicating the number of Cr microbands removed for each bimetallic composition tested: (a) Pd-Au, (b) Pd-Co, and (c) Pd-W. Each composition was tested in triplicate using at least 9 separate BPEs. The error bars represent one standard deviation from the mean for each composition. The solid red lines indicate the performance of the 100% Pd material.

This is in accord with expectations based on the guidelines discussed earlier. For example, Pd_6-Au_4 revealed a statistically significant difference over Pd-only at the 95% confidence level. However, even in this case the bimetallic only resulted in three more oxidized bands, which is equivalent to less than a 50 mV difference in E_{onset}^{ORR}.

A number of factors could be responsible for the ~±10% variation indicated by the error bars in Figure 4.12. First, the electrocatalyst candidates are heterogeneous. SEM micrographs highlighting this observation are shown in Figures 4.5-4.7. For example, micrographs of the Au-only catalyst reveal the presence of Au nanoparticles on the ITO support. This heterogeneity is important, because toward the end of each screening experiment only the distal edge of the cathode of each BPE is active for the ORR (that is, only the longest dimension of the BPE is important). Heterogeneity in catalyst composition at this location will result in some scatter in the number of Cr microbands that dissolve. Second, for the same reason, slight differences in the location of the catalyst on the BPE cathode will also lead to some uncertainty in the results. The variation in the location of the spotted catalyst is approximately ±30 μm in the direction parallel to the long axis of the electrodes (Figure 4.3).

Of the three bimetallic ORR electrocatalyst compositions studied, the Pd-Co materials exhibit the most positive shifts of E_{onset}^{ORR} (Figure 4.12b). This result is consistent with those obtained by others using different electrochemical methods. For example, SECM results indicate that Pd_8-Co_2 is the most active composition for the ORR.[72,73,97] Our data indicate that materials containing 30-90% Pd exhibit much more positive E_{onset}^{ORR} values compared to pure Pd. For example, E_{onset}^{ORR} for Pd_6-Co_4 is 0.61 ± 0.04 V vs. RHE compared to 0.46 ± 0.04 V for the Pd-only catalyst. Several experimental and theoretical reports indicate that Pd-Co compositions ranging from Pd_9-Co_1 to Pd_6-Co_4 should show the greatest activity for the ORR.[72,98-102]

It is important to point out here that the true identity of the most active phase in a certain compositional range is difficult to know with certainty (all electrochemical screening methods that rely on catalysts prepared by the method reported here suffer from this same problem). For example, as shown in Figure 4.6, the morphologies of the Pd-Co materials are quite heterogeneous even for a particular composition. Moreover, the Pd-Co system is not entirely stable in acidic electrolyte. In our experiments, dissolution of Co from the surface of the BPEs is apparent from micrographs collected during the screening

experiments, and EDS results obtained after screening indicate a marked change in final composition (Figure 4.13b). For example, EDS analysis indicates that after screening the compositions of the Pd-Co bimetallics typically contain 60-90% Pd, depending on the initial percentage of Pd present. This compositional change accounts for the surprisingly high E_{onset}^{ORR} for the catalysts having a nominally low percentage of Pd. The point is that loss of Co from the BPE cathodes increases the Pd:Co ratio but also lowers the overall metal loading, and these factors compromise the assumed catalyst structure-function relationship to some extent.

The Pd-W bimetallics (Figure 4.12c) represent the most extreme differences in the $-\Delta G^{\circ}$ values for the reaction shown in eq 4.1 and the standard reduction potential for the reaction shown in eq 4.2 for the two materials. As has been shown previously, the presence of W in bimetallic compositions containing 50–90% Pd does result in some improvement in electrocatalytic behavior compared to the Pd-only catalyst.[103] Like the Pd-Co catalyst, the Pd-W system also exhibits some loss of W in the acidic electrolyte. However, this effect is much less pronounced for the Pd-W electrocatalyst (Figure 4.13b).

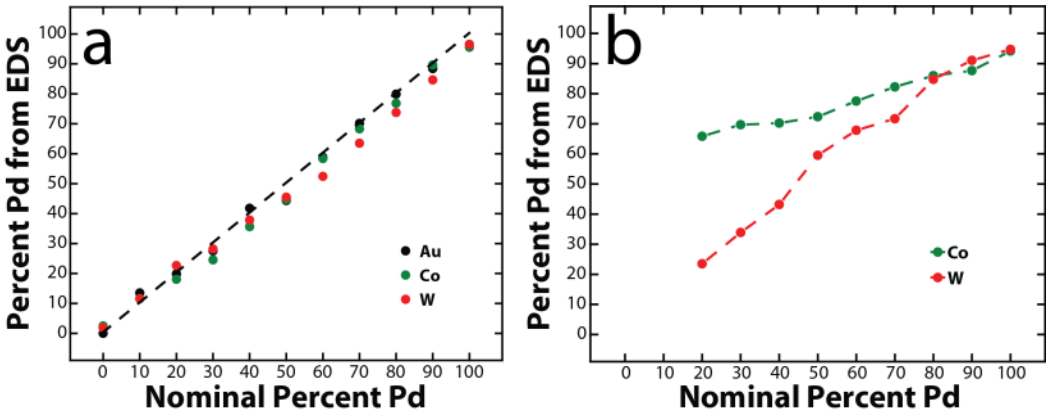

Figure 4.13. EDS analysis of spotted electrocatalyst candidates. Elemental compositions of the catalyst candidates were estimated (a) before and (b) after screening experiments. (b) Plot of relative at% Pd for Pd-Co and Pd-W vs. the nominal at% Pd dispensed onto the BPE cathode.

Optical Determination of Current. Thus far we have only discussed the total number of microbands remaining at the end of a screening experiment, and then correlated these data to the onset potential of the ORR. This only requires a single micrograph, such as that shown in Figure 4.11d, obtained at the end of a screening experiment. However, one of the main virtues of this catalyst-selection method is that it is nearly as straightforward to capture the time evolution of the entire BPE array *in situ*. For example, Figure 4.14 is a plot of the number of bands dissolved vs. time for a BPE array spotted with different Pd-Co compositions. Because each Cr microband represents a certain quantity of charge, it is possible to correlate such data to the current flowing through each BPE.

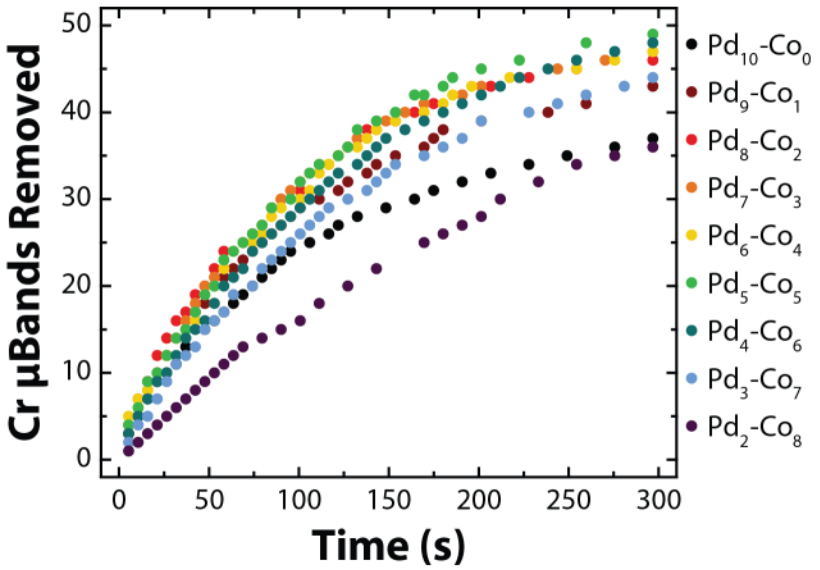

Figure 4.14. Plot of the number of Cr microbands removed vs. time for one row of BPEs.

4.5. Summary and Conclusions

In this chapter we have shown that bipolar electrochemistry provides a simple and highly parallel means for evaluating electrocatalyst candidates. To demonstrate this, we prepared 11 distinct compositions of each of three bimetallic electrocatalysts and tested their effectiveness for the ORR using arrays of wireless BPEs. The Pd-Co electrocatalyst proved to be the most effective. However, we showed that interpretation of these results requires caution due to catalyst instability and differences in the morphologies of the catalysts that depend on the relative amounts of the two metals present.

The methodology reported here provides a number of important advances over our earlier preliminary report of this general approach for electrocatalyst screening.[43] First, the number of electrodes per screening platform has been increased by more than an order of magnitude, which means more materials can be screened per experiment. It is also important to note that the device design can easily be changed to accommodate much larger arrays. Here, because we wanted to capture real-time, *in situ* movies of the electrodissolution of the Cr microbands, the size of the array was limited by the resolution and field-of-view of our microscope and camera. Second, we have implemented piezodispensing as a means of producing arrays of materials

of varying compositions. Third, we changed the identity of the reporter from Ag to Cr, because Cr requires a more positive potential to oxidize (near the thermodynamic potential of the ORR), meaning that materials requiring low overpotentials for the ORR can be reliably evaluated. The potential needed to oxidize Ag can actually be negative with respect to the ORR for certain promising catalyst candidates, meaning that the ORR and Ag oxidation could take place spontaneously (prior to the application of E_{tot}). The switch from Ag to Cr has several other benefits, such as simpler microfabrication and less risk of poisoning catalyst candidates with an easily reducible species such as Ag^{+}.

There are limitations to this technique in its current form. First, preparation of the platform requires fairly sophisticated microfabrication. Second, the electrode density (number of BPEs/cm^2) is limited by the method used to dispense the electrocatalysts. Third, it is important to control the location of the electrocatalysts. Fourth, the ITO substrate limits the maximum annealing temperature of the dispensed precursors. To varying degrees, there are probably solutions to all of these problems, and as the methodology evolves we will report on such advances. Finally, as for all such screening methods, variations in morphology of multimetallic catalyst candidates make it difficult to unambiguously identify the active phase.

Chapter 5: Evaluating Electrocatalysts for the Hydrogen Evolution Reaction based on Bi- and Trimetallic Combinations of Co, Fe, Ni, Mo, and W using Bipolar Electrode Arrays

5.1 Synopsis

In this chapter we report the development of a parallel electrocatalyst screening platform for the HER using BPEs. Electrocatalyst candidates are subjected to screening in a N_2-purged bipolar electrochemical cell where a pair of driving electrodes produce an electric field in the electrolyte solution. The HER occurring at the BPE cathodes is electrically coupled to the electrodissolution of an array of Cr microbands present at the BPE anodes. The readout of this device is simple, where the species that dissolve the most Cr microbands are identified as the most promising electrocatalyst candidates for further evaluation. We demonstrate the utility of this technique by comparing several bi- and trimetallic systems involving Co, Fe, Ni, Mo, and W, which are compared directly to pure Pt. Of all the compositions tested, Ni_8-Mo_2 is demonstrated to be the most active for the HER in a neutral electrolyte solution.

5.2 Introduction

In this chapter we report an electrocatalyst screening platform for the hydrogen evolution reaction (HER) that is based on bipolar electrochemistry.[49,104-106] Specifically, combinations of Co, Fe, Mo, Ni, and W have been defined on the cathodic poles of arrays consisting of 36-72 individual bipolar electrodes (BPEs). These metallic composites are then screened by exposing the electrode array to an electric field present in an electrolyte solution. Because the HER, occurring at the BPE cathodes, is electrically coupled to anodic dissolution of Cr microbands present at the BPE anodes (Scheme 5.1a), superior electrocatalysts will result in electrodissolution of a large number of Cr microbands (Scheme 5.1b).[45] The number of bands dissolved is determined by optical microscopy.

High-throughput electrocatalyst screening techniques are typically carried out using one of three general schemes (or some combination thereof): (1) direct measurement of the amperometric or voltammetric behavior of the catalyst at individually addressable electrodes,[75-77,107-110] (2) interrogation of an array of materials using a scanning probe (e.g., a laser beam,[79] an optical fiber,[80,111-115] a movable reference and counter electrode,[99,108] or an ultramicroelectrode tip[72,73,80,94,103,116-118]) in serial format, or (3) detection of an optical signal change

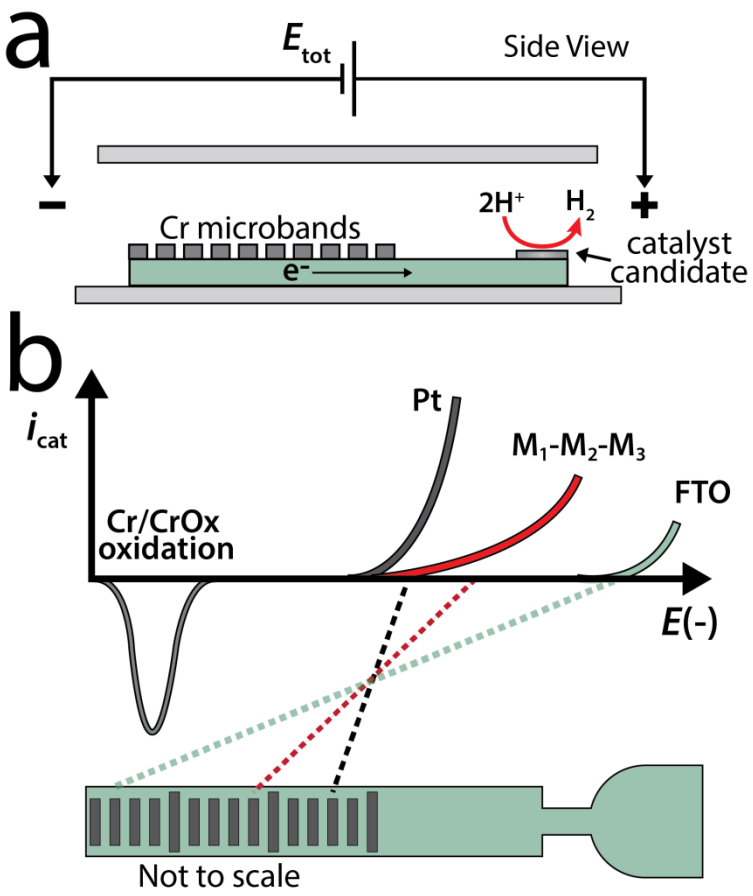

Scheme 5.1. (a) Side view of a BPE within the bipolar electrochemical cell where the oxidation of Cr microbands is coupled to the HER occurring at electrocatalyst candidates. (b) Schematic representation of the potentials needed to drive the HER at Pt, a trimetallic material, and naked FTO compared to the number of Cr microbands dissolved.

(e.g., changing local pH to turn on a fluorescent tracer,[74,119,120] changing reflectivity of a reporting thin film,[121,122] or monitoring gas bubbles[123]) arising from the products of an electrocatalyzed reaction. The direct measurement of current provides a great deal of information about the materials being evaluated, but may become unwieldy with dense electrode arrays. Scanned probe techniques are very powerful, information rich, and have been used in a variety of systems, but they are generally slow. Methods relying on an optical signal change offer much faster and simpler readout of the state of the array, but they may suffer from crosstalk between the materials being evaluated due to diffusion of the reporter dye. Additionally, they do not provide as much information as the foregoing two methods.

Bipolar electrochemistry offers a convenient platform for the parallel operation of large arrays of electrodes.[16,106,124] This is because each individual BPE is powered through an externally applied electric field. Accordingly, it is not necessary to connect each electrode to a power source or to directly measure current. However, because each BPE has both an anode and a cathode, an electrocatalytic reaction at one pole can be electrically linked to a reporting reaction at the other pole. For example, we previously showed that arrays of BPEs can be

used to screen electrocatalysts for the ORR using electrodissolution of thin metal films as the reporter reactions.[45,125] This provides a means for indirectly correlating the electrocatalytic current (or total charge) to the activity of the catalyst. Other groups have shown the electrogeneration of a fluorescent species or electrogenerated chemiluminescence (ECL) can be used to evaluate electrocatalysts using "closed" BPEs, where the BPEs serve as the only electrical path between physically separated half cells.[93,124] The fundamentals of bipolar electrochemistry and the operating principles of sensing and screening applications have been discussed in recent reviews.[49,106]

Pd and Pt are considered benchmark materials for the HER, because they have exchange current densities (j_0, A/cm^2) on the order of $\log(j_0)$ = -3 A/cm^2. However, they are scarce elements, making them impractical for large-scale applications.[126] In contrast, combinations of Co, Fe, Mo, Ni, and W might offer an economical alternative. For example, Co, Fe, Ni, Mo, and W, have been tested individually and as composite materials for the HER in acidic and alkaline solutions, and the exchange current densities vary between $\log(j_0)$= -6 and -4 A/cm^2.[127-133] However, a direct comparison of these materials, using consistent synthesis and measurement techniques, has not been carried out and there

are conflicting reports as to which compositions are the most active for the HER. One such study showed that for Ni-containing materials Ni-Mo was superior to Ni-Co and Ni-Fe.[127] Another study reported a lower overpotential for Co-Mo compared to Ni-Mo.[130] Others have shown that Ni-Mo out-performs Ni-Fe and Ni-W.[134] For the Ni-Mo system, some report a volcano-type relationship between activity and composition with the maximum activity occurring near Ni:Mo=1:1,[132] while others have found less systematic trends within narrow compositional variations.[131,133,134]

In this chapter, we synthesized and directly compared the following bimetallic compositions: Fe-Mo, Co-Mo, Ni-Mo, Fe-Ni, Co-Ni, Ni-W, Mo-W, along with several trimetallic compositions: Ni-Mo-Fe, Ni-Mo-Co, Ni-Mo-W. In all, we evaluated 231 different combinations of HER candidates. We found that most of these materials were unsuitable for use in acidic electrolytes compared to pure Pt. Under neutral conditions, however, we identified a compositional range of Ni-Mo materials (50-10% Mo) that produced promising results.

5.3 Experimental Section

Chemicals. Unless otherwise noted in the text, the following chemicals were used as received : $Fe(NO_3)_3 \cdot 9H_2O$ (Sigma Aldrich, 99.999%), $Co(NO_3)_2 \cdot 6H_2O$ (Alfa Aesar, 99.999%), $Ni(NO_3)_2 \cdot 6H_2O$ (Alfa Aesar, 99.9985%),

$(NH_4)_6Mo_7O_{24}•4H_2O$ (Sigma-Aldrich, 99.98%), $(NH_4)_{10}W_{12}O_{41}•5H_2O$ (Sigma-Aldrich, 99.99%), $(NH_4)_2PtCl_4$ (Alfa Aesar, 99.9%), KH_2PO_4 (Fisher Scientific), and K_2HPO_4 (Fisher Scientific). All aqueous solutions were prepared using Milli-Q water (18.2 Ω·cm). For piezodispensing, the concentrations of the metal precursor solutions were 0.15 M (metal equivalent) in ethylene glycol (Fisher Scientific).

Device Fabrication and Design. The BPEs were microfabricated and consisted of fluorine-doped tin oxide (FTO, 12-14 Ω/sq, TEC15, 2 mm-thick glass, Hartford Glass Co., Hartford City, IN) modified with Cr microbands, which were prepared using a slight modification of a previously described procedure.[45] Specifically, the etch step was longer (35 min) to account for the thickness of the FTO film vs. the previously used ITO. As shown in Scheme 5.2, each BPE was 4.00 mm long and had a 325 µm-wide pad defining the cathodic pole. The functional anode of each BPE consisted of 100 individual Cr microbands (5 nm thick, 10 µm long, and 10 µm edge-to-edge spacing). The lateral spacing of BPEs in the array was 750 µm center-to-center. Arrays designed for screening bimetallic compositions consisted of 36 electrodes (3 rows of 12). Thirty-three of these electrodes were used to test bimetallic composites,

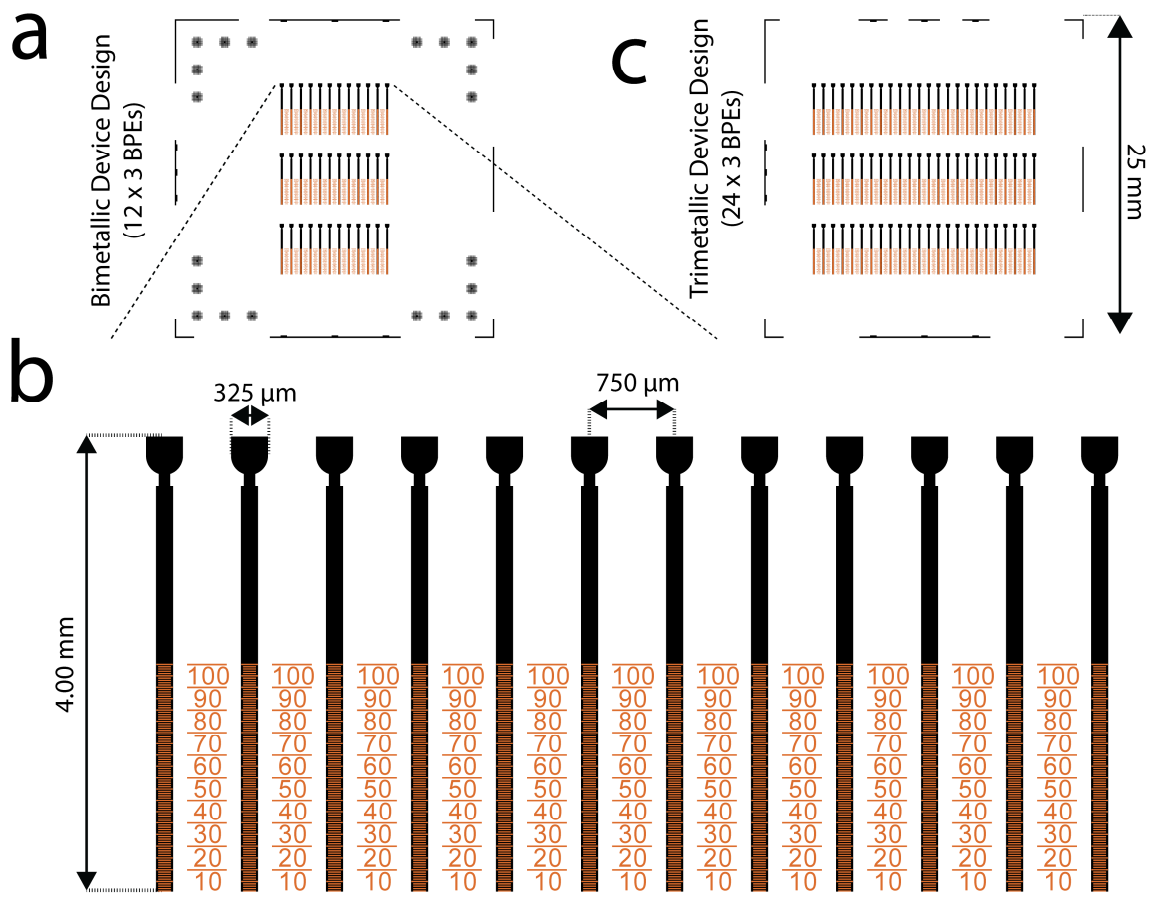

Scheme 5.2. (a) Device design used for testing bimetallic materials. Each device contains 36 electrodes (33 for the bimetallic materials and 3 for Pt). The black features result in FTO and the burnt orange features result in Cr. The functional anode of each electrode in the array is modified with 100 individual Cr microbands (5 nm-thick, 10 µm-long, 10 µm edge-to-edge spacing. (b) Expanded view of the first row of the device shown in (a). Each electrode is 4.00 mm-long and has a 325 µm-wide cathodic pad at the top. The electrodes are spaced by 750 µm center-to-center. (c) Device design for testing trimetallic compositions. Each device hosts an array of 72 individual electrodes (66 for the trimetallic composites, 6 for either Pt or FTO). The electrode dimensions and spacings are identical to those of the device shown in (a). Each frame is drawn to scale.

varying in composition by 10 atomic percent, in triplicate. The remaining 3 electrodes were modified with Pt to serve as internal standards for each row. Arrays designed for screening trimetallic composites contained 72 electrodes: 66 electrodes for evaluating trimetallic composites in increments of 10 atomic percent, with the remaining 6 electrodes either modified with Pt (3-6 electrodes) or left as naked FTO (3-0 electrodes) to serve as controls.

Piezodispensing Materials. Precursor salt solutions were dispensed using a previously described piezodispensing set-up.[112] The instrument has a printhead (PH046H-AT, Microfab) mounted onto an *x*,*y*,*z* robotic micropositioner (1560A, CH Instruments, Austin, TX). Each piezoelectric dispensing tip in the printhead is fed by a 2 mL reservoir connected to a pneumatic controller. The printhead contains 4 independent dispensing tips, so up to 4 components can be dispensed. Each electrode was modified with a total of 10 drops (~300 pL/drop) so that the total number of moles was maintained. By dispensing different relative numbers of drops of each precursor, the compositions can be changed by 10 atomic percent. The geometrical fidelity of the array spots was evaluated by scanning electron microscopy (SEM) using a Zeiss Supra 40 VP microscope.

Bipolar Electrochemical Cell Configuration. Screening experiments were carried out using a bipolar electrochemical cell consisting of a pair of GC driving electrodes (separated by 28.6 mm), a silicone gasket (0.5 mm-thick, Grace Biolabs, Bend, OR), which was laser-cut (Epilog Zing 16, Epilog Laser, Golden, CO) to a width of either 12 mm or 19 mm depending on the size of the BPE array, and a microscope slide, which served as the bottom of the BPE cell (Scheme 5.3). The BPE array, modified with electrocatalyst candidates, was then placed on top of this assembly with the electrodes facing down toward the microscope slide. The entire cell/electrode assembly was then placed into a home-built Teflon holder. Finally, the entire assembly was placed inside a transparent plastic box on a microscope stage.

The transparent box was purged with N_2 for at least 5 min before the cell was filled with electrolyte. Figure 5.1 shows the effectiveness of this purge box design for removing O_2, a possible source of background signal due to the ORR. A solution of 0.10 M PB (pH 6.9) was sparged with N_2 for at least 1 h before a small volume (~400 µL) was injected into the cell through a small opening in the purge box using a gas tight syringe (500 µL, Hamilton) fitted with a small length of polyetheretherketone (PEEK) tubing.

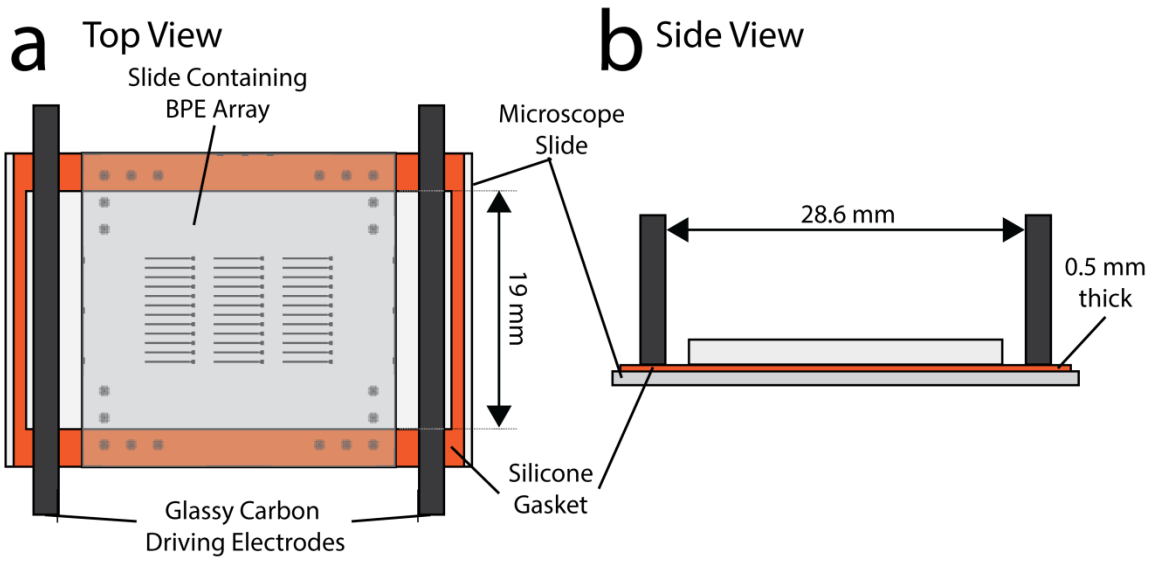

Scheme 5.3. Schematic of BPE cell. (a) Top view of the cell. The entire cell is mounted within a set of Teflon holders. The bottom-most piece is a microscope slide. On top of that is placed a laser-cut silicone gasket (0.50 mm-thick and with an opening of either 12 mm x 36 mm or 19 mm x 36 mm). The slide containing the BPE array is then placed on top of the gasket and sealed by pressure. Two GC driving electrodes are placed in the Teflon holder and are separated by 28.6 mm. (b) Side view of the cell shown in (a). These schematics are drawn to scale.

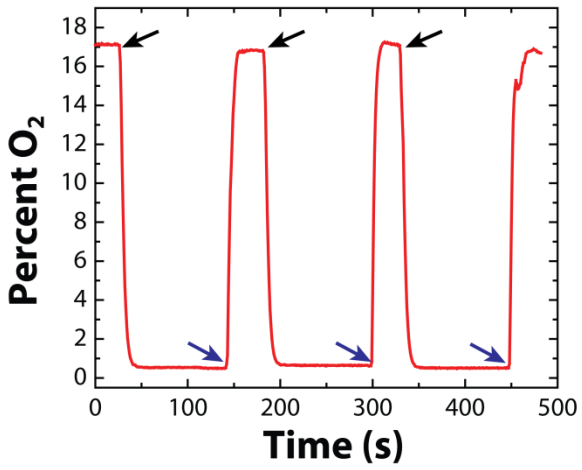

Figure 5.1. Monitoring concentration of O_2 in the purge box housing the cell in Scheme 5.3. The purge box was left open to atmosphere initially, then closed and purged with N_2 through a small tip inserted in the back at times indicated by the black arrows. At the times indicated by the blue arrows the box was opened to the atmosphere. A NEOFOXGT sensor (NFG0183, Ocean Optics, Dunedin, FL) was used to monitor the O_2 level. The percentage of O_2 measured inside the purge box after 60 s of purging was 0.55 ± 0.05% for the three pulses tested. This represents an approximately 31-fold decrease in O_2 concentration compared to the normal atmospheric level of 17.1%.

Electrocatalyst Screening Experiments. The driving voltage (E_{tot})[106] was applied to the two GC driving electrodes using a programmable DC power supply (PWS4721, Tektronix, Portland, OR) controlled by a custom LabView program that enables custom voltage/current step programs as well as monitoring/recording the total current (i_{tot}) and applied voltage (E_{tot}) in real time.

In addition to the incorporation of dedicated Pt-modified BPEs as internal standards on each device, the strength of the electric field was measured during preliminary experiments using a pair of pyrolyzed photoresist film (PPF) microband electrodes[135] microfabricated on the bottom microscope slide and an electrometer (2700, Keithley Instruments, Cleveland, OH). As an additional quality check, the total current passing through the cell (i_{tot}) was collected from the power supply using the custom LabView program. Figure 5.2 shows the measured values of i_{tot} for the devices tested in 0.10 M PB (pH = 6.9) when E_{tot} = 17.5 V was applied for a 10 s duration. The average value of i_{tot} was 5.69 ± 0.14 mA, or a 2.5% variation, for eight independent experiments.

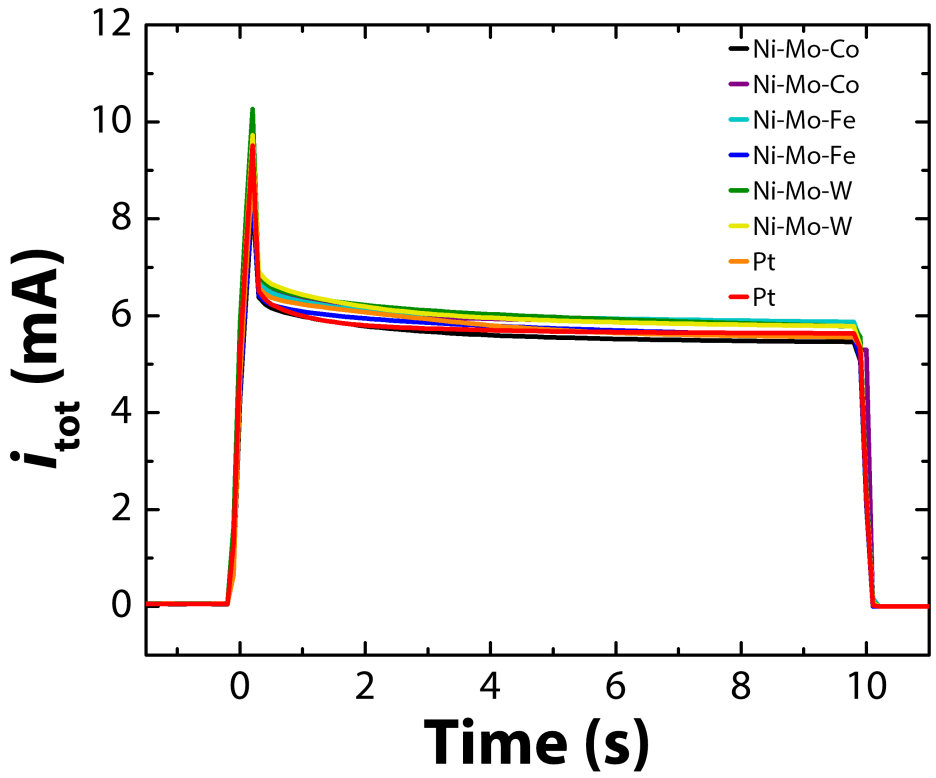

Figure 5.2. Measured values of total cell current (i_{tot}) for 8 devices consisting of the components listed in the figure legend. The devices were tested in 0.10 M PB (pH 6.9) with E_{tot} = 17.5 applied for 10 s. The average current was 5.69 ± 0.14 mA.

The experiments were monitored optically using a Nikon AZ100 microscope with a 0.5X PLAN APO objective. The camera was a Canon Rebel T3i digital single-lens reflex camera (DSLR) which was attached to the microscope using a Varimag II adapter (CNC Supply, Cape Coral, FL). Movies of the screening experiments were captured in the movie mode of the DSLR with a resolution of 1920 x 1080 pixels at a frame rate of 29.97 fps. This lower resolution but higher speed imaging was necessary given the short duration (10 s) of the screening experiment. This sacrifice in resolution means that the plots of bands removed vs. time are measured by monitoring the dissolution of the slightly wider bands at 5-band intervals instead of counting individual bands.

Scale-up and Three-Electrode Experiments. Following the BPE screening experiments, macro-scale films of certain compositions were synthesized and drop-cast onto electrodes for more detailed testing. Briefly, precursor solutions were pre-mixed to a total concentration of 15 mM in ethylene glycol, and 225 µL aliquots of this solution were drop-cast onto 1.5 cm x 1.5 cm FTO substrates. Under 5% H_2 / 95% Ar flow, the drop-cast films were dried at 120 °C for 1 h and then annealed at 350 °C for 2 h. The electrochemical properties of the films were evaluated in a three-electrode cell outfitted with a Pt wire counter electrode and a

Ag/AgCl (sat'd KCl, E = 0.197 V vs. NHE) reference electrode. The cell was filled with an electrolyte solution consisting of N_2-sparged 0.20 M PB (pH 6.9), and it was controlled by a potentiostat (601D, CH Instruments, Austin, TX). All potentials are converted from V vs. Ag/AgCl to the potential of a reversible hydrogen electrode (RHE, E = -0.408 V vs. NHE at pH = 6.9) to simplify comparison with the scientific literature.

5.4 Results and Discussion

Principles of the Screening Experiments. BPEs are well-suited for array-based sensing and screening experiments, because an entire array can be powered by a single power source and because a direct electrical connection to each BPE is not required. The basic principles and fundamentals of bipolar electrochemistry have been discussed in detail in recent reviews,[49,106] but the specific operating principles of a BPE screening experiment are described next.

As shown in Scheme 5.1a, a potential bias (E_{tot}) is applied between a pair of driving electrodes to produce an electric field in the solution covering the BPE array. The fraction of E_{tot} dropped over each electrode is referred to as ΔE_{elec}, and the latter is estimated by multiplying the length of the BPE by the strength of the electric field.

ΔE_{elec} is the driving force for the faradaic reactions occurring at the two poles of each BPE. When E_{tot} is first applied, all of the BPEs in the array experience the same magnitude of ΔE_{elec}. However, as the Cr microbands begin to dissolve, the effective length of each BPE in the array decreases, thereby decreasing ΔE_{elec}. Because both the oxidation of the Cr microbands and the HER must be driven simultaneously, when ΔE_{elec} becomes too small the two reactions effectively stop. Better electrocatalysts need lower overpotentials to drive the reaction and thus oxidize more Cr microbands.

Short Duration BPE Screening Experiments. For the screening experiments described in Chapter 4, the experiment was allowed to progress for up to 5 min so that the rate of Cr dissolution effectively stopped. This made it possible to determine the relative onset potentials for the ORR by simply counting the number of Cr microbands that dissolved. However, for the screening experiments reported here, we have adopted a slightly different approach.

Instead of allowing the reactions to progress until the rates become insignificant, we apply E_{tot} for a much shorter time (5 or 10 s, depending on the electrolyte). The motivation behind this change in experimental protocol is to remove, to the maximum extent possible, contributions of

background processes, such as the ORR, that could affect the apparent end point of the experiment. In many systems the HER occurs at a much faster rate than the ORR, especially in the N_2-purged electrolyte solutions used in the experiments reported here.

The important distinction between the short-duration screening experiments used here and the longer durations used previously is that instead of determining a relative onset potential for the electrocatalytic reaction of interest, the screening experiment is ended while both the anode and cathode reactions are active. This is analogous to determining the overpotential at a particular current density rather than determining the onset potential for the reaction. Therefore, it is very important to select an appropriate duration for the application of E_{tot}.

In a preliminary experiment, using Ni-Mo as a bimetallic catalyst in 0.10 M PB (pH 6.9), E_{tot} was applied for 30 s and the rate of Cr microband dissolution was measured as a function of time. Figure 5.3a is an optical micrograph of one row of a BPE array consisting of 36 individual electrodes (3 rows of 12 electrodes each) configured such that a bimetallic system of 10% compositional variation can be evaluated in triplicate (33 total electrodes) with the 3 remaining electrodes modified with piezodispensed Pt serving as a control.

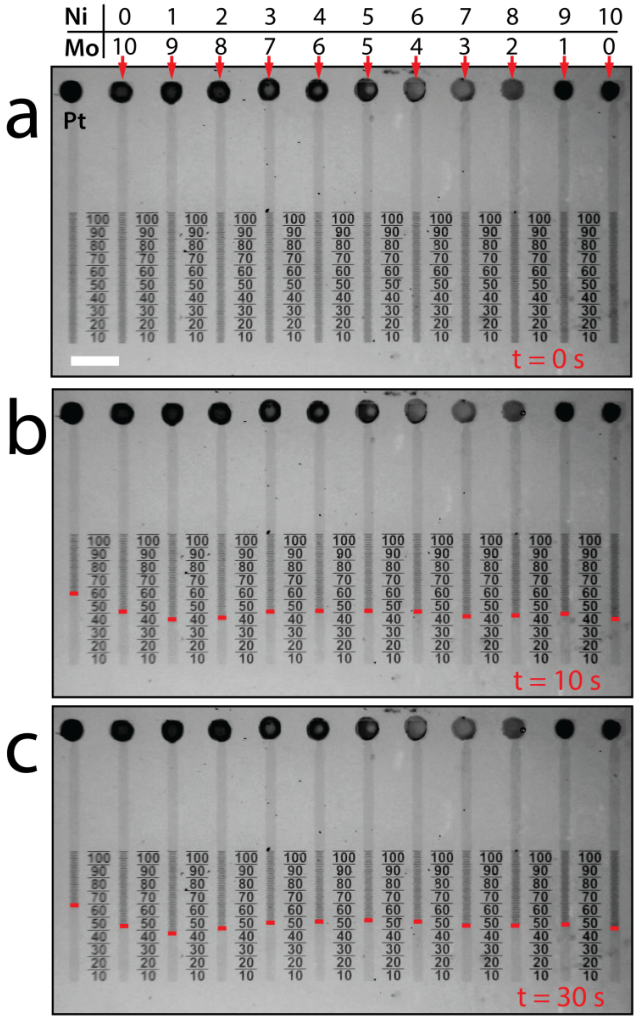

Figure 5.3. A BPE electrochemical cell for screening Ni-Mo bimetallic catalyst candidates for the HER. (a) Optical micrograph of the device prior to the application of E_{tot}. The cathodic pole of the left-most electrode was modified with 10 drops of Pt. The remaining electrodes were modified with the indicated number of drops of precursor solution for Mo and Ni such that the total number of moles of metal (Ni + Mo) deposited on each electrode was the same, but the atomic percentages varied by 10%. The silicone gasket used to define the walls of the fluidic space was 12 mm-wide. E_{tot} = 17.5 V was applied for 30 s. The remaining frames show the progress of the screening experiment at (b) 10 s and (c) 30 s.

Figures 5.5b and 5.5c show the progress of the screening experiment during the application of E_{tot} = 17.5 V for 10 s and 30 s, respectively. These data demonstrate that the majority of dissolution occurs within the first 10 s, with just 1-5 bands dissolving during the remaining 20 s. Therefore, the duration of all experiments carried out in PB electrolyte was limited to 10 s.

Figure 5.4a is a plot of the number of bands removed as a function of time for the electrodes shown in Figure 5.3. These data indicate that the rate of dissolution of the Cr microbands from the anodic pole of each electrode is related to the material present at the cathode. The electrode modified with Pt (black) dissolves the most bands during the application of E_{tot}. The Ni-Mo composites that dissolved the most bands within the first 10 s consisted of 40-50% Ni. Figure 5.4b is a plot of the electric field strength, measured between two PPF microbands fabricated on the bottom glass piece of the bipolar electrochemical cell, and i_{tot}, the total current flowing in the cell, as a function of time. A comparison of these data indicates that there is a time-dependent decay both in i_{tot} and the strength of the electric field across the cell. The important point is that within 5 s, both the current and the field are stabilized, and hence times >5 s are desirable for making reproducible measurements.

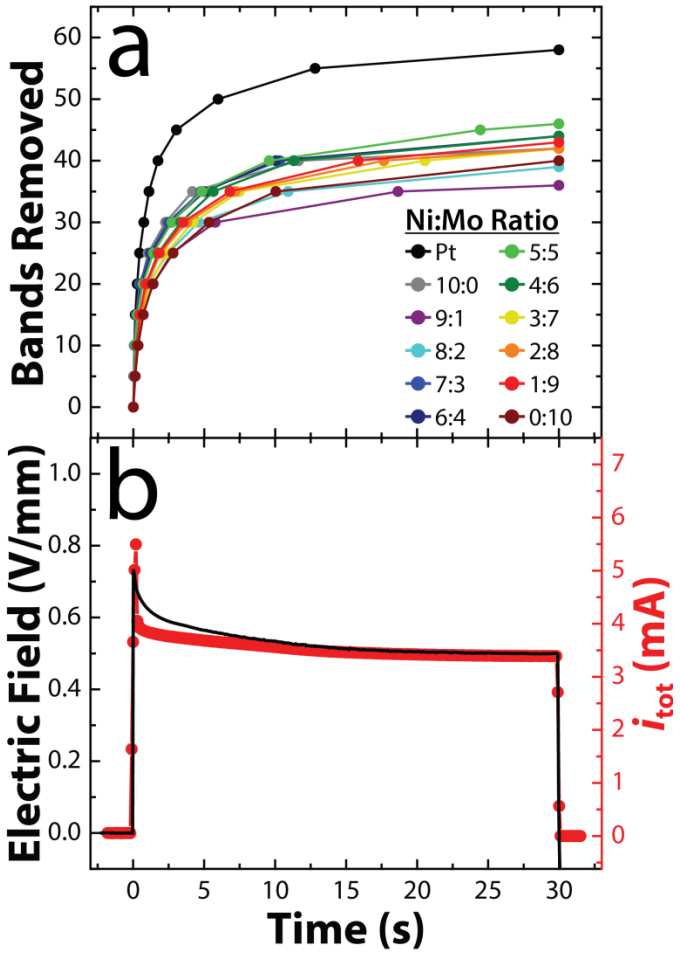

Figure 5.4. (a) Plot of the number of Cr bands removed vs. time for the same device shown in Figure 5.3. (b) Electric field strength (black, left axis) and total current (i_{tot}, red, right axis) flowing through the electrochemical cell as a function of time during the application of E_{tot} = 17.5 V. The field strength was measured using a pair of PPF microbands (150 µm-wide, separated by 20 mm) fabricated onto the bottom microscope slide of the bipolar electrochemical cell. Notice the time-dependent decay of i_{tot} and the electric field strength during the application of E_{tot}.

Demonstrating Reproducibility with Pt. To determine the reproducibility of this screening approach, a control experiment was carried out by evaluating the HER on 36 nominally identical BPEs. Figure 5.5a is an optical micrograph of one row of the array, comprising 12 BPEs, prior to application of E_{tot}. Figures 5.7b and 5.7c show the device during the applied potential pulse at t = 5 and 10 s. The red bars, indicate the position of lowest intact Cr microband. At the conclusion of the 10 s duration of the experiment, an average of 45.1 ± 1.8 Cr microbands dissolved. In an independent, replicate experiment, the average number of Cr microbands dissolved was 43.2 ± 1.8. Altogether, a total of 99 Pt spots were tested in the PB electrolyte, and 46 ± 4 microbands were found to dissolve. These results demonstrate that the level of reproducibility is around 10% using this short potential pulse method. This value is comparable to the variability reported previously for the long potential pulse method applied to ORR electrocatalyst candidates.[106]

Figure 5.6a provides additional information regarding reproducibility. It is a plot of the number of Cr microbands removed as a function of time throughout the 10 s duration of the experiment. The data for each electrode were fitted using a single exponential function to compare the rates of dissolution. At short times (50 ms to 500 ms) the rates show

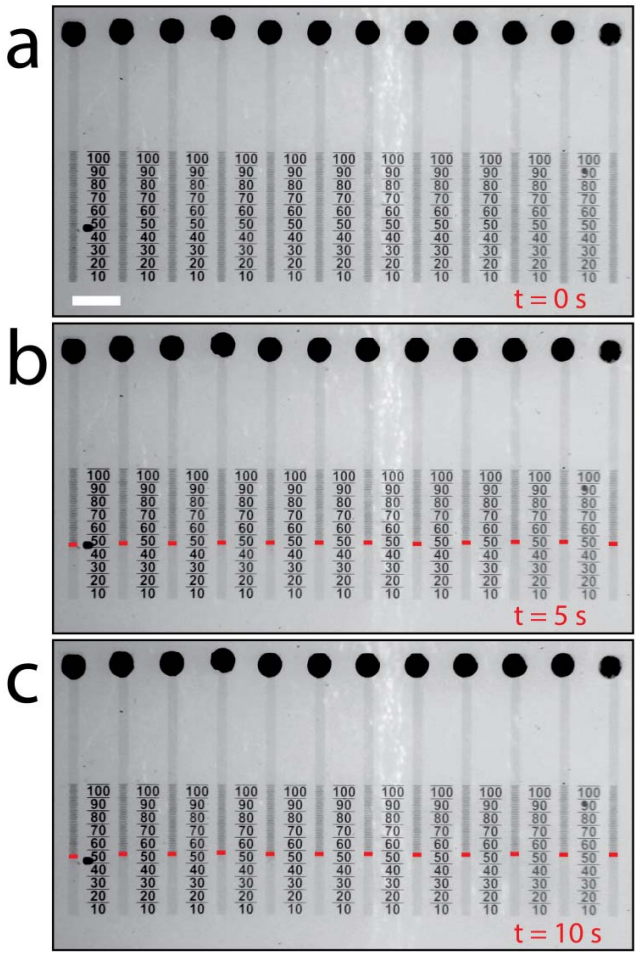

Figure 5.5. A BPE electrochemical cell for screening Pt candidates for the HER. (a) Optical micrograph of the device prior to the application of E_{tot}. The configuration of the BPE array is the same as in Figure 5.3, except here every BPE on this device was modified with Pt. The silicone gasket used to define the walls of the fluidic space was 19 mm-wide. E_{tot} = 17.5 V was applied for 10 s. The remaining frames show the progress of the screening experiment at (b) 5 s and (c) the 10 s.

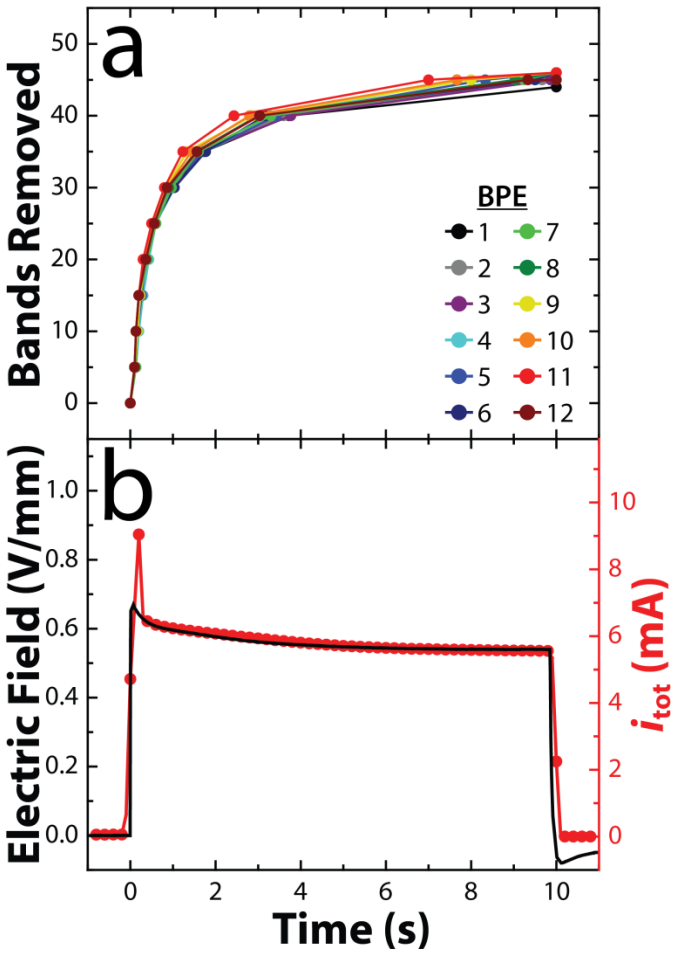

Figure 5.6. (a) Plot of the number of Cr bands removed vs. time for the same device shown in Figure 5.5. (b) Electric field strength (black, left axis) and total current (i_{tot}, red, right axis) flowing through the electrochemical cell as a function of time during the application of E_{tot} = 17.5 V. The field strength was measured using a pair of PPF microbands (150 µm-wide, separated by 20 mm) fabricated onto the bottom microscope slide of the bipolar electrochemical cell. Notice the time-dependent decay of i_{tot} and the electric field strength during the application of E_{tot}.

decreasing relative standard deviations (RSDs) from 7-12% across the 12 electrodes. At longer times (t >500 ms), the RSDs of the rates of dissolution are less than 5%. Figure 5.6b shows the electric field strength and i_{tot} and during the E_{tot} pulse.

We carried out screening experiments similar to those just described, but in 50 mM H_2SO_4 for an array of BPEs modified with Pt. Under these conditions the average for all piezodispensed Pt spots evaluated, using a 5 s pulse of E_{tot} = 15.0 V in the 50 mM H_2SO_4 electrolyte (42 total), was 48 ± 5 Cr microbands dissolved. An example of a screening experiment for Pt is shown in Figure 5.7.

Screening Bi- and Trimetallic Non-Noble Metal Electrocatalyst Candidates. After demonstrating that the selected experimental design and operating parameters result in reproducible data for Pt alone, we returned to evaluating bi- and trimetallic compositions for the HER using 0.10 M PB (pH 6.9) electrolyte and Ni and Mo as the common elemental components. Each bimetallic composition was evaluated in triplicate and Pt served as an internal standard for each row to provide reliable intra- and inter-device comparisons.

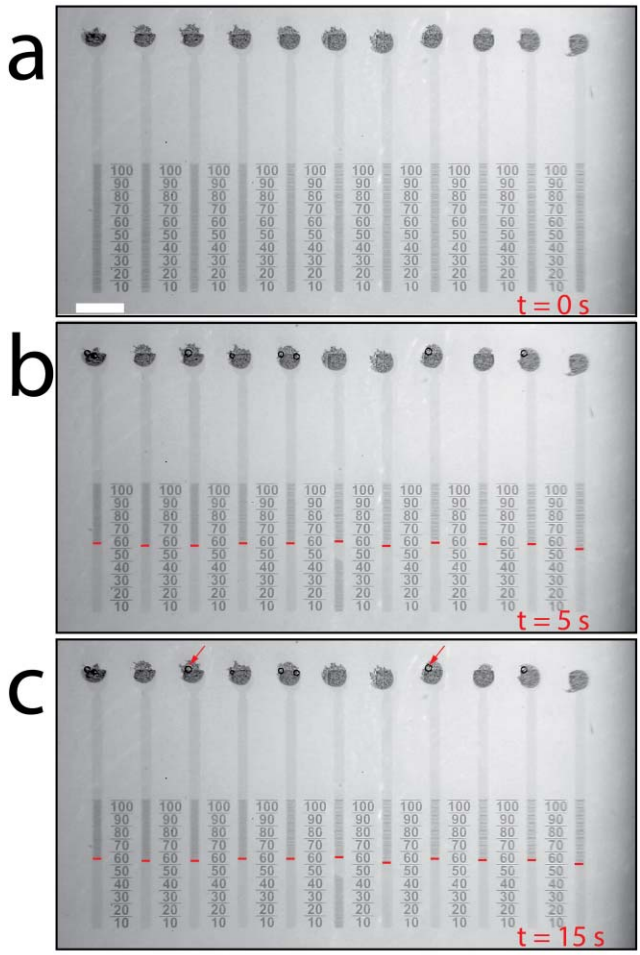

Figure 5.7. (a) Optical micrograph of an array of 11 BPEs having Pt at their cathodic poles. Each BPE is 4 mm long and each has been modified with an array of 100 individual Cr microbands. The BPE device was placed in the bipolar electrochemical cell situated in an optically transparent plastic box. The box was purged with N_2 for >5 min. The cell was then filled with a N_2-purged, 50 mM H_2SO_4 solution. E_{tot} (15.0 V) was applied for 15 s using a programmable DC power supply. The remaining frames show the progress of the experiment at (b) 5 s and (c) 15 s. The sixth electrode from the left side of the array had damage in the FTO at the anodic pole, meaning it was not connected for the whole length of the electrode. Note the presence of bubbles formed at the cathodic poles of the BPEs (red arrows).

The BPE arrays used for testing trimetallic materials consisted of 3 rows of 24 individual electrodes (72 total electrodes). Sixty-six of the electrodes were modified with a mono-, bi-, or trimetallic mixture of Ni-Mo-M, where M = Co, Fe, or W, and the remaining electrodes were either modified with Pt or left as naked FTO to serve as controls.

Figures 5.8-5.10 show matrix plots for 3 different trimetallic combinations: Ni-Mo-Co, Ni-Mo-Fe, and Ni-Mo-W. These plots show the number of Cr microbands dissolved for each species and are color coded according to the scale shown on the right: dark green tones represent the best catalysts. The arrays vary in atomic composition by 10% for Ni on the vertical axis, by 10% for Mo on the diagonal (indicated by thin black dashed lines), and by 10% for the third metal on the horizontal axis. A total of 10 drops was used to prepare each trimetallic composite. For example, Figure 5.8 shows the results for the Ni-Mo-Co trimetallic. To identify the performance of Ni_6-Mo_2-Co_2, start with the row designating 6 drops of Ni, then find the column indicating 2 drops of Co, and then follow the diagonal black dashed line to the box indicating 2 drops of Mo. The results for this material are found in the box highlighted by a red border. Several reports indicate that trimetallic composites of Ni-Mo-Co may out-perform Ni-Mo or the monometallics.[136,137] Additionally, Co-Mo has been reported to require a lower

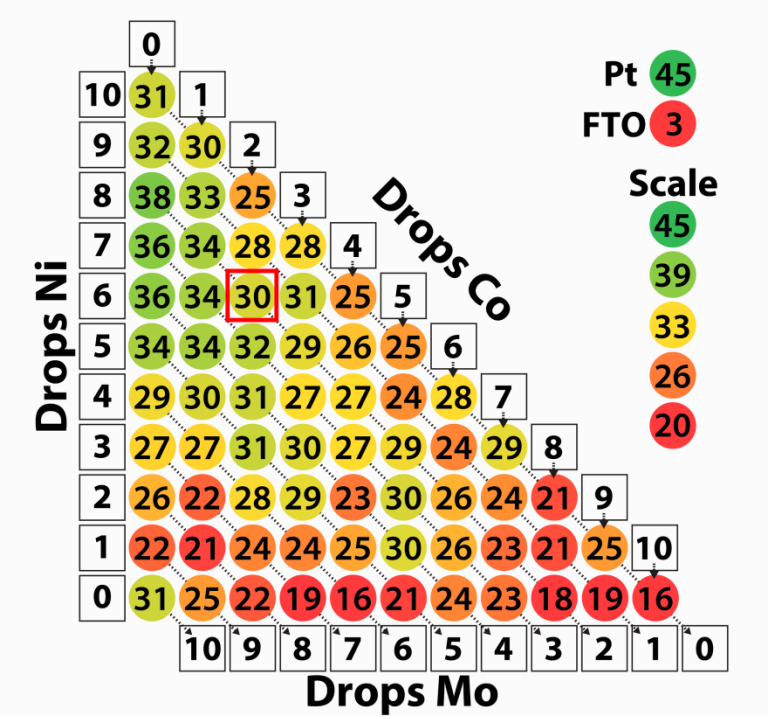

Figure 5.8. Matrix plot of number of bands dissolved based for Ni-Mo-Co. The vertical axis represents the amount of Ni, the diagonal axis (bottom, indicated by black dashed arrows) represents the amount of Mo, and the horizontal axis represents the amount of Co. The numbers in the chart indicate the average number of bands dissolved for two separate devices. The performance of the Ni-Mo spots is shown in the left-most column. The average performance of the Pt and naked FTO support is shown on the right side of the plot. The color scale is indicated on the right side. The red box in (a) indicates Ni_6-Mo_2-Co_2 as described in the main text.

overpotential for the HER than Ni-Mo.[130] In our case, however, the bimetallic Ni-Mo catalysts were the most active species with generally decreasing performance as the percentage of Ni was lowered. It is also important to point out that the differences in the number of Cr bands dissolved is low within certain compositional windows, but these results are still useful for identifying trends in the performance of the materials.

Figure 5.9 shows results for the Ni-Mo-Fe trimetallic system. In basic electrolyte solutions, Ni-Mo-Fe has been reported to have higher activities than the other trimetallic compositions tested here.[137] As is evident from this matrix, the bimetallic Ni-Mo system produced the most active species, with low (less than 30%) amounts of Fe producing similar numbers of Cr bands removed, suggesting that additional, more detailed studies of these materials might be warranted.

Figure 5.10 shows the screening results for the Ni-Mo-W trimetallic system. W was chosen as the third component based on its slightly higher exchange current density than Mo: $\log(j_0) \approx -6$ A/cm^2 vs. -7 A/cm^2.[128] Interestingly, high concentrations of W appear to produce poorly performing materials, and composites with small amounts of W (less than 30%) showed similar performance to the bimetallic Ni-Mo system.

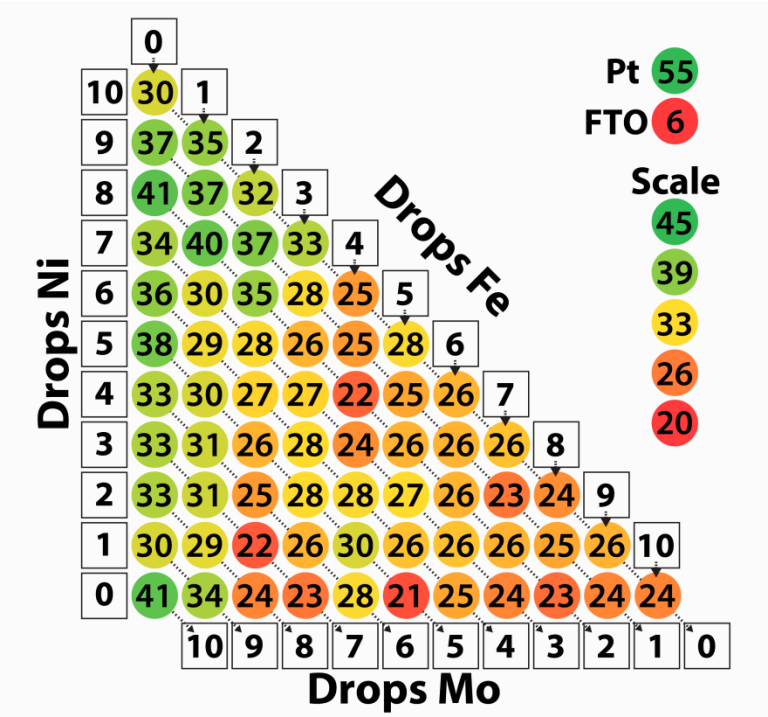

Figure 5.9. Matrix plot of number of bands dissolved based for Ni-Mo-Fe. The vertical axis represents the amount of Ni, the diagonal axis (bottom, indicated by black dashed arrows) represents the amount of Mo, and the horizontal axis represents the amount of Fe. The numbers in the chart indicate the average number of bands dissolved for two separate devices. The performance of the Ni-Mo spots is shown in the left-most column. The average performance of the Pt and naked FTO support is shown on the right side of the plot. The color scale is indicated on the right side.

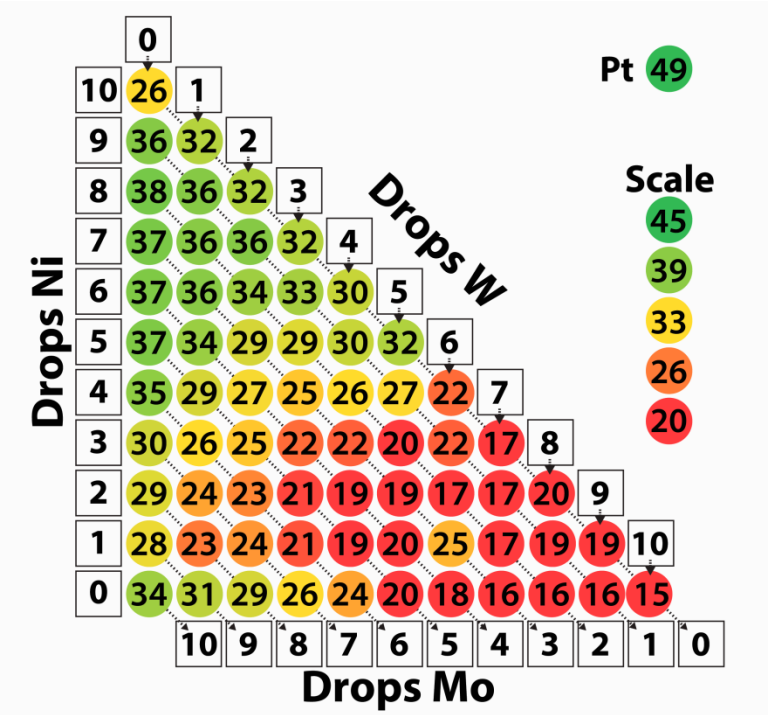

Figure 5.10. Matrix plot of number of bands dissolved based for Ni-Mo-W. The vertical axis represents the amount of Ni, the diagonal axis (bottom, indicated by black dashed arrows) represents the amount of Mo, and the horizontal axis represents the amount of W The numbers in the chart indicate the average number of bands dissolved for two separate devices. The performance of the Ni-Mo spots is shown in the left-most column. The average performance of the Pt is shown on the right side of the plot. The color scale is indicated on the right side.

In this study, the bimetallic Ni-Mo catalysts (left-most columns in Figures 5.8-5.10) consistently performed better than the three trimetallic combinations. The dark gray bars in Figure 5.11 summarize the relative activity of the Ni-Mo materials (tested in 0.10 M PB, pH 6.9) for at least 8 independently prepared electrodes for each composition. The most active species was Ni_8-Mo_2, but all of the compositions comprised of between 50 and 90% Ni exhibited better average activity than the pure component metals. This result is consistent with a recent study of Ni-Mo nanopowders.[138]

The light gray bars in Figure 5.11 correspond to the same Ni-Mo combinations described in the previous paragraph, except now evaluated for activity using 50 mM H_2SO_4 electrolyte. There were differences in performance across the compositional range, but the materials performed considerably worse than Pt and all compositions performed more poorly than in PB buffer. Furthermore, even in the short amount of time necessary to run the screening experiment (~3-5 min), the materials partially dissolved from the cathodic pole in the acidic electrolyte. This poor stability has been predicted for Ni and Mo based materials via density functional theory (DFT) calculations.[139] The results for bimetallic Fe-Mo and Co-Mo combinations in the acidic electrolyte are provided in the Figure 5.12. Both

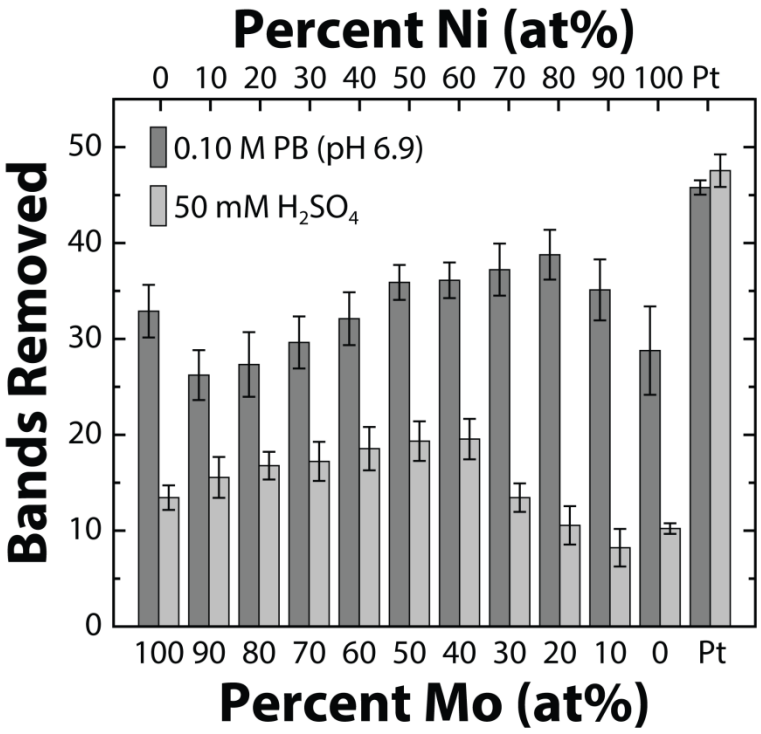

Figure 5.11. Bar graph showing the number of Cr microbands dissolved for the bimetallic Ni-Mo system in 0.10 M PB (pH 6.9) (dark gray) and 50 mM H_2SO_4 (light gray). The bars on the far right indicate the mean performance of Pt over all devices in each electrolyte. The error bars indicate the 95% confidence interval for these data.

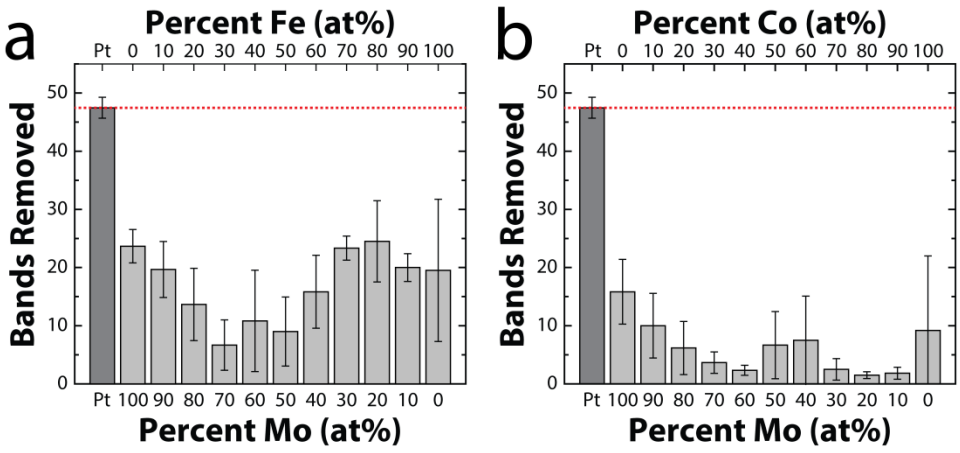

Figure 5.12. Performance of bimetallic systems in 50 mM H_2SO_4 for (a) Fe-Mo and (b) Co-Mo catalyst candidates. Each composition was evaluated on at least 6 individual BPEs. The dark gray bar at the far left indicates the mean performance of Pt, which is also indicated by the red dashed line. The error bars indicate the 95% confidence interval for each material.

systems suffered from inconsistent results and showed no enhancement over the monometallic materials.

One disadvantage of synthesizing metals by piezoelectric dispensing of metal salt solutions followed by reduction at elevated temperatures is that the surface structure and morphology are not controlled. Therefore, differences in activity for various piezoelectric dispensed compositions may be partially due to differences in the accessible surface area of the catalyst.[140] To address this concern, we viewed the Ni-Mo array spots, along with the Pt spots and naked FTO, by SEM (Figures 5.13 and 5.14). The SEM micrographs reveal a somewhat porous nanostructure for pure Ni, Mo, and Pt. However, the bimetallic Ni-Mo compositions (10 – 90% Mo) appear to be mostly dense without a remarkable amount of surface structure. Therefore compositional effects likely play a larger role in the catalytic activity of the Ni-Mo system than surface area.

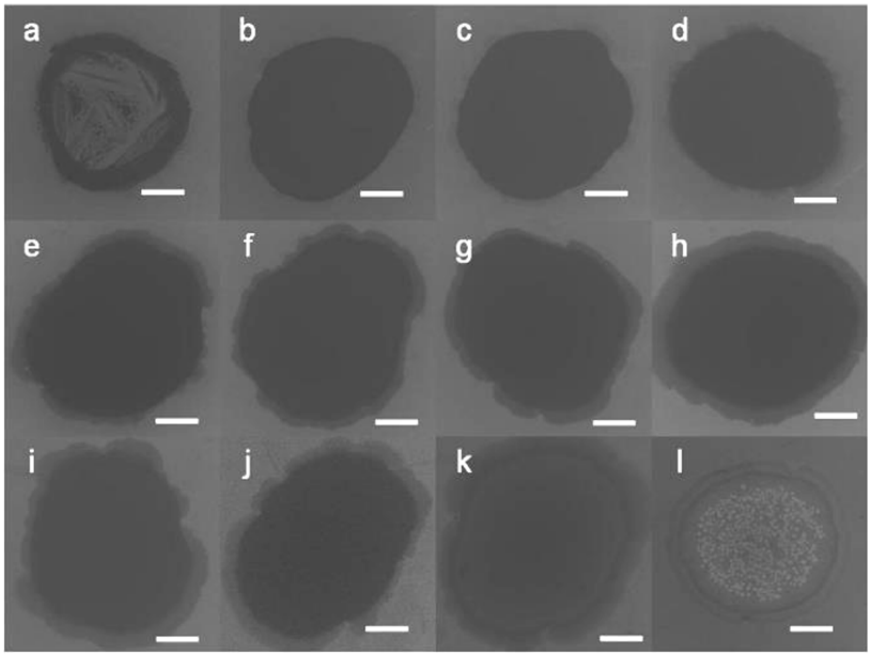

Figure 5.13. Low magnification SEM images of Ni-Mo catalyst candidates. The Ni:Mo atomic ratios are: (a) 0:10, (b) 1:9, (c) 2:8, (d) 3:7, (e) 4:6, (f) 5:5, (g) 6:4, (h) 7:3, (i) 8:2, (j) 9:1, and (k) 10:0. Frame (l) shows the spot for pure Pt. The white scale bars represent 100 µm. After dispensing the precursor solution, the spots were reduced in 5% H_2 / 95% Ar at 350 °C for 1.5 h.

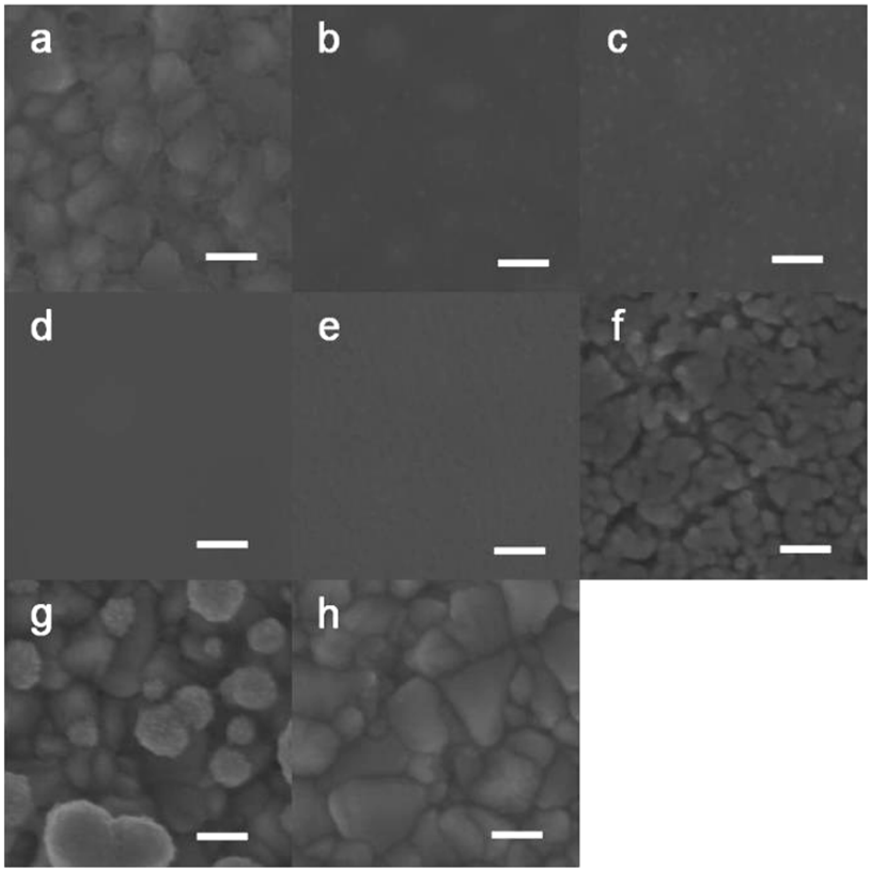

Figure 5.14. High magnification SEM images obtained in the center of several of the spots shown in Figure 5.15. The Ni-Mo atomic ratios are: (a) 0:10, (b) 2:8, (c) 4:6, (d) 6:4, (e) 8:2, and (f) 10:0. Frame (g) shows pure Pt and (h) shows naked FTO. The white scale bars represent 100 nm.

Three-Electrode Evaluation of Ni-Mo. Because the Ni-Mo bimetallics containing 50-80% Ni reproducibly yielded the most active catalysts, we prepared macro-scale films of several Ni-Mo compositions (0, 20, 80, and 100% Mo) by drop-casting the appropriate metal salts and then heating in H_2 to verify the results obtained from the screening experiments. A three-electrode electrochemical cell and the technique of linear scan voltammetry (LSV) were used for these measurements. The results are shown in Figure 5.15.

The LSV trace for Pt shows a cathodic current onset near the thermodynamic potential for the HER (0 V vs. RHE). The Ni_8-Mo_2 bimetallic exhibited a similar cathodic current onset potential, but a slower increase in current density compared to Pt. At a current density of 10 mA/cm^2, Pt had the lowest HER overpotential (237 mV) followed by Ni_8-Mo_2 (498 mV). Ni_2-Mo_8 and Mo yielded significantly higher HER overpotentials and did not reach 10 mA/cm^2 at potentials more positive than -0.6 V. The important point is that the LSV results, obtained using a traditional electrochemical set-up and macro-scale electrodes, are consistent with the results of BPE screening experiments (Figure 5.11), verifying that the BPE screening platform can be used to select promising electrocatalyst candidates for the HER.

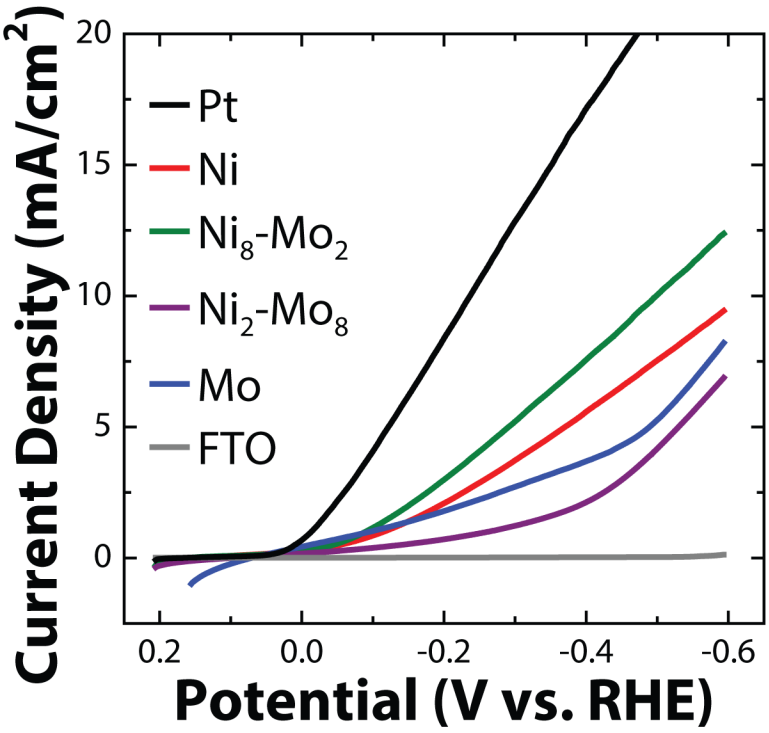

Figure 5.15. LSV scans for macro-scale metal films of materials indicated in the legend. The electrolyte was 0.20 M PB (pH 6.9), which was continuously sparged with N_2 gas. The initial scan direction was negative. The scan rate was 25 mV/s and no *iR* compensation was used.

5.5 Summary and Conclusions

We have demonstrated that bipolar electrochemistry can be used to evaluate electrocatalyst candidates for the HER. Specifically, a series of bi- and trimetallic candidates were prepared using a piezodispensing technique followed by chemical reduction, and the resulting materials were tested in both neutral and acidic electrolytes. Better stability was observed in neutral electrolytes and the most active material identified was a Ni-Mo bimetallic consisting of 20% Mo. The fact that the catalytic activity of these materials is consistent with that found using LSV, as well as results reported by other groups who used different screening methods, is a reassuring sign that BPE screening provides accurate results.

The key point is that a large number of catalyst compositions can be screened in just a few minutes using simple instrumentation, and that the BPE screening method leaves a permanent record of the results. Moreover, by filming videos of the dissolution of the Cr bands, it is possible to obtain kinetic data about the catalyst. Indeed, we are presently trying to understand how such videos can accurately be converted into quantitative kinetic information. This turns out to be a complicated problem, but if it can be resolved this approach to screening will become even more useful.

Chapter 6: Two-Dimensional Bipolar Electrochemistry

6.1 Synopsis

This chapter introduces the concept of two-dimensional bipolar electrochemistry and discusses its principle of operation.[41] The interesting new result is that electrochemical reactions can be localized at particular locations on the perimeter of a two-dimensional bipolar electrode (2D-BPE), configured at the intersection of two orthogonal microfluidic channels, by controlling the electric field within the contacting electrolyte solution. Experimentally determined maps of the electric field in the vicinity of the 2D-BPEs are in semi-quantitative agreement with finite element simulations.

6.2 Introduction

In this chapter we introduce the concept of two-dimensional bipolar electrochemistry and discuss its principles of operation. The interesting new result is that electrochemical reactions can be localized at particular locations on the perimeter of a 2D-BPE by controlling the electric field within the contacting electrolyte solution. This construct is conceptually distinct from the types of one-dimensional BPEs that we[16,35-37] and others[50,141-144] have reported previously, and it opens up the possibility of

creating an electrochemical array comprised of a single electrode. Such systems might find applications in chemical sensing,[35,36,145] or materials synthesis and characterization.[143]

One-Dimensional BPE. First consider the case of a simple, one-dimensional BPE (Scheme 1.2).[37] When a voltage (E_{tot}) is applied between two driving electrodes present in reservoirs at either end of a single microfluidic channel filled with an electrolyte solution, an electric field is induced within the channel. If an electronically conductive wire of sufficient length is present within the channel, and if E_{tot} is sufficiently high, then faradaic electrochemical reactions will take place at either end of the wire even though there is no direct electrical connection to it.[37] In this case, the wire is called a BPE, and the fraction of E_{tot} that is dropped in solution over the BPE is defined as ΔE_{elec}.

While the potential difference between the two ends of a BPE and the contacting solution can be conveniently controlled, measurement of current induced in the BPE is more problematic. Some time ago, the Crooks group resolved this difficulty by coupling the electrochemical reaction at the cathodic pole of the BPE to a light emitting reaction at the anodic pole.

Specifically, ECL, produced by the simultaneous oxidation of $Ru(bpy)_3^{2+}$ and tri-*n*-propylamine (TPrA), reported the rate of the cathodic process.[64] This is an effective strategy because the rates of the faradaic reactions at the two poles of the BPE must be the same.[37] We employ the same approach here.

Two-Dimensional BPE. Now consider the 2D-BPE configuration shown in Scheme 6.1. It consists of a planar electrode situated at the intersection of two orthogonal microfluidic channels. When driving voltages (E_{tot1} and E_{tot2}) are independently applied across the two channels, the resulting field is the vector sum of the individual fields in the microfluidic channels. Accordingly, the magnitude of the interfacial potential difference between the solution and the BPE, which is the driving force for electrochemical reactions, is a function of location.[37] This provides a means to focus electrochemical reactions at specific points on a 2D-BPE.

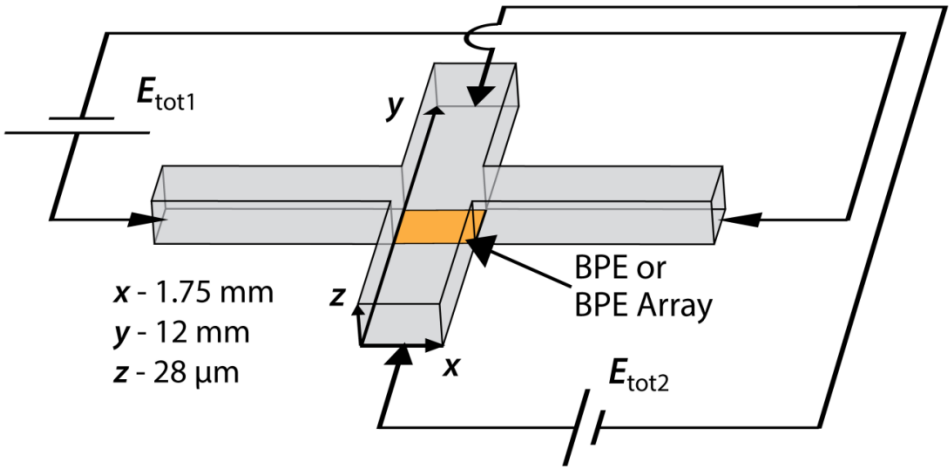

Scheme 6.1. Schematic depiction of the two orthogonal microchannels used to drive a 2D-BPE or to power an array of BPEs. The scheme is not drawn to scale.

6.3 Experimental Section

Chemicals, Materials, and Instrumentation. Gold-coated slides (5 nm Cr adhesion layer, 100 nm Au, EMF Corp., Ithaca, NY) were used to fabricate the electrodes using previously reported photolithographic techniques.[37] PDMS (Sylgard 184, Dow Corning, Midland, MI) was used to construct the channels. $Ru(bpy)_3Cl_2 \cdot 6H_2O$ was purchased from Strem Chemicals, Inc. The tri-*n*-propylamine was purchased from Sigma-Aldrich. The potentials of the driving electrodes were controlled using two independent power supplies (Electrometer 6517B, Keithley Instruments, Cleveland, OH and Power Supply LLS-9120, TDK-Lambda, San Diego, CA). An optical microscope (Nikon AZ1000, Nikon Co., Tokyo, Japan) with a CCD detector (Cascade, Photometrics Ltd., Tucson, AZ) was used to collect micrographs.

Finite Element Simulations. Simulations were carried out using the COMSOL Multiphysics software package (version 3.5a) and the Conductive Media DC module. The dimensions of the channels were constructed to reflect the actual dimensions of the microfluidic device, and the applied potentials were simulated by inputting the potential at the ends of the channels. To account for the potential drop due to faradaic reactions at the driving electrodes, 3 V was subtracted from the total applied potential.[37] To account

for the floating nature of the two power supplies, the potential at the center of the model (x = 0, y = 0) was fixed at 0 V. Because we have previously demonstrated that under similar conditions the amount of current passing through the BPEs is less than 1% of the total current,[37] we assume that the BPEs do not have a significant impact on the shape of the electric field.

6.4 Results and Discussion

A Single 2D-BPE. Figure 6.1a is an optical micrograph of the crossing point of the two channels illustrated in Scheme 6.1; the light area is the Au BPE and the PDMS channels are delineated by dashed white lines in the corners of the image. For the experiments described here, the channels were filled with aqueous, air-saturated 5.0 mM $Ru(bpy)_3^{2+}$, 25 mM TPrA, and 0.10 M phosphate buffer (pH 6.9). Under these conditions, ECL is emitted at the anodic pole when oxygen and water reduction occur at the cathodic pole. We have previously shown that ΔE_{elec} must exceed ~1.3 V for ECL emission to be observed under these conditions.[37] Figure 6.1b is a luminescence micrograph showing the ECL emission when the total voltage applied across the horizontal channel (E_{tot1}, Scheme 6.1) is 20.0 V and E_{tot2} = 0 V, which is equivalent to $\Delta E_{elec} \approx$ 2.5 V. In this case, ECL is

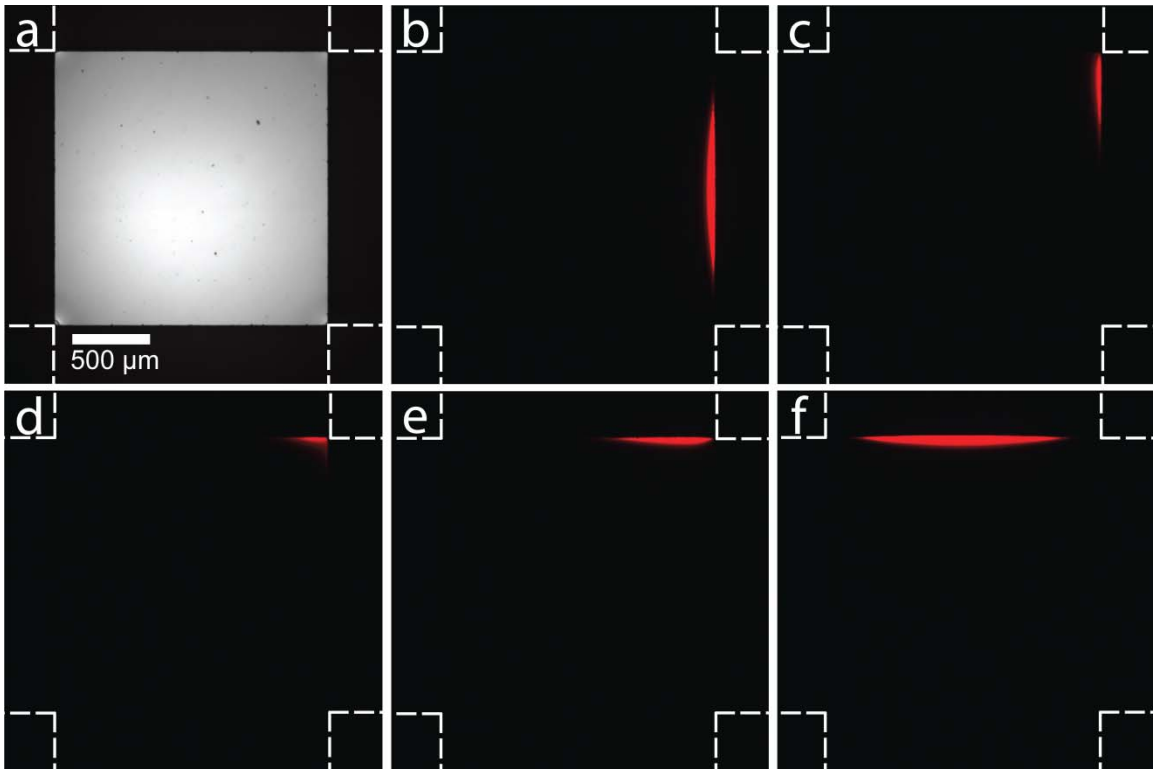

Figure 6.1. (a) Optical micrograph of the 1.75 x 1.75 mm BPE illustrated in Scheme 6.1. The remaining frames show the ECL intensity resulting from application of E_{tot1} and E_{tot2} values of (b) 20.0 and 0 V; (c) 17.3 and 10.0 V; (d) 14.2 and 14.2 V; (e) 10.0 and 17.3 V; and (f) 0 and 20.0 V, respectively.

emitted just at the right edge of the BPE. However, when a driving voltage is applied to both channels, such that the vector sum remains geometrically constant, the location of the ECL emission is localized on different sections of the 2D-BPE. For example, when E_{tot1} = 17.3 V and E_{tot2} = 10.0 V, the light emission moves to the upper-right edge of the BPE (Figure 6.1c). Likewise, when E_{tot1} and E_{tot2} are changed to the values shown in the caption of parts d, e, and f of Figure 6.1, light emission moves counter-clockwise around the perimeter of the BPE.

Visualizing the Electric Field. To better understand the electric field distribution in the vicinity of the channel intersection, the single BPE shown in Figure 6.1a was replaced with an array of BPEs (Figure 6.2a). In this case, each electrode in the array experiences a different value of ΔE_{elec}, depending on its position, and therefore the ECL intensity provides a map of the field gradient. In the optical micrograph shown in Figure 6.2a, the lighter regions are the Au BPEs and the dashed white lines delineate the walls of the PDMS microfluidic channels. Figure 6.2b is a luminescence micrograph obtained in the same region of the microfluidic device shown in Figure 6.2a when E_{tot1} = E_{tot2} = 45.0 V. The non-uniform potential gradient shown in Figure 6.2b demonstrates the driving force for localization of

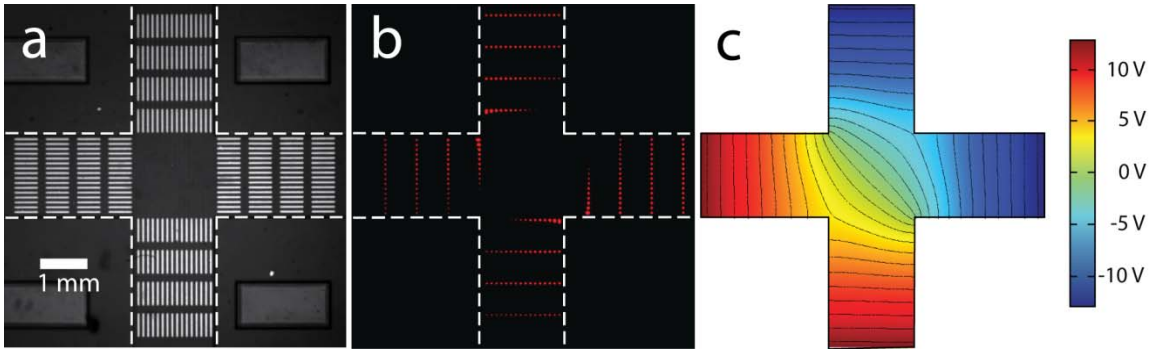

Figure 6.2. (a) Optical micrograph of the 2D microfluidic channel showing the positions of the four BPE electrode arrays. Each array consists of four columns, with 16 BPEs per column. The individual BPEs are 500 µm long and 50 µm wide. The channel dimensions are given in Scheme 6.1. The channels are filled with an aqueous, air-saturated solution containing 5.0 mM $Ru(bpy)_3^{2+}$and 25.0 mM TPrA in 0.10 M phosphate buffer (pH 6.9). (b) False color luminescence micrograph showing ECL emission from the BPE arrays when $E_{tot1} = E_{tot2} = 45.0$ V. (c) COMSOL Multiphysics simulation showing the potential gradient within the microfluidic channels. Both contour and surface plots represent the potential gradient in the device. The isopotential lines of the contour plot correspond to 1 V.

faradaic processes on a single 2D-BPE. The intensity and location of the emission of red light from the anodic poles of the BPEs reflects the magnitude of ΔE_{elec} between the solution and each BPE: more intense emission covering more of the BPE indicates a higher value of the electric field in that region of the channel.[37] Figure 6.3 shows the effect of four different symmetrically applied values of E_{tot1} and E_{tot2} (Scheme 6.1). As the driving voltages are reduced, fewer of the BPEs experience the necessary threshold potential for ECL emission.

Comparing Experimental Results to Simulations. The experimental results in Figures 6.2b and Figure 6.1 can be compared to finite element simulations of the potential gradient formed when symmetric potentials are applied across the two channels (Figures 6.2c and 6.4, respectively). The simulations indicate that the highest gradients are at the corners connecting oppositely polarized channels. Likewise, the lowest potential differences occur near similarly polarized channels. Comparison of the simulated results with the luminescence micrograph in Figure 6.2b indicates a clear correspondence. Specifically, the simulations indicate that a sufficiently high value of ΔE_{elec} exists to illuminate 13 electrodes in the first rank of each of the four 16 x 4

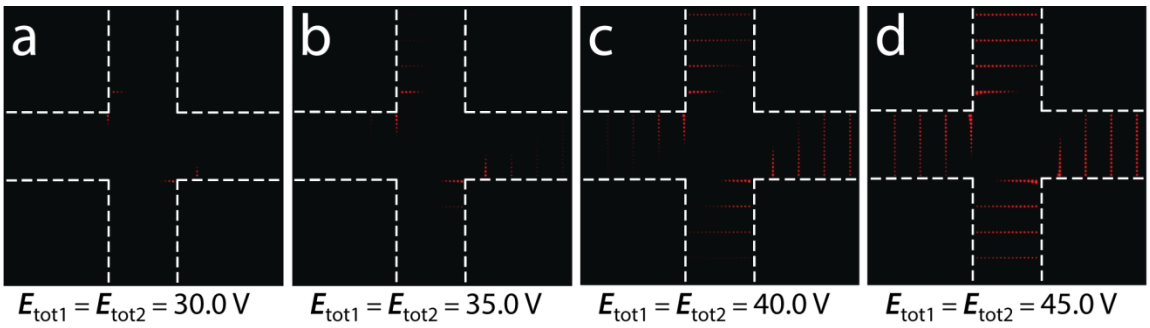

Figure 6.3. False color luminescence micrographs of an array of BPEs like that shown in Figure 6.2 experiencing increasing symmetrical values of E_{tot1} and E_{tot2}. When $E_{tot1} = E_{tot2} = 30.0$ V (a), only those BPEs situated at the intersection of two oppositely polarized channels experience a sufficiently high ΔE_{elec} to produce ECL. As the applied potential biases are increased, more BPEs produce ECL until the potential gradient is high enough to drive ECL on electrodes located away from the intersection and in the channels (d).

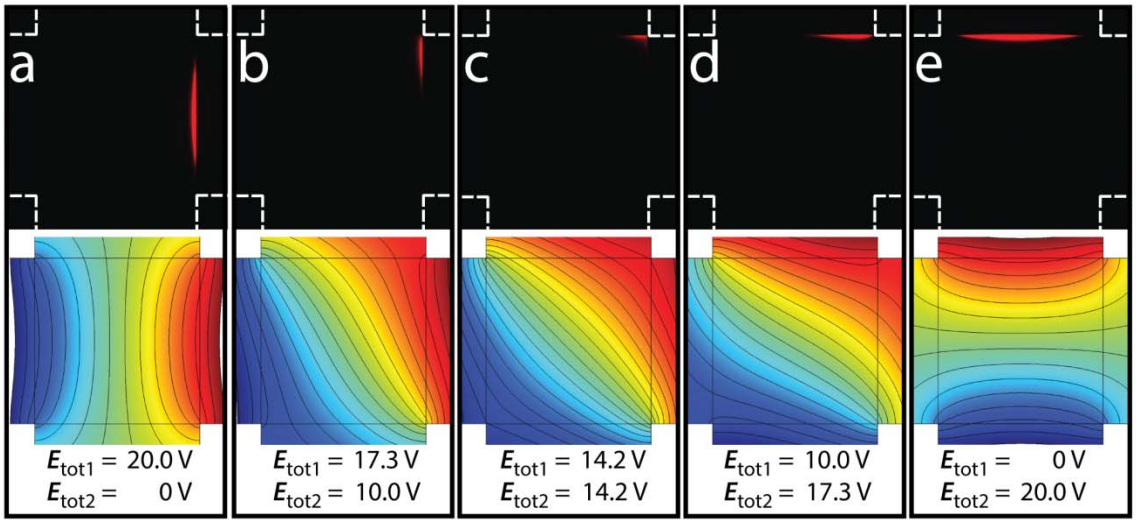

Figure 6.4. Comparing ECL emission from 2D-BPE to simulated potential gradients with varying magnitudes of E_{tot1} and E_{tot2}.

electrode arrays. Experimentally, 11 of the 16 electrodes emit detectable light. This is reasonable agreement given that the simulations do not take into account the finite height of the channels and BPEs, transient effects resulting from the applied potentials and the available current, or the depolarization effect of the BPE array on the potential drop in the channel.[37] Note also that the ECL intensity is highest from those electrodes predicted by the simulations to have the highest value of ΔE_{elec}.

6.5 Summary and Conclusions

To summarize, we have shown that particular locations on the perimeter of a BPE can be electrochemically isolated using a 2D electric field manipulated within the context of crossed microfluidic channels. Moreover, a map of ECL emission from an array of BPEs is in semi-quantitative agreement with simulations of the electric field near the intersection of the channels. Because the 2D-BPE geometry makes it possible to control the potential difference between the solution and electrode at selected locations, one can imagine adapting this approach for applications such as electrochemical sensing, electrochemical synthesis of graded materials,[143] and high-throughput screening of electrocatalytic activity.

Chapter 7: Correlated Electrochemical and Optical Tracking of Discrete Collision Events

7.1 Synopsis

In this chapter we show that optical tracking of collisions between insulating microbeads and an ultramicroelectrode surface are correlated to electrochemical measurements and 3D simulations. The experiments are based on partial blocking of the electrode surface by the spheres. Results obtained using these three methods provide details regarding the radial distribution of landing locations, the extent of current blockage, collision frequency, motion of spheres on the electrode surface following collisions, and aggregation behavior both prior to collisions and afterwards on the electrode surface.

7.2 Introduction

This chapter describes the simultaneous electrochemical and optical detection of individual, fluorescent microbeads interacting with an ultramicroelectrode (UME). The important new result is that electrochemical signals can be directly correlated to optical observations of single particles colliding with and moving about an electrode surface. To the best of our knowledge, specific interactions of this sort have not previously been visualized. To implement this

experiment, an electrochemical cell is configured atop a microscope objective focused on the electrode surface (Scheme 7.1a). The electrode potential is then adjusted such that electroactive molecules present in solution undergo faradaic reactions. When a fluorescent bead strikes the electrode surface it blocks part of the electroactive area, and this results in a current decrease (Scheme 7.1b). Because the beads stick to the surface, these current decreases have a stepped appearance (Scheme 7.1c). Moreover, the magnitude of the steps depends on the landing location of the particles. The results of this study are highly relevant to chemical and biological electrochemical sensing schemes involving single-particle collisions.

Our work is motivated by previous findings from Quinn et al., who reported the chronoamperometric detection of 150 nm and 500 nm carboxyl-functionalized latex spheres.[146] They found that when such beads collide with and irreversibly adsorb to a 2.5 μm UME, the electroactive surface area is reduced sufficiently to partially block oxidation of ferrocenemethanol (FcMeOH). Each time a sphere struck the surface, a step-like decrease in the current (i_{step}) was observed, and these were proposed to correspond to individual collisions. They also found that lowering the conductivity of the solution led to more frequent collisions due to increased mass transfer arising from electromigration

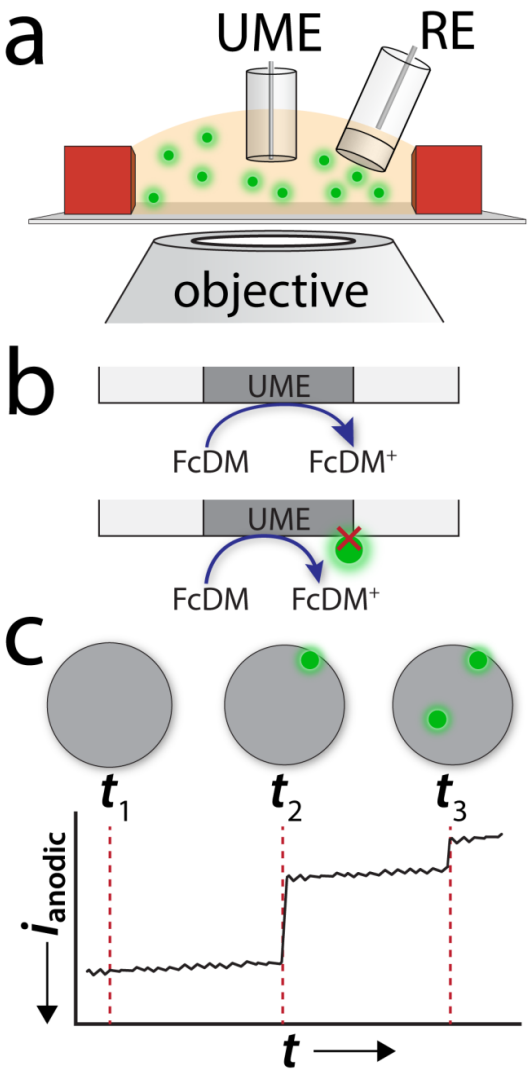

Scheme 7.1. (a) Schematic illustration of the two-electrode electrochemical cell mounted atop a microscope objective for electrochemical and optical tracking of insulating microbeads interacting with the UME. (b) Illustration depicting the blocking of the diffusive flux of FcDM to the UME surface. (c) Schematic illustration depicting the relative intensity of the electrochemical signal on the location of the microbead.

of the negatively charged beads in the vicinity of the electrode. Lemay and co-workers also noted that the magnitude of i_{step} was proportional to the concentration of FcMeOH present in solution. Their work included 2D and 3D finite-element simulations for the approach of an insulating sphere to an active UME.

Bard and co-workers extended the foregoing findings by reporting collisions of silica and polystyrene (PS) beads (diameters 310 and 530 nm, respectively) at Pt UMEs.[147] They described a series of finite-element simulations correlating the effect of the bead landing location on the magnitude of i_{step} as well as the effect of electromigration on the flux of particles to the electrode surface. These simulations predicted that because the diffusive flux of the electroactive species, and thus the electric field, is highest at the edges of the disk UME, the landing position of the beads favors the electrode perimeter over its center. Bard and co-workers also postulated that occasional very low current transients might correspond to beads moving and, in some cases aggregating, on the surface of the electrode. Additionally, they employed Poisson statistics to predict the likelihood of aggregates of two or more beads colliding with the electrode surface.

In addition to collisions involving insulating particles, colliding particles can also generate signals

through electrocatalytic amplification.[148] Specifically, Bard and Xiao reported single Pt nanoparticle (NP) collisions at UMEs, where the Pt NPs catalyzed H^+ and H_2O_2 reduction at glassy carbon (GC) and Au UMEs, respectively.[149] Compton and co-workers have carried out related experiments, except in their case amplification arises from electrodissolution of Ag NPs.[150] Unwin, Koper, and co-workers used the meniscus formed at the end of a double-barrel micropipette to define an electrochemical cell used to monitor collisions.[151] These groups, and others, have reported many other variants on this same basic experiment over the last few years.[152-165]

7.3 Experimental Section

Chemicals and Materials. 1,1'-ferrocenedimethanol (FcDM) (98%, Sigma Aldrich) and analysis grade KNO_3 (Fisher Scientific) were used as received. The fluorescent beads were specified by the manufacturer as having a mean diameter of 1.04 μm (measured by SEM to be 1.03 ± 0.06 μm, Figure 7.1) , were composed of poly(styrene/divinylbenzidine), were carboxyl functionalized, and modified with a fluorescent dye (excitation = 480 nm, emission = 520 nm) (FC04F, Bangs Labs, Fishers, IN). Aqueous solutions were prepared using HPLC-grade water. All solutions were filtered

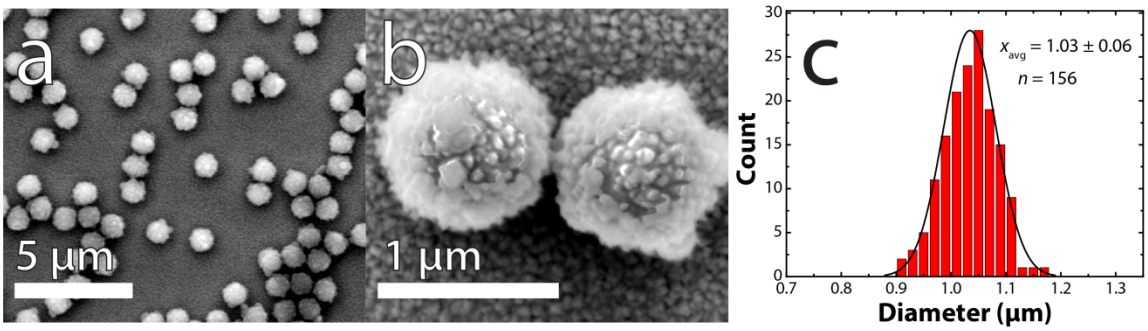

Figure 7.1. Sizing of insulating microbeads. (a) and (b) Scanning electron micrographs of microbeads dropcast onto a conductive ITO support having been coated with a thin (~10 nm) coating of Pd/Pt to reduce charging effects in the electron beam. (c) Histogram showing the measured diameters of 156 individual beads from SEM micrographs like that shown in (a). Dynamic light scattering measurements indicate that the beads have an average diameter of 1.1 ± 0.2 µm.

using a 0.2 µm PTFE filter prior to use in experiments. The 10.0 µm Pt UME was purchased from CH Instruments (Austin, TX).

Equipment and Experimental Setup. The electrochemical cell consists of a silicone gasket placed on a No. 1 coverslip (24 x 60 mm, VWR). Prior to collision experiments, the Pt UME was polished using 0.05 µm alumina, rinsed under a strong stream of Milli-Q water (18.2 MΩ-cm), and sonicated in Milli-Q water for 10 min. Once cleaned, the UME was mounted on an *x,y,z*-micropositioner and placed in the electrochemical cell, which was set on the stage of an inverted epifluorescence microscope (Eclipse TE 2000-U, Nikon, Tokyo, Japan) (Scheme 7.1a). A 60x objective (CFI Plan Fluor 60x C, Nikon) was used with a 1.5x intermediate magnification. The working distance of the objective is 0.30 mm. Therefore, the distance separating the UME and the top of the coverslip was ~150 µm. Images and movies were captured using a CCD camera (Cascade 512B, Photometrics, Tucson, AZ) controlled by V++ Precision Digital Imaging (Auckland, New Zealand) software. In order to maintain a suitable time resolution (7 fps) for the entire duration of the collision experiments (>10 min), a screen capture software package (Total Screen Recorder, Guangzhou, China) was used to collect movies. Figure 7.2 shows the ratio of

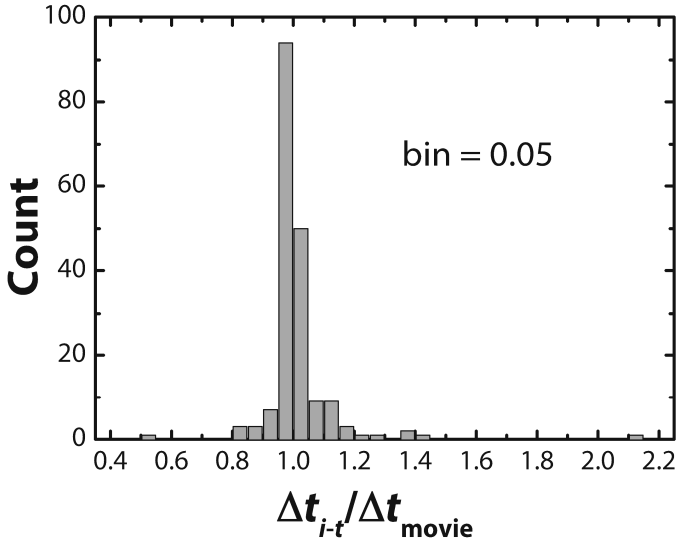

Figure 7.2. Histogram showing the ratio of $\Delta t_{i\text{-}t}$ to Δt_{movie}. Δt designates the time between consecutive collisions. Small or large values of $\Delta t_{i\text{-}t}/\Delta t_{movie}$ correspond to closely spaced events where the time resolution of the movie (7 fps) the *i-t* trace (0.1 s sample interval) lead to a slight discrepency. Most events occurred near the expected ratio of 1.0.

movie timings to those in the *i*-*t* traces. Deviations from the ideal ratio are the result of very closely spaced events.

CVs and *i*-*t* data were collected using a Chem-Clamp (Dagan Corp., Minneapolis, MN) functioning as a potentiostat with the voltage signal generated by a PAR 175 (Princeton Applied Research, Oak Ridge, TN) waveform generator. These were interfaced to a Dell PC using a PCI-6251 data acquisition board (National Instruments, Austin, TX) *via* a BNC-2090A analog breakout accessory, and the data were measured using custom LabView 2010 software (National Instruments, Austin, TX). CVs and *i*-*t* traces were collected with a sampling frequency of 10 Hz and a gain of 1 mV/pA. A Ag/AgCl reference electrode was used as both reference and counter electrode in a two-electrode electrochemical setup. A homebuilt Faraday cage was used on the microscope stage to isolate the system from environmental electrical noise.

Estimation of D_{FcDM}. The diffusion coefficient for FcDM (D_{FcDM}) was estimated using the slope of a linearized Cottrell plot for individual single potential steps (i vs. $t^{-1/2}$) at two glassy carbon macro electrodes (GCEs) (r = 1.5 mm) and steady state currents (i_{lim}) at a series of UMEs of known r in a solution containing 1.00 mM FcDM and 0.10 M KNO_3. The experiments were performed using a CH Instruments 700E

potentiostat in a three electrode cell. The calculated value of D_{FcDM} was 6.4 ± 0.2 x 10^{-6} cm^2/s. This is in reasonable agreement with several reported literature values in similar systems (D_{FcDM} = 6.7 x 10^{-6} cm^2/s,[166] 5.9 (±0.9) x 10^{-6} cm^2/s,[167] and 6.1 x 10^{-6} cm^2/s[168]).

Finite Element Simulations. Finite-element simulations (FES) were performed on a Dell T7500 equipped with a Dual Six Core Intel Xeon processor (2.40GHz) and 24GB of RAM, running on a Windows 7 64-bit operating system. Simulations were carried out using COMSOL Multiphysics (version 4.3). Simulations were performed in 3D, taking advantage of a single plane of symmetry, reducing computation time (Figure 7.3). A spherical geometry was used with two spherical domains concentric with respect to the UME (r = 5 µm). The inner domain had a radius of 12.5 µm and an extremely fine mesh, while the outer domain had a radius of 500 µm with a significantly coarser mesh. This geometry was further split into two separate domains, and a boundary layer mesh was placed over the entire electrode surface. The complete mesh consisted of over 2.1 x 10^7 elements.

The outermost boundaries were taken to be concentration boundaries representing the bulk solution (C = 5 mM), while the UME was taken as the surface concentration under mass-

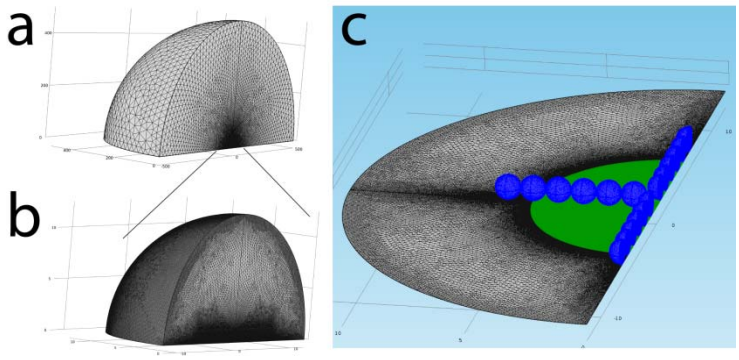

Figure 7.3. Geometry used for the finite-element simulations. (a) Entire geometry and mesh. Outer domain (r = 500 µm) with an exponentially increasing mesh size. (b) Close-up of the inner domain (r = 12.5 µm) which as an extremely fine mesh. Both inner and outer domains are concentric with the surface of the electrode. (c) Near-surface mesh of 1.03 µm diameter insulating spheres (blue) resting 10 nm above the surface of the electrode (green, r = 5 µm). This 10 nm spacing was required to properly mesh this geometry. The spheres can be activated (insulating) by creating a no-flux boundary across the surface of the sphere. Conversely, they can be deactivated by treating the domain as continuous.

transfer limited conditions (C = 0). The limiting current determined by FES was found to be within 1% of the theoretical value. An array of microspheres was then placed in close proximity (10 nm) to the UME surface along the plane of symmetry, and the domains describing them were selectively excluded from the physics model calculation. This was done in order to prevent localized differences in the mesh surrounding the spheres from having an effect on the predicted value of i_{step}.

7.4 Results and Discussion

Here, we show that it is possible to simultaneously track carboxyl-modified fluorescent PS beads (diameter = 1.03 ± 0.06 μm) using optical microscopy and electrochemical methods. Our experiment is carried out using a 10.0 μm Pt UME immersed in a solution containing the beads, 5.0 mM FcDM, and 5.0 mM KNO_3 as a supporting electrolyte (Scheme 7.1a). When the electrode is held at a potential at which FcDM is oxidized at the mass-transfer-limited rate (i = i_{lim}), the negatively charged beads are attracted to the electrode *via* electromigration, and their arrival at the surface of the electrode is monitored both optically and electrochemically.

Collision Experiments. Experiments were carried out as follows. First, the electrochemical cell was filled with 250

µL of the FcDM + KNO_3 solution in the absence of beads. Cyclic voltammograms and *i-t* traces were then collected to ensure acceptable noise levels and value of i_{lim} (Figure 7.4). Second, 250 µL of a 100 fM bead solution, also containing supporting electrolyte, was injected into the cell, resulting in a final bead concentration of 50 fM. Third, the potential of the UME was stepped from 0 to 0.50 V vs. Ag/AgCl, which results in $i = i_{lim}$. Figure 7.5 is an *i-t* trace of collision experiment as described, showing the first 600 s after the potential step. The upper left frame of Figure 7.6a is an optical micrograph of the Pt UME used in this study. The remaining frames in Figure 7.6a show the collision of each of 10 fluorescent beads with the surface of the UME. Figures 7.6b to 7.6d are *i-t* traces that correspond to the optical micrographs, and the numbered current steps are correlated to the numbered micrographs. For example, bead 2 first strikes the electrode about halfway (2.2 µm) along the radius of the UME. It then moves to the outer edge of the electrode at about the same time as bead 3 hits the surface. Beads 7 and 8 appear to oscillate on the surface shortly after colliding, causing a noticeable change in the apparent noise in the *i-t* trace (Figure 7.5d). Figure 7.7 shows a series of micrographs of a Pt UME before and after a collision experiment, indicating the types of bead coverages achieved for long experiment durations.

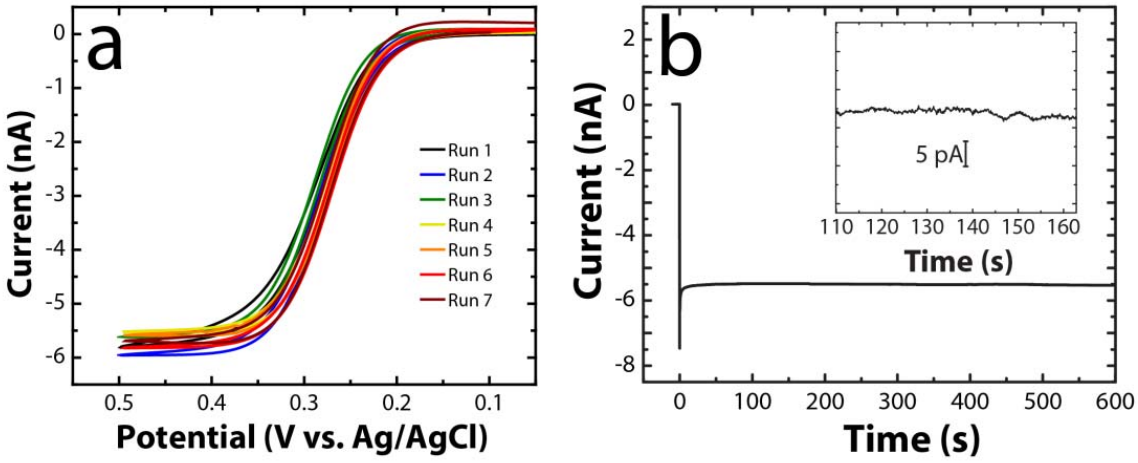

Figure 7.4. (a) Cyclic voltammograms of 5.0 mM FcDM in 5.0 mM KNO_3 at a 10 µm Pt UME for seven individual collision experiments immediately prior to the injection of beads. The steady state current (i_{lim}) at a disk UME is given by eq 7.1.[55]

$$i_{lim} = 4nFDCr \qquad (7.1)$$

Where n is the number of electrons, F is the Faraday constant, D is the diffusion coefficient, C is the bulk concentration of FcDM, and r is the radius of the disk UME. The concentration of FcDM was 5.0 mM and the value of 6.4 x 10^{-6} cm^2/s was used for D. The calculated i_{lim} is 6.2 nA, and the average experimental value of i_{lim} was 5.8 ± 0.2 nA. The slight difference between these two values might be a consequence of the non-ideal cell geometry required for the *in situ* analysis. (b) i-t trace obtained in the *in situ* electrochemical cell after stepping the electrode potential from 0 to 0.50 V vs. Ag/AgCl. The inset is a close-up view showing the noise level of the i-t trace. Immediately after these data were collected, a solution containing the beads was injected into the cell to yield a final bead concentration of 50 fM, with the concentrations of FcDM and KNO_3 remaining constant.

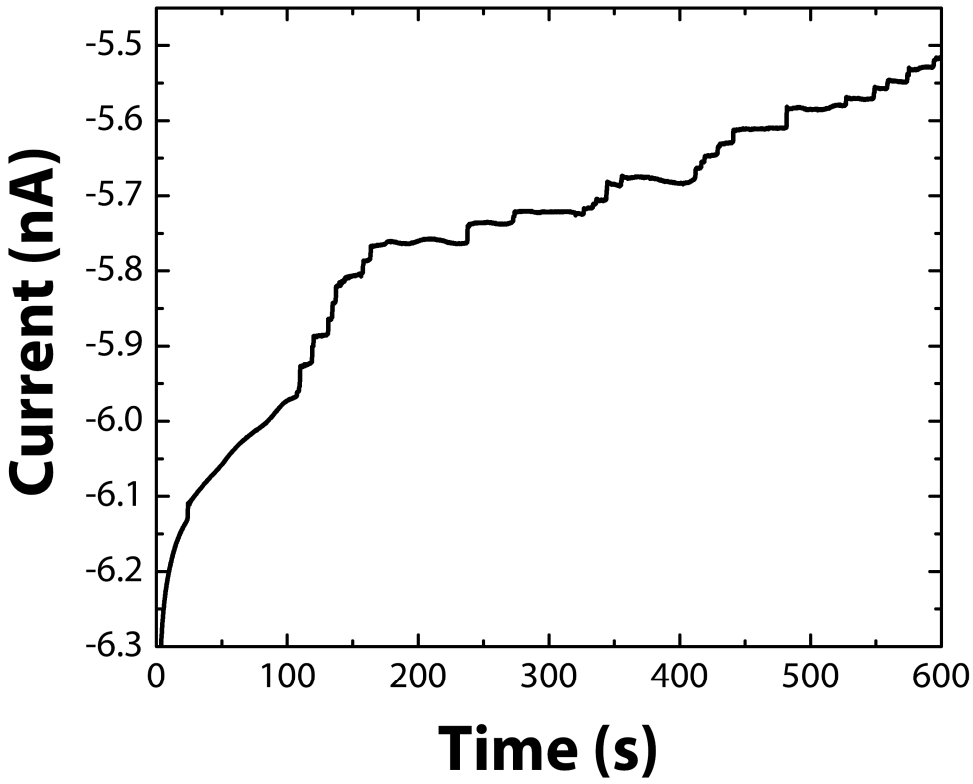

Figure 7.5. Chronoamperometric (*i*-*t*) trace for a collision experiment with 50 fM beads in a solution of 5 mM FcDM and 5 mM KNO_3 for the first 600 s of the potential step.

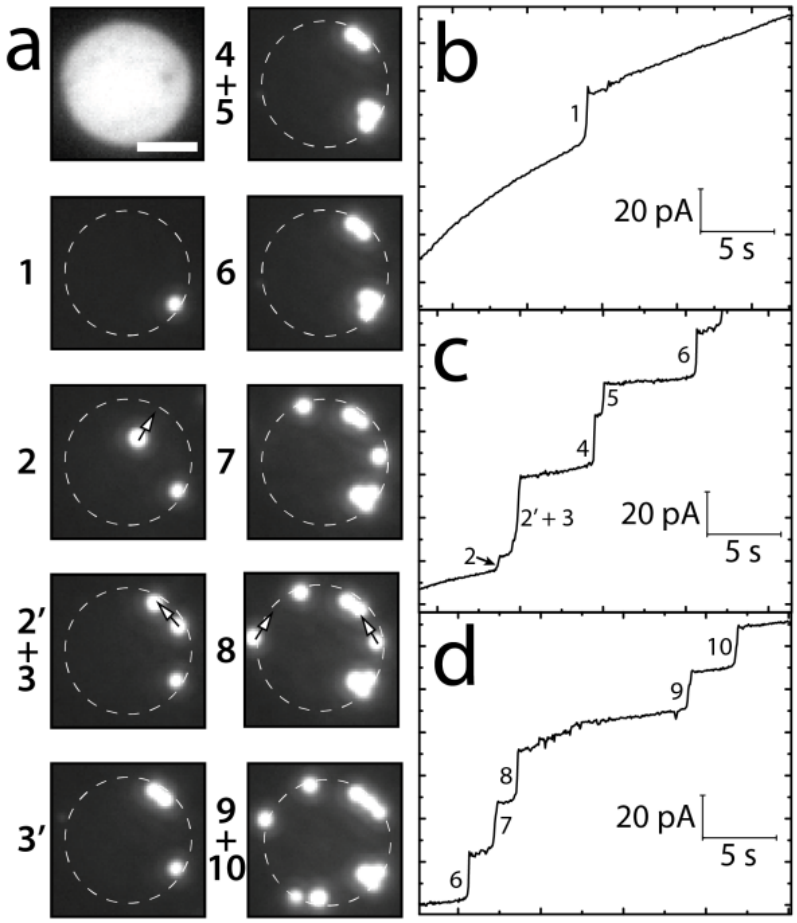

Figure 7.6. (a) A series of micrographs showing bead collisions at a Pt UME. (top left) Optical micrograph of the 10 µm Pt UME (the white scale bar indicates 5 µm). The numbers to the left of each frame indicate which bead collision is represented in that frame. Arrows have been added to show the motion of the beads on the electrode surface following collisions. (b-d) Chronoamperometric (*i*-*t*) traces obtained during the movie. The time correlated collision from the movie frames (part a) and the *i*-*t* traces (parts b-d) are indicated by the numbers in each frame. Notice that after beads 7 and 8 collide with the surface, they are observed to move on the surface in the direction of the arrows. This leads to an increase in the apparent noise between the landing time of beads 8 and 9 in the trace shown in part (d).

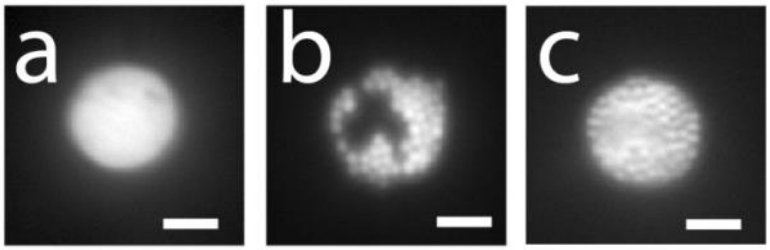

Figure 7.7. Micrographs of a collision experiment. (a) Optical micrograph of Pt UME prior to the collision experiment. The white scale bar represents 5.0 µm. (b) Fluorescence micrograph of the same UME shown in (a) after 1700 s after a potential step from 0 to 0.50 V vs. Ag/AgCl. (c) Optical micrograph of the same electrode after the collision experiment.

Collision Location Matters. The most interesting result of these experiments is that the locations of bead collisions can be directly correlated to the size of the current step in the *i*-*t* trace. To achieve this, the location of each bead is determined using the general approach shown in Figure 7.8a. Specifically, the centroid of the first bead striking the electrode surface is determined by maintaining a high intensity of excitation light, which provides sufficient illumination to view the UME. Once the position of the first bead is established relative to the UME, a neutral density filter is inserted into the optical path of the excitation source to reduce the excitation intensity. Next, the positions of subsequent beads colliding with the UME are established relative to the first bead. Figure 7.8b is a scatter plot showing the measured value of i_{step} vs. radial distance of bead center from UME center (r_{b-e}) for each of ~150 bead collisions. Figure 7.9 shows the results when two-bead aggregates collide with the surface, a result that would be difficult to confirm without the fluorescence data.[147] These data demonstrate that the magnitude of i_{step} depends on the location of the collision of the beads. Larger values of i_{step} are observed for collisions near the edge of the electrode than the center. Also, beads tend to collide with greater frequency at the edge of the electrode than at the center (see Figure 7.10). The frequency of bead

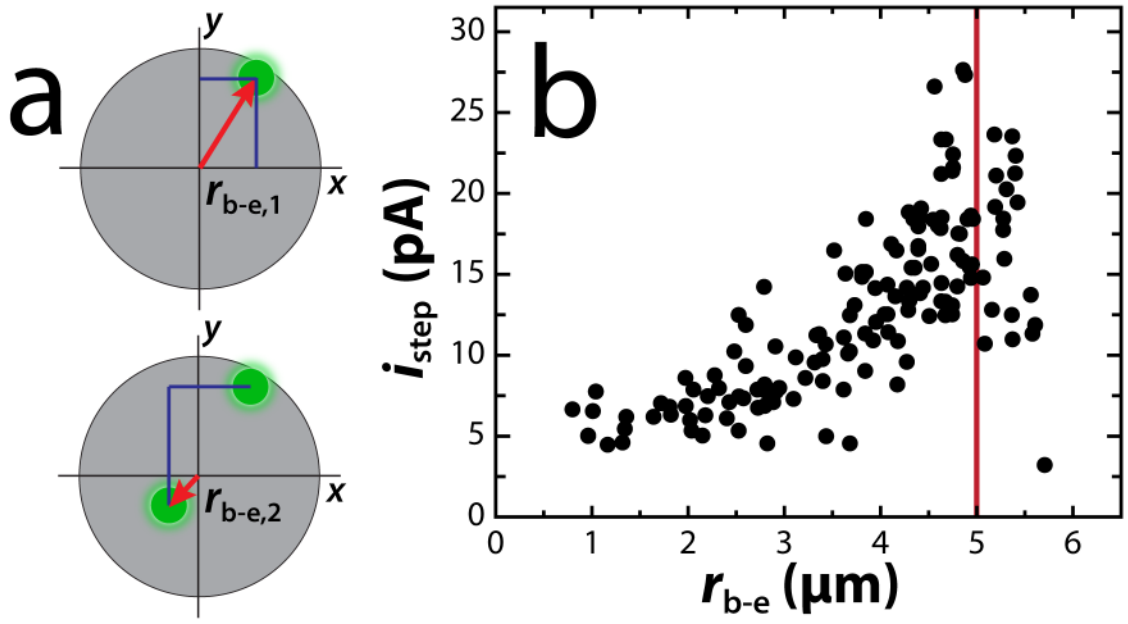

Figure 7.8. (a) Schematic illustration showing the method used to determine radial bead distance from UME center ($r_{b\text{-}e}$). The first bead to collide was calibrated against the framework of the UME and the x,y coordinates (lines) converted to radial coordinates (arrow). The location of subsequent collisions was measured relative to the position of a previously arrived bead, again converting relative differences in x,y coordinates (lines) to radial coordinates (arrow). (b) Scatter plot of i_{step} vs $r_{b\text{-}e}$ for ~150 collisions recorded using chronoamperometric and fluorescence data, respectively. Only collisions occurring within the first 600 s of the potential step are shown. The line indicates the radius of the UME.

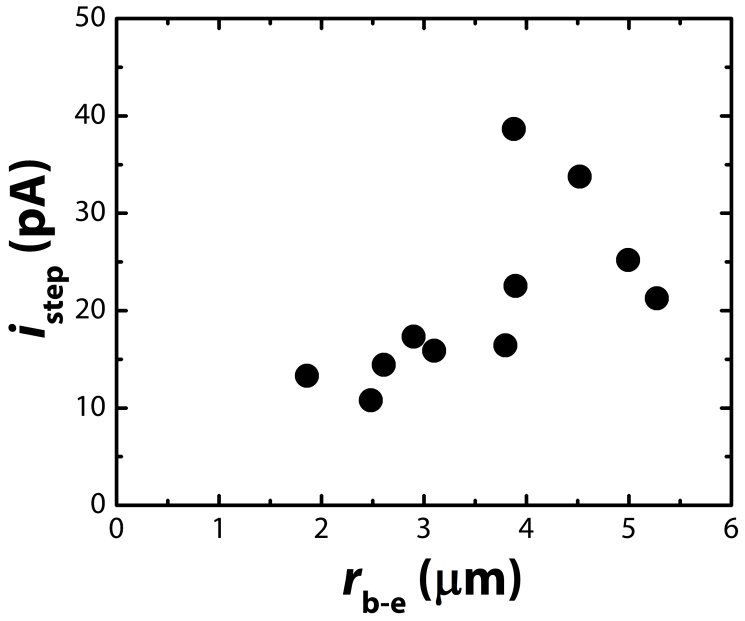

Figure 7.9. Plot of i_{step} vs. radial distance of bead center from UME center ($r_{b\text{-}e}$) for two-bead aggregates as determined by optical tracking.

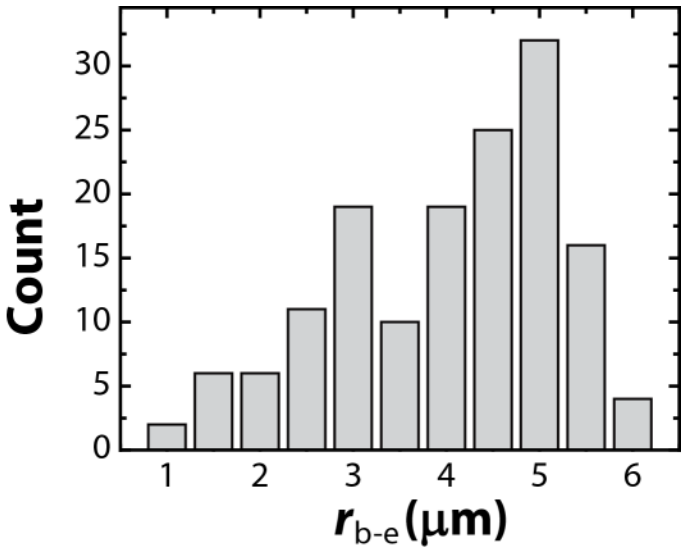

Figure 7.10. Histogram showing the number of collisions within bins centered at the indicated distances from the center of the UME ($r_{b\text{-}e}$).

collisions also decreases with time. Nearly twice as many beads arrive in the first 300 s of the potential step compared to the following 300 s. Another interesting point is that beads colliding on the insulating shroud near the edge of the electrode also cause measureable values of i_{step}, because they still block FcDM flux to the surface of the electrode. This implies that the magnitude of i_{step} is not caused solely by blocking portions of the electrode surface, but also by other perturbations of the diffusion layer.

Comparing Collision Experiments to Simulations. In Figure 7.11a, the results in Figure 7.8b have been binned into 0.5 μm increments so that they can be directly compared to 3D finite-element simulations. The experimental and simulated results are compared in Figure 7.11a and are within ~1.5 pA (~20%) of one another, which is close to the experimental error given that the baseline noise is on the order of 1 pA peak-to-peak (Figure 7.4b, inset). Additionally, the distribution of particle sizes (Figure 7.1) also impacts the magnitude of i_{step} for each collision, which contributes to the scatter. An illustration of this point can be found in Figure 7.12, which shows simulated values of i_{step} for beads of varying diameters. Figure 7.11b shows the effect of beads centered at several different values of $r_{b\text{-}e}$ on the diffusive

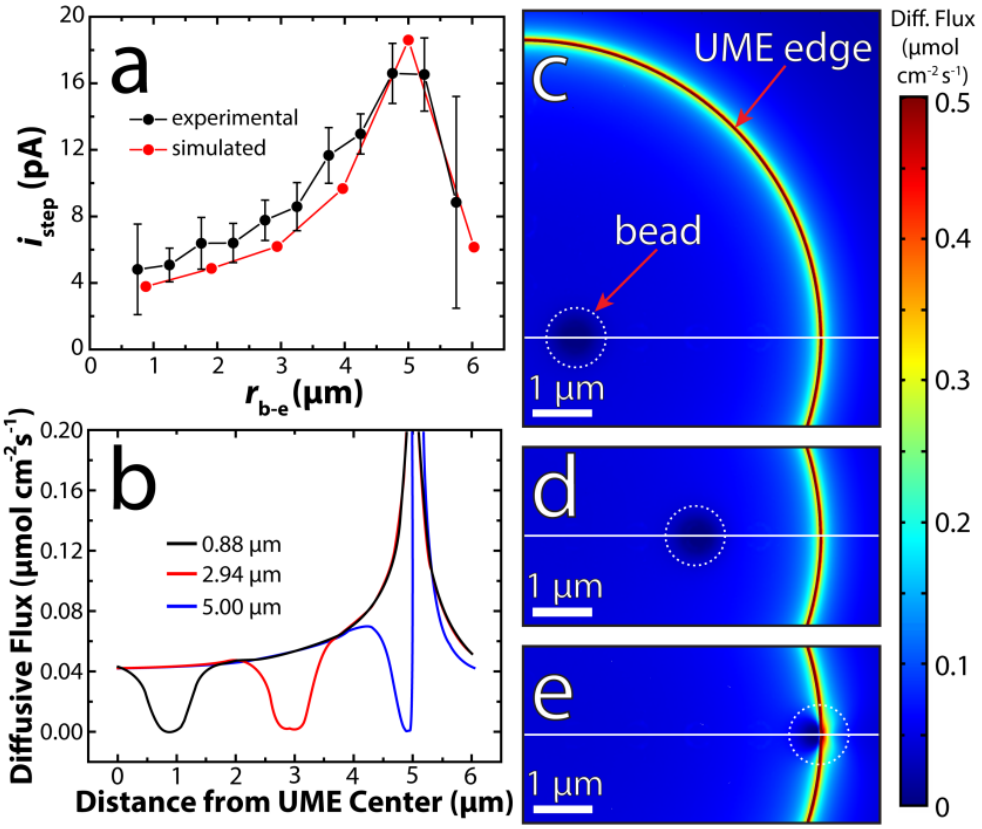

Figure 7.11. (a) Plot of i_{step} vs r_{b-e}. The black symbols represent data from Figure 7.5b that was binned into increments of 0.5 μm. The error bars represent the 95% confidence interval for collisions that occurred within the indicated bin. The red circles represent simulated data for the difference in steady-state current at a UME having an insulating spherical particle (1.03 μm) centered at the indicated distance from the center of the UME vs. the steady-state current at the bare electrode. (b) Simulated diffusive flux profile across the length of the radius of the UME for different values of r_{b-e}. The maximum flux was 4.2 μmol cm^{-2} s^{-1}, but the color scale was truncated to more clearly show the effect of the insulating beads. (c-e) Surface plots of diffusive flux over a portion of the surface of the UME for r_{b-e} = 0.88 μm (c), 2.94 μm (d), and 5.00 μm (e). The location of the spheres is indicated by the dashed white circle and the white line represents the radius of the UME.

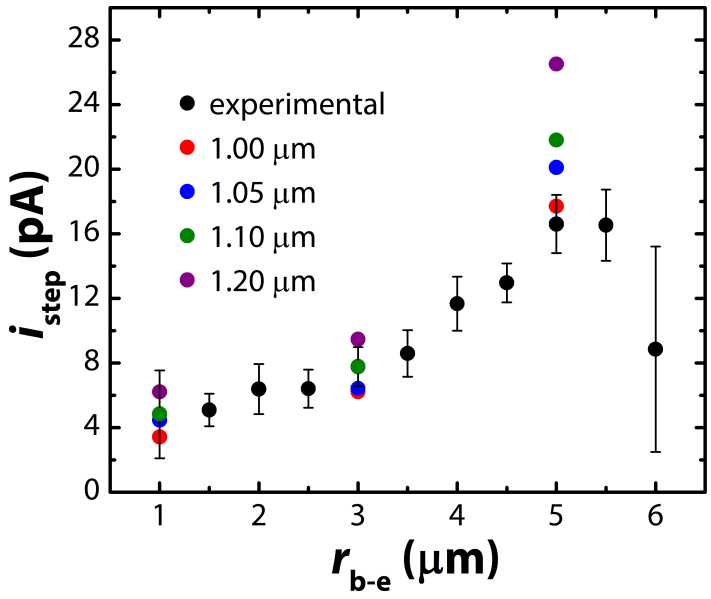

Figure 7.12. Comparison of experimental data for experimental i_{step} values and those obtained for beads of different diameters.

flux profile along that radius. This clearly demonstrates why beads at the edge of the disk cause larger values of i_{step}: more FcDM flux is blocked at the edges because a disk UME is not uniformly accessible.[55] Figures 7.11c-7.11e are simulated surface plots of the diffusive flux at the disk UME with beads centered at the same r_{b-e} values as in Figure 7.11b. Using these types of simulations, it is possible predict i_{step} for a bead as it moves to different positions on the electrode surface following an initial collision, collision events occurring in close spatial proximity, and collisions of two-bead aggregates, though this level of sophistication is beyond the scope of this initial report. For now, however, we are satisfied, that the electrochemical, optical, and theoretical results are in good agreement.

7.5 Summary and Conclusions

In conclusion, we have used optical tracking and simulations to show that the location of a bead collision on an active UME is related to the magnitude of the resulting current steps. Moreover, details relating to the motion of beads on the electrode surface following collisions, including aggregation behavior, have also been revealed by the optical experiments.

Chapter 8: Wire, Mesh, and Fiber Electrodes for Paper-based Electroanalytical Devices

8.1 Synopsis

In this chapter we report the use of microwire and mesh working electrodes in paper analytical devices fabricated by origami paper folding (*o*PADs). The important new result is that Au wires and carbon fibers having diameters ranging from microns to tens of microns can be incorporated into *o*PADs, and that their electrochemical characteristics are consistent with the results of finite element simulations. These electrodes are fully compatible with both hollow channels and paper channels filled with cellulose fibers, and they are easier to incorporate than typical screen-printed carbon electrodes. The results also demonstrate that the Au electrodes can be cleaned prior to device fabrication using aggressive treatments, and that they can be easily surface modified using standard thiol-based chemistry.

8.2 Introduction

In this chapter we report paper-based microelectrochemical devices that incorporate conductive wires as electrodes (Scheme 8.1). The important new result is that the identity and preparation of the wire can be customized to meet the specific requirements of an

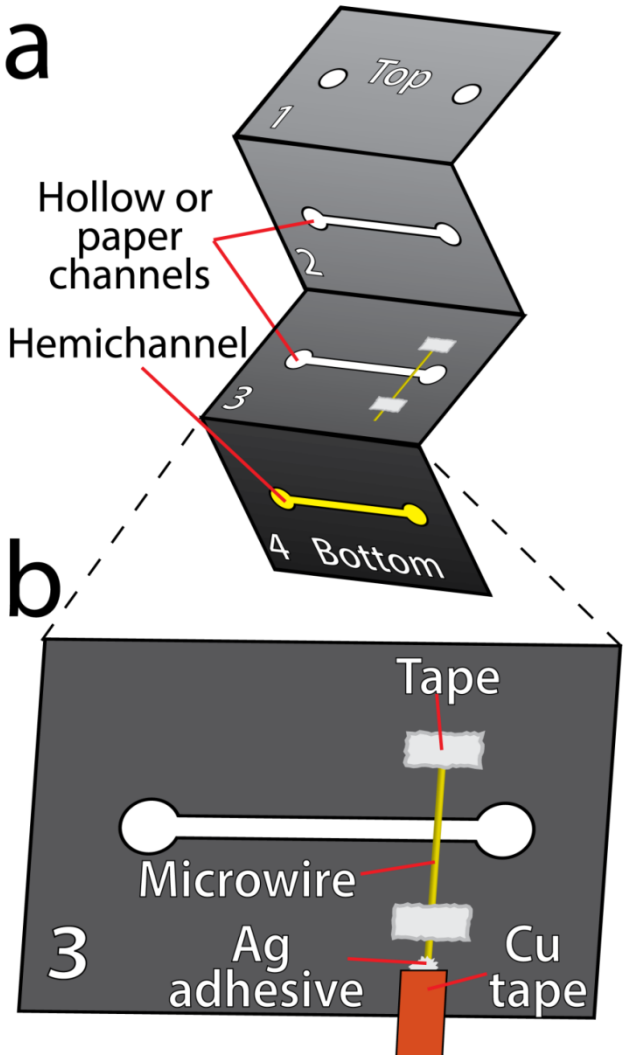

Scheme 8.1. (a) Schematic illustration of the 4 layer *o*PAD device where the top layer (1) contains an inlet and outlet, the middle two layers (2 & 3) contain either a paper channel or hollow channel, and the bottom layer (4) contains a partially hydrophilic hemichannels. A microwire is inserted between Layers 2 & 3 to act as a working electrode in an electrochemical PAD. (b) Zoom in view of Layer 3, where the microwire is placed showing its attachment and the method used to achieve electrical connection.

electrochemical method or assay. This greatly expands the versatility of paper analytical devices (PADs), because at present nearly all PADs employ screen-printed carbon electrodes, which are only partially conductive,[169,170] usually have high surface areas,[171] and are difficult to surface-modify with receptors.[172,173] Additionally, fabrication of PADs incorporating microwire electrodes is significantly easier than current methods for preparing screen-printed electrodes, and allows the electrode to be placed at any location within the device. We show that Au wires and C fibers can be used as electrodes in PADs based on the principle of origami (*o*PADs). Furthermore, these wire electrodes can be suspended within open channels of paper fluidic devices or between two cellulosic paper channels. Additionally, electrode pretreatments, such as piranha cleaning and modification with self-assembled monolayers (SAMs), can be achieved external to the PAD prior to incorporating them into the device. Finally, this approach makes it possible to change the location of the microwire electrodes and to integrate wire electrodes with screen-printed electrodes when appropriate.

The Whitesides group reported the first examples of two- and three-dimensional fluidic devices built on cellulosic paper platforms.[174,175] Since that time, the intrinsic advantages of paper-based devices, including easy

fabrication, low cost, and simple disposal, have led to a renewed interest in paper-based point-of-care (POC) sensing devices.[176-178] Detection in PADs is typically by naked-eye observation of color change,[179-181] fluorescence,[182-184] or electrochemical methods.[172,185-187] Of these, electrochemistry provides a good combination of simplicity, low power requirements, low LODs, and ease of quantitation.[188,189] Indeed, since the first report of electrochemical detection on a PAD by Henry and co-workers, the popularity of this method has rapidly increased.[185,186,190-193] Although nearly all electrodes that have been reported for use in PADs are on the millimeter length scale, there are numerous potential advantages to using smaller dimension electrodes. These include lower capacitances, higher rates of mass transfer, and lower overall currents, leading to reduced ohmic drop (particularly important in PADs) and allowing the use of two-electrode cells.[55,194] Some of these advantages have already been demonstrated by Henry and co-workers, who showed that a microelectrode could be produced in a PAD by creating a hole in a plastic transparency film and filling the resulting hole with C paste.[195]

An unmet need in the field of paper fluidics is the development of better electrode fabrication methods. As mentioned previously, screen-printed carbon electrodes are the current standard for PADs. Such electrodes are produced

by pushing a viscous ink containing graphitic carbon suspended in a polymer matrix through a patterned mesh screen or inscribing the ink within a stencil to yield a well-defined shape. The primary problems with this approach are the poor electrical properties of the resulting electrodes and their irreproducible surface chemical properties. As an alternative, we propose the use of prefabricated microwire electrodes. Microwires have been used in a variety of electroanalytical systems. For example, Osteryoung and co-workers used C fibers for investigating the electrochemical behavior of *n*-acetylpenicillamine.[196] Henry and co-workers demonstrated post-separation amperometric detection in capillary electrophoresis using a microwire.[197] Additionally, microwires have found use in anodic stripping voltammetry of trace metals.[198,199] The advantages of this type of approach are many, but can be summarized on the basis of flexibility in the choice of electrode material, maintaining the ease of device fabrication and rapid prototyping, and perhaps most importantly, the ability to modify electrodes prior to device assembly. Within the context of paper fluidics, this latter advantage is quite similar in concept to our previously reported practice of placing receptors on microbeads,[191] rather than directly modifying cellulose fibers[200,201] or relying on physisorption.[202,203]

8.3 Experimental Section

Chemicals and Materials. The following chemicals were used as received unless otherwise noted in the text: ferrocenemethanol (FcMeOH) (97%, Sigma-Aldrich), hexaammineruthenium(III) chloride ($Ru(NH_3)_6Cl_3$) (98%, Acros), potassium ferricyanide ($K_3Fe(CN)_6$) (99.99% metals basis, Sigma-Aldrich), potassium nitrate (KNO_3) (99%, EM Sciences), 11-(ferrocenyl)undecanethiol (95%, Sigma-Aldrich), mercaptohexane (Acros), 11-mercaptoundecanoic acid (MUA) (95%, Sigma-Aldrich), ethanol (100%, Capitol Scientific, Austin, TX), hydrogen peroxide (H_2O_2) (30% v/v in H_2O, Fisher Scientific), HPLC grade water (Fisher Scientific), and sulfuric acid (H_2SO_4) (95% H_2SO_4, Fisher Scientific). Whatman grade 1 chromatography paper (20 x 20 cm sheets) was purchased from Fisher Scientific. Au wire (nominal diameter = 0.05 mm, measured diameter = 51.3 ± 0.2 µm, 99.99% Au) was purchased from Alfa-Aesar. Carbon fibers (nominal diameter = 10 µm, measured diameter = 9.95 ± 0.2 µm) were from Goodfellow (Coraopolis, PA). Gold gauze, 100 mesh woven from 0.064 mm diameter wire (99.99%, metals basis) was purchased from Alfa-Aesar. Figure 8.1 shows scanning electron micrographs of the Au wire and C fiber.

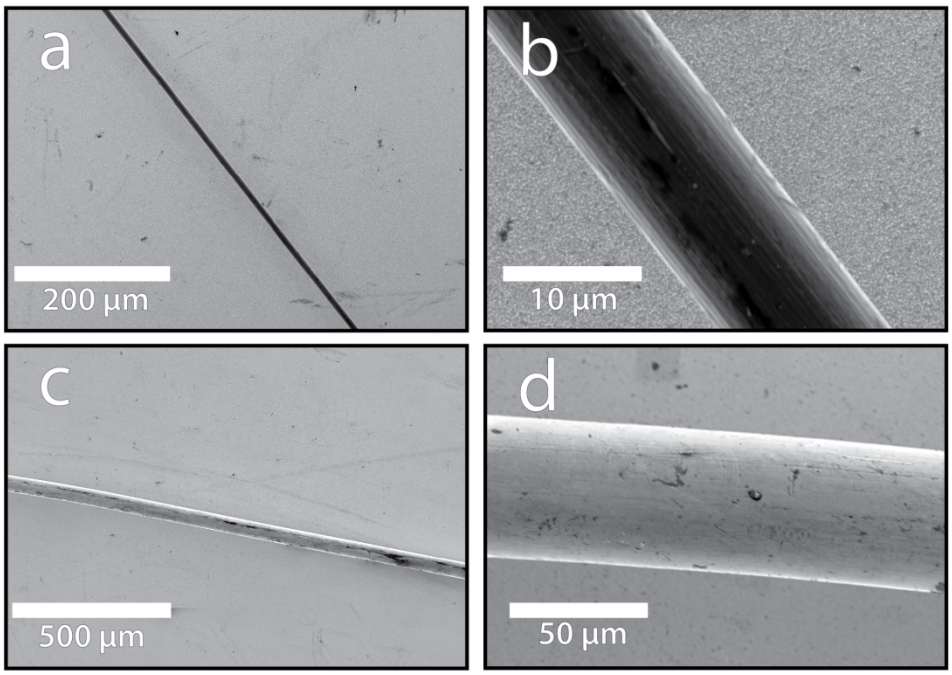

Figure 8.1. Scanning electron micrographs of the carbon fiber and Au wire electrodes used in this study. The SEM used in this study was a Quanta 650 FEG ESEM system. (a and b) Micrographs of C fiber. (c and d) Micrographs of Au wire. The measured diameter of the Au wire was 51.3 ± 0.2 µm and the measured diameter of the C fiber was 9.95 ± 0.2 µm.

The carbon (CI-2042) and Ag(83%)/AgCl(17%) (CI-4002) inks were purchased from Engineered Conductive Materials (Delaware, OH). All aqueous solutions were prepared using deionized water (Milli-Q, 18.2 MΩ·cm).

Device Fabrication. The paper channel *o*PADs (PC-*o*PADs) and hollow channel *o*PADs (HC-*o*PADs) were fabricated using a previously reported wax-printing method.[204] The patterns were printed onto Whatman grade 1 chromatographic paper using a Xerox 8570DN inkjet wax printer. After printing, the paper was placed into an oven at 135 °C for 45 s to melt the wax and allow it to spread into the paper matrix. The paper was then cooled to room temperature. HC-*o*PADs where prepared by laser cutting (Epilog Zing 16, Epilog Laser, Golden, CO). The channel dimensions for both PC-*o*PADs and HC-*o*PADs were 1.3 mm wide and 30 mm long. The channels consist of two paper layers, making the final channel height ~0.35 mm.

Au wire electrodes were cleaned by immersion in piranha solution (1:3 H_2O_2/H_2SO_4) for 1 min and then water immediately prior to use. *Caution: piranha solution is a strong oxidant and reacts violently with organic materials. It should be handled with extreme care; all work should be performed under a fume hood and with protective gear.* The C fiber was used as received. Ag conductive adhesive (Electron Microscopy Sciences) and Cu tape (3M) were used to make

electrical contact to the microwires. The wires were placed ~5 mm from the outlet reservoir of the *o*PAD to reduce ohmic drop during electrochemical experiments (in most cases the reference and counter electrodes were placed in the outlet reservoir).

In some cases, *o*PAD configurations were tested in which the working, counter, and reference electrodes were all present within the HC-*o*PAD. In this case, the counter and reference electrodes were stencil-printed onto the bottom of Layer 1 (Scheme 8.1) by pushing carbon ink through a mask, which was a laser-cut plastic transparency. Before stencil-printing, the ink was heated, uncovered, for 30 min in an oven set to 65°C. After letting the ink cool to room temperature, a scraper was used to push the ink through the mask onto the HC-*o*PAD. The HC-*o*PAD was then cured at 65°C for 90 min. After curing the C ink, Ag/AgCl paste was painted onto one of the stencil-printed electrodes and it was cured at 65°C for 30 min. The front edge of the reference electrode was configured to be 5 mm from the microwire, and the back edge of the counter electrode was situated 15 mm from the microwire. Both the counter and reference electrodes spanned the width of the hollow channel and their length was 3 mm. A portion of the screen-printed carbon extended beyond the channel to facilitate electrical contact.

All devices were folded into the final configuration prior to being sandwiched between two rigid, 5-mm thick acrylic holders, which were clamped with binder clips. In the case of HC devices, when solution was added to the cell, the flow was stabilized by adding small additions of solution to the inlet or outlet during the first ~5 min. After that, the cell was allowed to equilibrate for another 10-20 min to reduce the flow rate within the channel. For all experiments described here, this procedure was followed and no flow was intentionally induced.

Preparation of SAM-coated Au Microwires. The Au wire electrodes were cleaned by immersion in piranha solution for 1 min, followed by rinsing in HPLC-grade water. The wires were then immersed in an ethanolic solution of 2.5 mM MUA for 48 h, to create a SAM having a negatively charged terminus, or in a solution of 1.0 mM 11-(ferrocenyl) undecanethiol and 1.0 mM mercaptohexane for 1 h, to prepare electroactive SAMs. The wires were removed from the thiol solutions and dipped into clean ethanol to remove any unbound thiols. The *o*PADs where then assembled as previously described.

Electrochemical Measurements. Electrochemical measurements were carried out at 23 ± 2°C using a potentiostat (Model 650C or 700E, CH Instruments, Austin, TX). Unless otherwise

indicated, the reference electrode was a mercury/mercurous sulfate electrode (MSE) (Hg/Hg_2SO_4 sat'd K_2SO_4, E = 0.64 V vs. NHE) and the counter electrode was a Pt wire or mesh. Most electrochemical measurements were carried out using a solution consisting of 1.0 mM FcMeOH and 0.10 M KNO_3. For electrochemical experiments using a MUA SAM-coated working electrode, solutions containing either 1.0 mM $Ru(NH_3)_6^{3+}$ and 0.10 M KNO_3 or 1.0 mM $Fe(CN)_6^{3-}$ and 0.10 M KNO_3 were used. In some cases, data were smoothed using a 5-point moving average to reduce noise.

Finite Element Simulations. Finite element simulations were performed using a Dell Precision T7500 workstation equipped with Dual Six Core Intel Xeon Processors (2.40 GHz) and 24 GB of RAM. Simulations were performed using the COMSOL Multiphysics v4.3b commercial package. All simulations were performed using a 2D geometry. The simulation geometry was made of a rectangle 360 μm (h) x 1 mm (w) with a circle representing the wire electrode placed in the center of the channel and subtracted from the geometry (Figures 8.2 and 8.3) The geometry was then cut in half along the vertical axis of symmetry to reduce computation time. An extremely fine mesh was placed over the electrode surface such that the maximum element size was 50 nm.

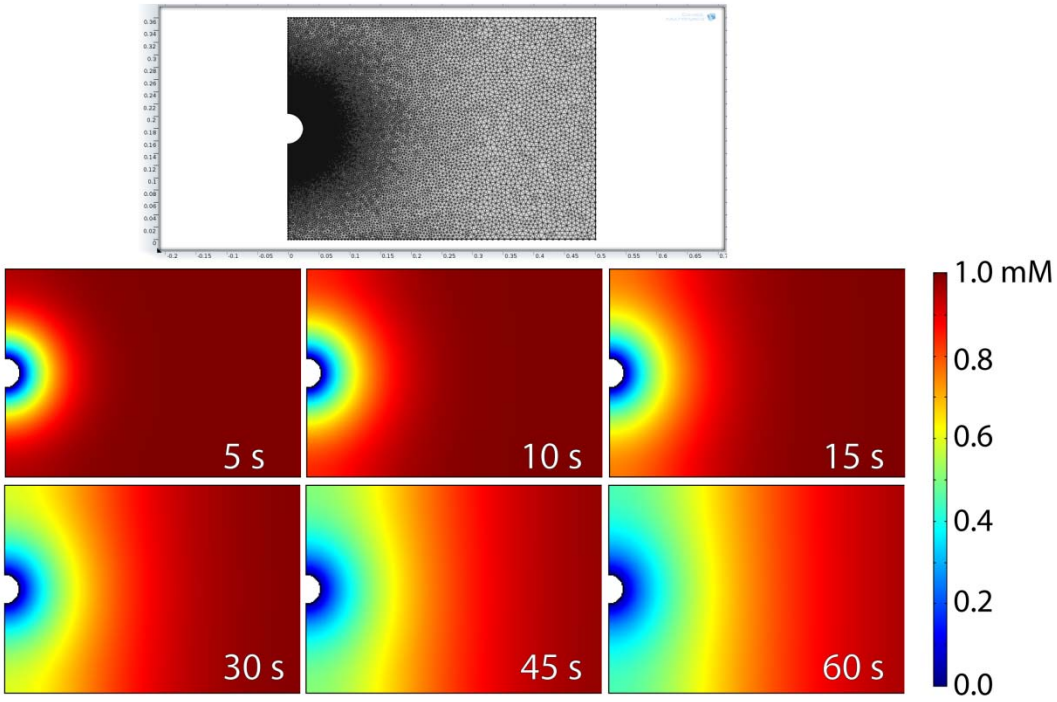

Figure 8.2. Finite element simulation of a single potential step experiment obtained using a 51.3 µm electrode. The top frame is an image of the simulation geometry and mesh (360 µm tall, 500 µm wide, wire placed at center of height of channel, and the left edge representing a plane of symmetry). The remaining frames show the concentration profiles of the redox probe at the indicated times during the potential step. Note that the diffusion profile of the redox active species begins to reach the top and bottom walls of the simulation in ~10 s, breaking the symmetry of the 1D semi-infinite mass transport of the redox probe to the wire. Note that uncompensated resistance, present in the experimental measurements, was not taken into account in the simulations.

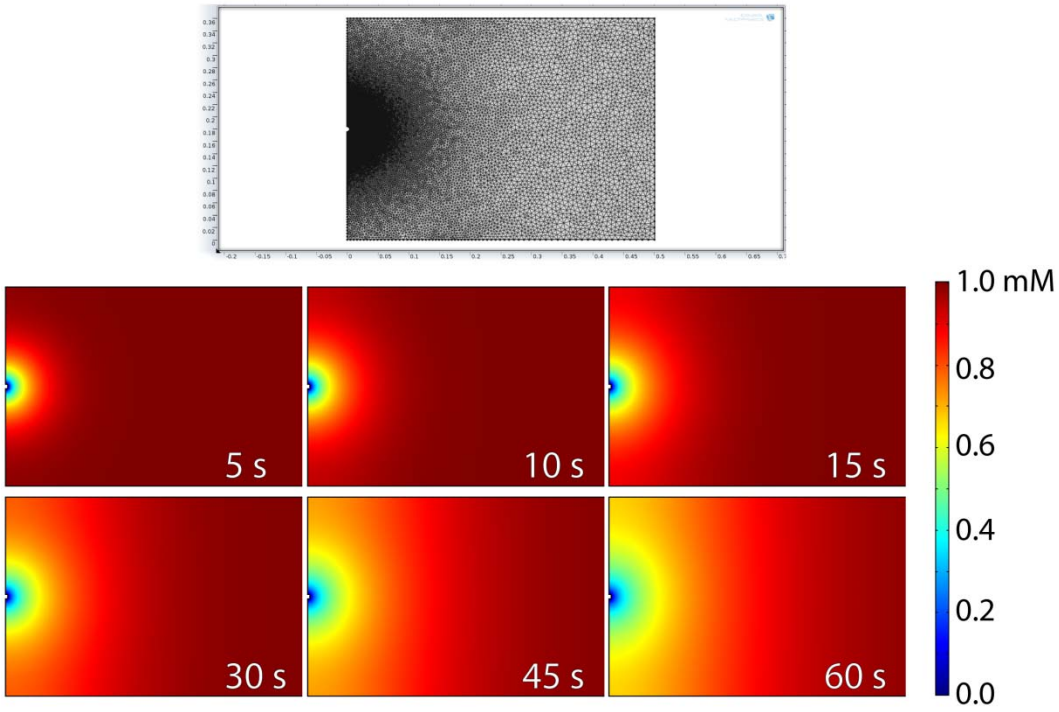

Figure 8.3. Finite element simulation of a single potential step experiment obtained using a 9.95 µm electrode. The top frame is an image of the simulation geometry and mesh (360 µm tall, 500 µm wide, wire placed at center of height of channel, and the left edge representing a plane of symmetry). The remaining frames show the concentration profiles of the redox probe at the indicated times during the potential step. Note that the diffusion profile of the redox active species begins to reach the top and bottom walls of the simulation in ~15 s, breaking the symmetry of the 1D semi-infinite mass transport of the redox probe to the wire. Note that uncompensated resistance, present in the experimental measurements, was not taken into account in the simulations.

A boundary layer mesh, consisting of 8 layers, was also placed over the electrode surface. The total number of mesh elements was 103,760 for the C fiber and 291,704 for Au wire. The largest mesh element in both cases was 10 μm.

Electrochemistry was modeled using the "Transport of Diluted Species" COMSOL module. Both FcMeOH and the oxidized form, ferroceniummethanol, $FcMeOH^+$, were considered for each calculation. The electrochemical reaction of the redox probe is described by eq 8.1.

$$FcMeOH^+ + e^- \leftrightarrow FcMeOH \tag{8.1}$$

The model assumed Butler-Volmer kinetics at the electrode surface.[55] This kinetic model dictates the rates of the forward (reduction) and back (oxidation) reactions based on eqs 8.2 and 8.3.

$$k_F = k^\circ \exp\left[\frac{\alpha F(E - E^\circ)}{RT}\right] \tag{8.2}$$

$$k_B = k^\circ \exp\left[\frac{(1-\alpha)F(E - E^\circ)}{RT}\right] \tag{8.3}$$

Where F is the Faraday constant (96,485 C mol^{-1}), R is the gas constant (8.314 J mol^{-1} K^{-1}), T is the temperature (298.15 K), E° is the reduction potential for the redox couple (-0.20 V vs. MSE based on experimental observation), E is the potential of the electrode, k° is the standard kinetic rate constant (0.2 cm s^{-1}),[205] α is the transfer

coefficient (0.5),[205] and k_F and k_B are the forward and backward rates of the reaction at the electrode surface, respectively. Based on these equations, it was possible to set the boundaries of the electrode surface as "Flux Boundaries" such that the flux into the solution domain across the electrode surface (N) are given by eqs 8.4 and 8.5.

$$N_{FcMeOH^+} = k_B c_{FcMeOH} - k_F c_{FcMeOH^+} \quad (8.4)$$

$$N_{FcMeOH} = -N_{FcMeOH^+} = k_F c_{FcMeOH^+} - k_B c_{FcMeOH} \quad (8.5)$$

The floor and the ceiling of the simulation geometry were taken to be no flux boundaries. Boundaries adjacent to the electrode were taken to be symmetry boundaries. The remaining boundary was taken to be a concentration boundary, such that c_{FcMeOH} = 1 mM and $c_{FcMeOH+}$ = 0 mM.

All simulations were performed under no-flow conditions, so the effects of convection and electromigration terms were neglected. Consequently, mass transfer is defined by eq 8.6.

$$N = -D\nabla c \quad (8.6)$$

Transient simulated cyclic voltammograms were obtained by varying the value of E as a function of time, while simulated chronoamperometric traces (i-t) were obtained by fixing E for the entire time window. In each case, the

current at the electrode surface was calculated using eq 8.7.

$$i = 2FWN^{\text{norm}}_{\text{FcMeOH}^+} \quad (8.7)$$

Where W is the channel width (1.3 mm) and $N^{\text{norm}}_{\text{FcMeOH}^+}$ is the normal flux of $FcMeOH^+$ at the electrode surface. A factor of 2 is included to account for the symmetry of the system.

8.4 Results and Discussion

Design and Considerations for Electroanalysis. The general design used in these experiments is illustrated in Scheme 8.1. The device is fabricated using the folding principles of origami to create a multi-layered structure we call an *o*PAD.[191,206] Two types of channels were used: (1) typical paper channels (PCs) filled with cellulose fibers and defined using wax printing;[182,207] and (2) HCs fabricated using a laser cutter to remove a section of cellulose fibers.[204] We have previously shown that HCs have a number of desirable characteristics, including simple fabrication, increased fluid flow, reduced surface area available for non-specific adsorption, and reproducible electrochemical characteristics.[208] As shown in Scheme 8.1, Layer 1 contains an inlet and outlet. Layers 2 & 3 contain two stacked channels, which may be either hollow or filled with cellulose fibers. The bottom layer contains a feature of

similar dimensions to the channels in Layers 2 & 3, but which is partially waxed. We call this type of structure a hemichannel.[204] It consists of a top layer (~70 µm) of cellulose fibers, and a bottom layer (~110 µm) of wax-filled cellulose. Both layers are present within a single ~180 µm-thick section of the constituent paper. The hydrophilic layer of the hemichannels enables capillary flow in HCs.[204,209]

The *o*PAD platform depicted in Scheme 8.1 allows microwires to be placed anywhere within the channels of either a HC or PC device. However, in most cases discussed herein (and unless otherwise stated), the microwires were placed between Layers 2 & 3, as shown in Scheme 8.1a, resulting in a wire suspended at the vertical center of the channel. Wires can also be placed on either the top of the channel (bottom of Layer 1) in a HC-*o*PAD. Additionally, the wire can be placed between two paper channels (Layers 2 & 3) in a PC-*o*PAD.

For electrochemical detection schemes where the analyte is a freely diffusing species, it is advantageous to reach steady-state mass transport conditions, such as radial diffusion to an ultramicroelectrode.[55] This is because the steady state simplifies the relationship between current and concentration of a redox target.[55] Micron-scale wires can achieve a quasi-steady state current response even in

non-flowing solutions. On the other hand, many detection schemes rely on an electrode-immobilized receptor probe, such as single-stranded DNA or an antibody. In this case it may be desirable to use electrodes having higher surface areas than a micron-scale wire can provide. Later we will show that the flexibility of approach described here provides for this need too.

Electrochemistry at Microwire Electrodes. Figure 8.4 shows a series of experimentally obtained CVs (black lines) overlaid onto simulated CVs (red circles). These data were collected using a quiescent electrolyte solution consisting of 1.0 mM FcMeOH and 0.10 M KNO_3, and scan rates (v) of 10, 50, and 100 mV/s. For this data set the working electrode was a 51.3 μm-diameter Au wire stretched across Layer 3 of a HC *o*PAD (Scheme 8.1) and placed 5 mm from the outlet reservoir. Because there is a HC above and below the wire, this results in the electrode being configured at the vertical center of the channel.

The CVs in Figure 8.4 are typical of a reversible redox couple subject to scan-rate-dependent mass transfer conditions at a cylindrical microelectrode.[194,210] That is, at a scan rate of 100 mV/s, the peak-shaped voltammogram is qualitatively characteristic of linear diffusion, but as the

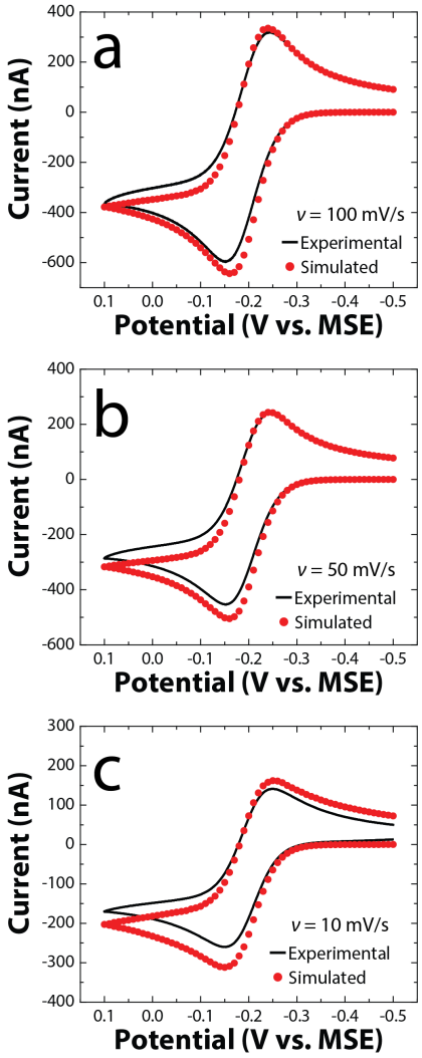

Figure 8.4. CVs of a 1.0 mM FcMeOH solution obtained using a 51.3 µm diameter Au wire working electrode in a HC-*o*PAD, like that depicted in Scheme 8.1, at scan rates between 10 and 100 mV/s. The black lines show the experimental results and the filled red circles are the results of finite element simulations. The Au wire was situated 5 mm from the outlet of the channel and was placed between Layers 2 and 3 of the device. This results in a configuration where the microwire electrode is suspended at the half height (vertical center) of the channel. The supporting electrolyte was 0.10 M KNO_3.

scan rate is lowered, the peak-shaped feature flattens and starts to become more characteristic of radial diffusion.

To better understand the voltammetric response of the device shown in Figure 8.4, we carried out finite element simulations (FES, red circles). While analytical solutions of the current response at microwire electrodes have been presented,[210,211] the unique geometry of the *o*PAD, such as the impact of the top and bottom of the channel on resulting concentration profiles, necessitates consideration of the location of the electrode in the device. As seen in Figure 8.4, the shapes of the experimental and simulated results have the same general characteristics, and the current magnitudes are in semi-quantitative agreement with one-another. For example, differences in the anodic peak currents ($i_{p,a}$) are typically within 7-16% depending on the scan rate. This variation is on the same order as the device-to-device variation in $i_{p,a}$ observed for nominally identical *o*PADs and experimental conditions (~10%, Figure 8.5). One significant difference between the experimental and simulated CVs relates to the uncompensated resistance (R_u) present in the *o*PAD. The experimental data in Figure 8.4 were not corrected for R_u, which has a measured value of 6.3 ± 0.2 kΩ. R_u results in a larger peak splitting (ΔE_p =

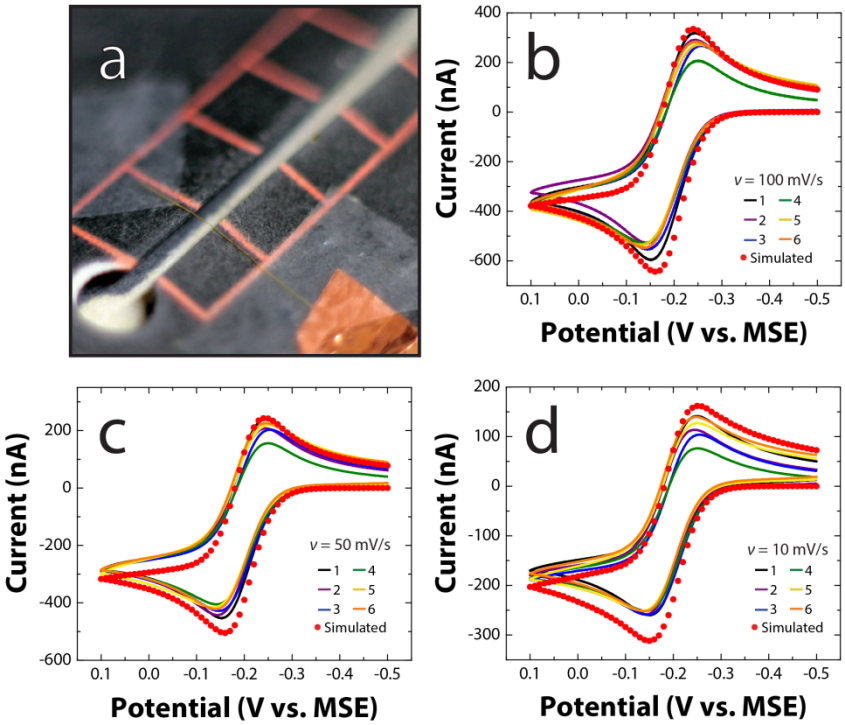

Figure 8.5. Results illustrating the reproducibility of the electrochemical response of independently fabricated hollow channel *o*PADs. (a) Photograph of a hollow channel *o*PAD having a 51.3 μm Au wire working electrode placed on the top of Layer 3. The photograph was obtained after the device had been used to obtain the data in Frames b-d. The hemichannel (white paper channel) on Layer 4 is visible at the bottom of the inlet. The pink lines are alignment features for folding and wire placement. The reference (MSE) and counter electrodes (Pt wire) were placed in the outlet reservoir. (b-d) CVs as a function of scan rate obtained using six independently fabricated devices like the one shown in (a). The colored lines show the response of each device and the red circles show the results of finite element simulations.

R_u results in a larger peak splitting (ΔE_p = 90-100 mV, depending upon scan rate) than is observed in the simulations (ΔE_p = 78-90 mV).

Figure 8.6 shows a series of CVs obtained at different scan rates using a 9.95 µm C fiber working electrode. In all other respects, the conditions are the same as those used to obtain the data in Figure 8.4. In this case, however, the simulated and experimental results are in better agreement (<6% difference) than for the larger Au wire electrode. This might be a consequence of the C fiber being more rigid than the Au wire, which can deform or bend during assembly of the *o*PAD. Additionally, because of the smaller radial dimension, the voltammetry at the C fiber electrodes exhibits less contribution from linear diffusion than does the larger Au wire. Accordingly, one advantage of the C fiber over the Au wire is that the smaller radial dimension leads to shorter time requirements for entering the quasi-steady state mass transfer regime. Examples of chronoamperometric experiments collected in HC-PADs with Au wire and C fiber can be found in Figure 8.7.

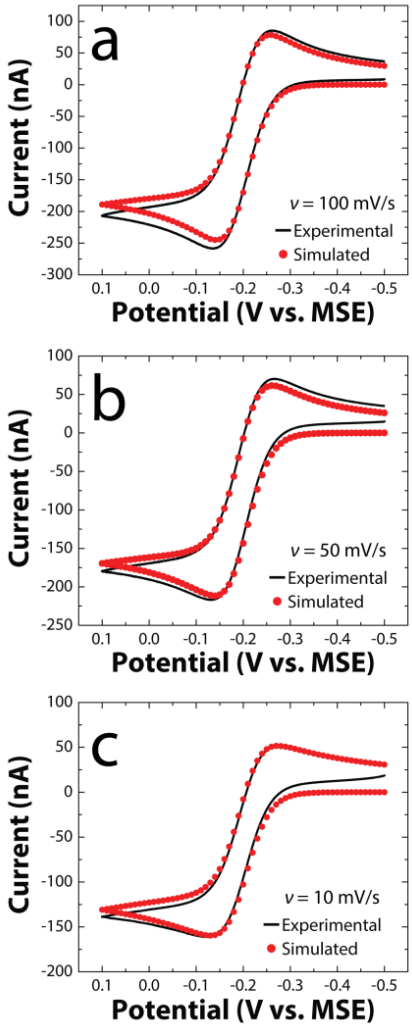

Figure 8.6. CVs of a 1.0 mM FcMeOH solution obtained using a 9.95 µm diameter C fiber working electrode in a HC-*o*PAD, like that depicted in Scheme 8.1, at scan rates between 10 and 100 mV/s. The black lines show the experimental results and the red circles show the results of finite element simulations. The C fiber was situated 5 mm from the outlet of the channel and was placed between Layers 2 & 3 of the device. This results in a configuration where the microwire electrode is suspended at the half height (vertical center) of the channel. The supporting electrolyte was 0.10 M KNO_3.

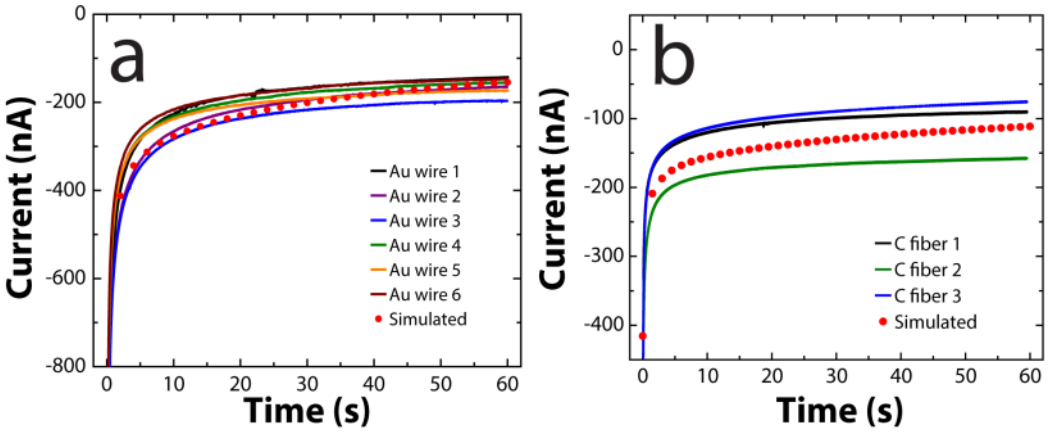

Figure 8.7. (a) Chronoamperometry collected using 6 individually fabricated hollow channel *o*PADs having a 51.3 µm Au wire working electrode. The experimental results (colored lines) can be compared directly to the simulated results (red circles). The average quasi-steady-state current (i_{qss}) at t = 15 s was -220 ± 20 nA, at t = 30 s i_{qss} was -186 ± 19 nA, and at t = 60 s i_{qss} was -163 ± 20 nA, indicating ~±11% variation for the 6 independently fabricated devices. The simulated values of i_{qss} at these times are -250, -201, and -155 nA, respectively. The differences between the average experimental values and the simulated results are 12%, 8%, and 6%, respectively. (b) Chronoamperometry collected from 3 individually fabricated hollow channel *o*PADs having a 9.95 µm C fiber working electrode. The experimental results (colored lines) can be compared directly to simulated results (red circles). The i_{qss} at t = 15 s was -130 ± 40 nA, at t = 30 s i_{qss} was -120 ± 40 nA, and at t = 60 s i_{qss} was -110 ± 40 nA, indicating ~±33% variation between the 3 devices. The simulated values of i_{qss} at these times are -147, -130, and -111 nA, respectively. The differences between these average values and the simulated results are 11%, 9%, and 3%, respectively. In all cases, the electrolyte solution contained 1.0 mM FcMeOH and 0.10 M KNO_3, the reference electrode (MSE) and the counter electrode (Pt wire) were placed in the outlet reservoir, and the potential of the working electrode was stepped from -0.50 V vs. MSE to 0.10 V vs. MSE for 60 s.

Modification of Au wire with SAMs. One important advantage of using wires as electrodes in PADs, rather than screen-printed electrodes, is that the former can be surface modified, for example with a bioreceptor, just prior to device assembly. This means that cleaning procedures that would destroy the paper or the hydrophobic wax support (e.g., piranha cleaning, ethanol washes) can be carried out. An additional advantage of wires over screen-printed electrodes is that a long length of wire can be modified simultaneously, and subsequently cut into pieces and inserted into the *o*PAD. Finally, because paper swells in water and because water penetrates wax on a time scale of tens of minutes,[208] long electrode modification times are impractical for screen-printed electrodes on paper. Figure 8.8 provides an example of some of the advantages alluded to in the previous paragraph. Figure 8.8a shows 20 consecutive CVs obtained at a scan rate of 100 mV/s and using a Au wire working electrode that was piranha-cleaned and then exposed to an ethanolic solution containing 1.0 mM 11-(ferrocenyl)undecanethiol and 1.0 mM mercaptohexane for 1 h prior to being configured in the *o*PAD along with a 0.10 M KNO_3 electrolyte solution. Clearly the scan-to-scan variability is small and consistent with published results obtained in more traditional electrochemical cells.[212-215] Figure 8.8b shows the voltammetric response of the same

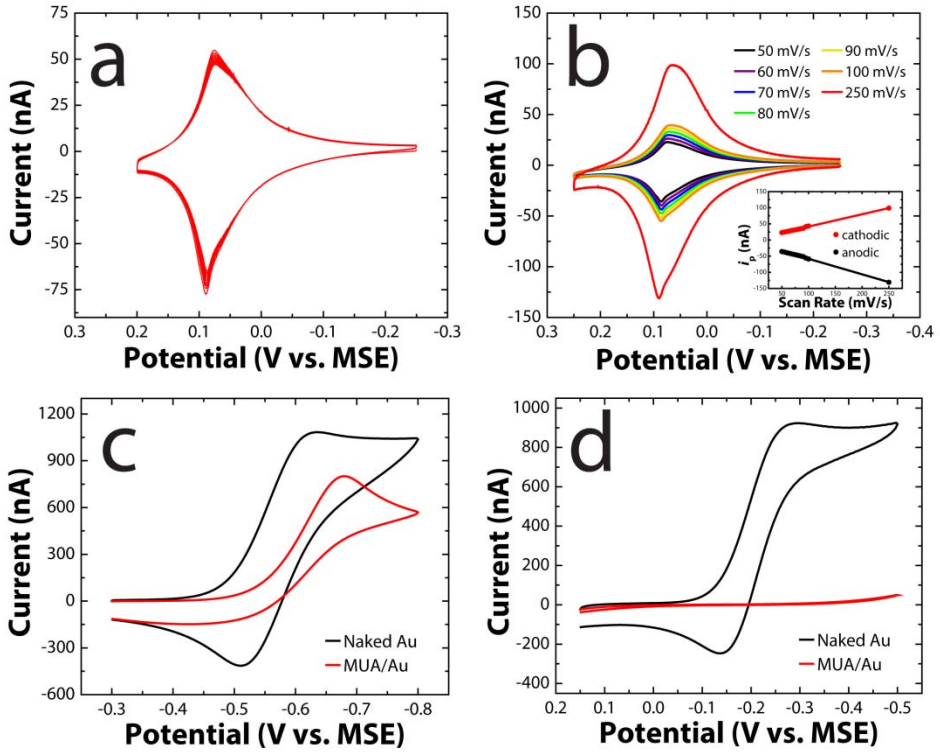

Figure 8.8. (a) Twenty consecutive CVs obtained using a 51.3 µm Au wire electrode co-modified with 11-(ferrocenyl) undecanethiol and mercaptohexane at a scan rate of 100 mV/s. (b) CVs of the SAM in (a) at scan rates ranging between 50 and 250 mV/s. The inset is a plot of $i_{p,a}$ and $i_{p,c}$ vs. scan rate. (c) CVs obtained using a naked 51.3 µm Au wire (black) and a Au wire modified with a MUA SAM (red) in a solution containing 1.0 mM $Ru(NH_3)_6^{3+}$ and 0.10 M KNO_3 at a scan rate of 100 mV/s. (d) CVs obtained using a naked Au wire (black) and a Au wire modified with a MUA SAM (red) in a solution containing 1.0 mM $Fe(CN)_6^{3-}$ and 0.10 M KNO_3 at a scan rate of 100 mV/s.

electrode, but at scan rates ranging from 50-250 mV/s. Because the film is immobilized on the electrode, the magnitude of the peak currents should vary linearly with scan rate.[55] The inset of Figure 8.8b shows that this behavior is observed for the electroactive SAM for both the anodic and cathodic peaks.

The wire electrodes can also be modified with SAMs that selectively block particular redox couples. For instance, when a thiolated SAM having a distal carboxylic acid group is immobilized on a Au electrode and the pH of the electrolyte solution is above the pK_a of the acid, then a negatively charged interface develops. This negative charge can then interact electrostatically with diffusing redox species and either promote or suppress their ability to undergo electron transfer.

Figure 8.8c shows CVs of the reduction of $Ru(NH_3)_6^{3+}$ at a naked Au wire (black) and one modified with an acid-terminated MUA SAM (red). The naked Au wire exhibits current due to simultaneous reduction of both oxygen (at potentials negative of about -0.5 V vs. MSE) and $Ru(NH_3)_6^{3+}$. The MUA SAM results in three major changes to the voltammetry of the $Ru(NH_3)_6^{3+}$ at the Au wire electrode: (1) the background current due to oxygen reduction is suppressed, (2) $Ru(NH_3)_6^{3+}$ reduction is shifted to more negative potentials, and (3) the re-oxidation of electroreduced $Ru(NH_3)_6^{2+}$ is suppressed.

The decrease in current contributions from oxygen reduction and the shift to slightly more negative potentials for $Ru(NH_3)_6^{3+}$ reduction are a consequence of the SAM blocking the Au surface, the increased resistance of electron tunneling through the SAM, and the change in the interfacial potential induced by the charged terminus of the SAM.[216,217] The apparent quasi-reversible or irreversible voltammetric behavior has been previously observed with oppositely charged SAM/redox probe systems.[216,218-221] The effect may be due in part to the effective interfacial potential difference caused by the charged SAM as well as the effect of the SAM on the distribution of ions at the interface.

Figure 8.8d shows CVs obtained at a naked Au wire electrode (black) and a Au wire modified with a MUA SAM (red) in a solution containing 1.0 mM $Fe(CN)_6^{3-}$ and 0.10 M KNO_3. In contrast to the response of the $Ru(NH_3)_6^{3+}$ solution, where the redox probe is a positively charged species, $Fe(CN)_6^{3-}$ is negatively charged and the electrostatic interaction between the MUA SAM and $Fe(CN)_6^{3-}$ prevents significant electron transfer.[216,222,223] Therefore, the voltammetric response of the electrode exhibits very little faradaic current (<0.6% of the peak current of the naked Au wire). The electrochemical results obtained using these modified Au electrodes demonstrate the likely utility of wire electrodes in future PAD-based sensors.

Fully Integrated Device. Because electrochemical PADs are intended primarily for POC applications, it is important that they be functional in a fully integrated format. The results discussed in this section demonstrate that all three electrodes required for voltammetry can be placed within a hollow channel, and that the electrochemical results are nearly identical to those obtained when the reference and counter electrodes are situated outside of the device.

Figure 8.9a shows a picture of a HC-*o*PAD incorporating 3 electrodes: a Au microwire working electrode, a SPCE coated with Ag/AgCl paste serving as a reference electrode, and a SPCE counter electrode. This device was tested in 1.0 mM FcMeOH containing 0.10 M KNO_3. The resulting voltammetry, shown in Figure 8.9b, is very similar to the results obtained when the reference and counter electrode are placed in the outlet reservoir of the device. The levels of R_u are also comparable: 6-10 kΩ.

Figure 8.9c compares amperometric *i*-*t* curves collected using 4 independently fabricated, fully integrated devices with simulated results. The average quasi-steady state currents (i_{qss}) for these 4 devices at 30 s and 60 s were -178 ± 18 nA and -154 ± 13 nA, respectively. The corresponding simulated values of i_{qss} at 30 s and 60 s are -201 nA and -154 nA, respectively.

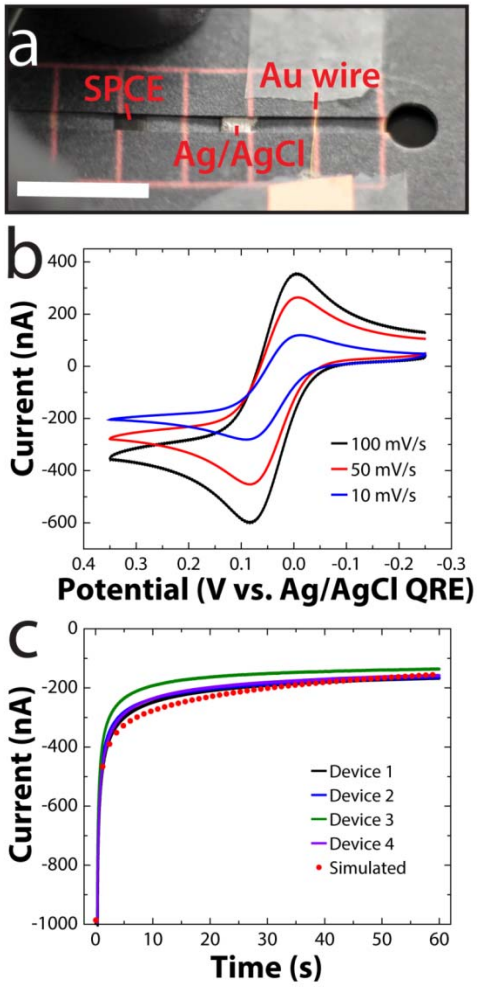

Figure 8.9. (a) Photograph of a fully integrated *o*PAD wherein the working electrode is a 51.3 µm Au wire, the reference electrode is a SPCE coated with Ag/AgCl paste, and the counter electrode is a SPCE. The pink lines are alignment marks used to accurately fold the device and to achieve reproducible electrode placement. The white scale bar indicates 1.00 cm. (b) CVs of 1.0 mM FcMeOH obtained using the *o*PAD shown in (a) at scan rates between 10 and 100 mV/s. The electrolyte was 0.10 M KNO_3. (c) Chronoamperometry of 1.0 mM FcMeOH using four independently fabricated *o*PADs like that shown in (a). The potential of the Au wire working electrode was stepped from -0.25 V to 0.35 V vs. Ag/AgCl QRE for 60 s. The corresponding finite element simulation is also shown (filled red circles). In all cases the electrolyte was 0.10 M KNO_3.

The key point is that the function of the *o*PAD is independent of the location of the three electrodes regardless of the electrochemical method (voltammetry or amperometry) employed.

Additional Electrode Configurations. The platform design shown in Scheme 8.1 provides a flexible means for positioning working electrodes in configurations other than those described thus far. For example, Figure 8.10 provides a photograph of an *o*PAD in which the Au wire working electrode is placed at the top of a hollow channel (bottom side of Layer 1) instead of at the half height (between Layers 2 & 3). The resulting voltammetry is reproducible and consistent with expectations. Figure 8.11 shows that both Au wire and C fiber electrodes are also fully functional when incorporated into cellulose-filled paper channels. Finally, Figure 8.12 demonstrates that a Au mesh electrode can also be integrated into HC-*o*PAD devices. This type of electrode provides additional surface area, compared to a single wire, and hence could be useful for immobilization of bioprobes, such as DNA or antibodies.

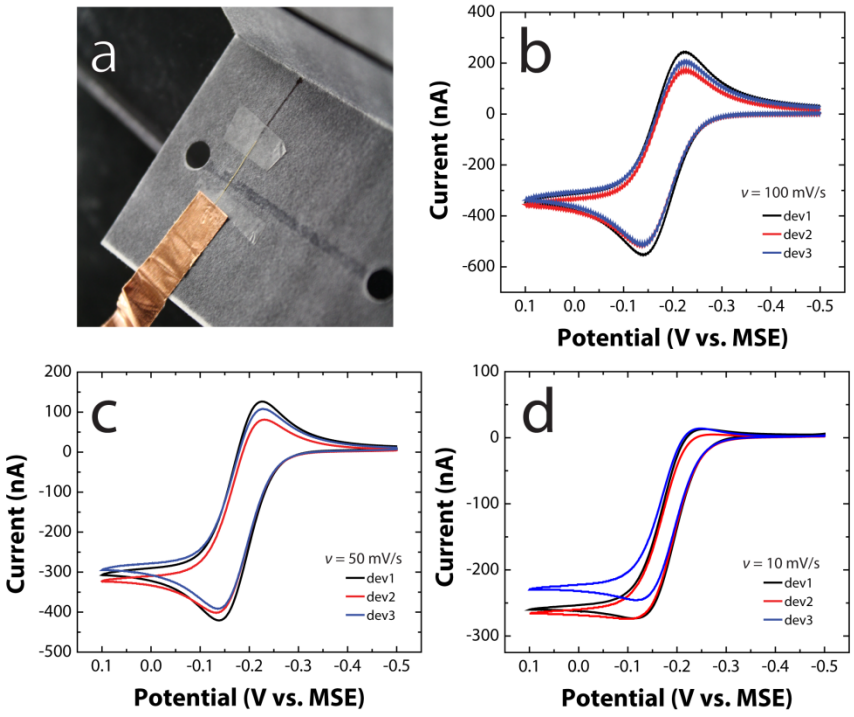

Figure 8.10. (a) Photograph of a HC-*o*PAD where the Au wire is placed on the bottom of Layer 1 instead of between Layers 3 and 4. (b-d) CVs obtained using three independently fabricated *o*PADs like that shown in (a). The scan rates are indicated in the individual frames. The solution contained 1.0 mM FcMeOH in 0.10 M KNO_3. At v = 100 mV/s, $i_{p,a}$ and $i_{p,c}$ varied by ±4.3% and ±5.1%. At v = 50 mV/s $i_{p,a}$ and $i_{p,c}$ varied by ±3.9% and ±3.8%, respectively. The variation at v = 10 mV/s was more substantial, the shape of the CVs somewhat different, possibly due to a small amount of unintentionally added flow. The reference electrode was a MSE and the counter electrode was a Pt wire. The reference and counter electrodes were placed in the outlet reservoir.

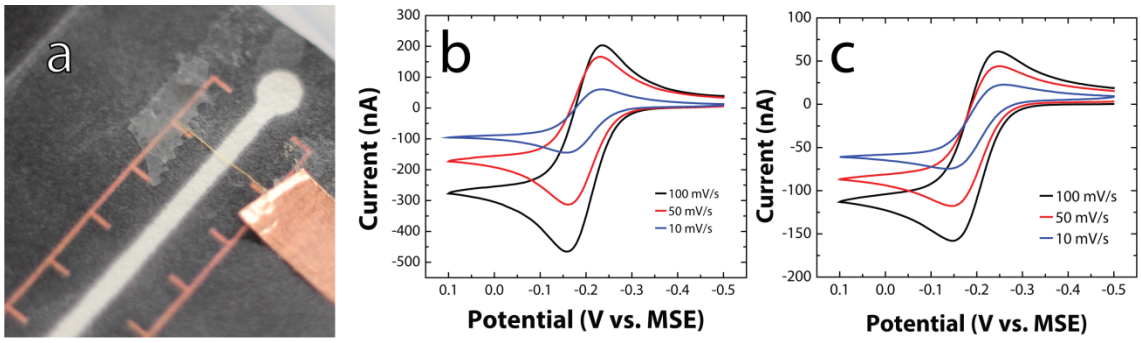

Figure 8.11. (a) Photograph of an *o*PAD having a cellulose-filled paper channel (i.e., not a hollow channel). The working electrode was placed in contact with the paper channel on top of Layer 3. The reference (MSE) and counter electrodes (Pt wire) were placed in the outlet reservoir. (b and c) CVs of 1.0 mM FcMeOH as a function of scan rate using the *o*PAD shown in (a). In (b) the working electrode was a 51.3 µm Au wire and in (c) it was a 9.95 µm C fiber. The pink lines in (a) are alignment features for folding and wire placement.

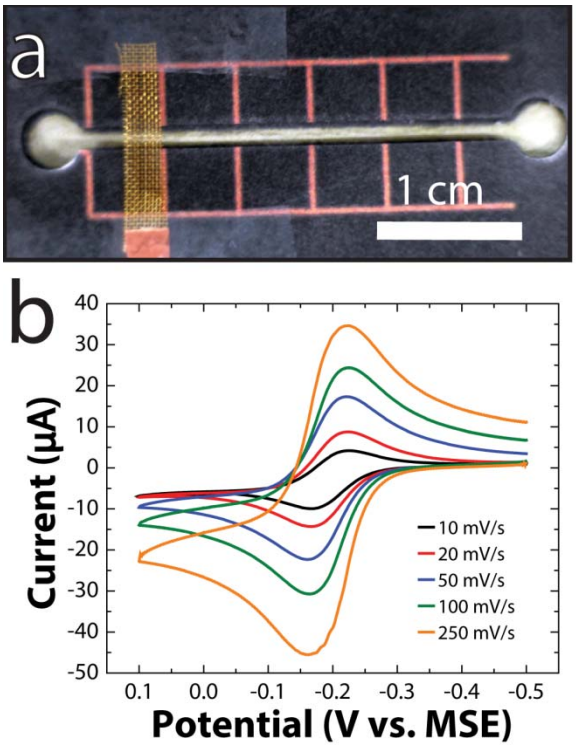

Figure 8.12. (a) Photograph of a HC-*o*PAD employing a Au mesh working electrode (100 mesh, 2 mm long and spanning the full width (1.3 mm) of the hollow channel). (b) CVs collected at different scan rates using the Au mesh electrode. The solution contained 1.0 mM FcMeOH and 0.10 M KNO_3. The resistance of the electrochemical cell was compensated at a level of 7.2 kΩ. The reference electrode (MSE) and the counter electrode (Pt mesh) were placed in the outlet reservoir.

8.5 Summary and Conclusions

In this chapter we have shown that Au microwires and meshes, as well as C fibers, can be used as working electrodes within paper-based electroanalytical devices. The voltammetric responses of these electrodes are consistent with finite element simulations, and hence their behavior is easily predictable, even when reference and counter electrodes are integrated within the paper platform. Mesh electrodes provide higher surface areas than wires, and could be useful for applications requiring higher surface areas for immobilization of bioprobes. Although this report has focused on just Au and C electrodes, there is no obvious barrier to using other common electrode materials such as Pt or even Hg-thin film electrodes.

Heretofore, most working electrodes in PADs have been based on carbon inks, but, depending on the application wires, fibers, and meshes may provide some distinct advantages. For example, they can be more easily cleaned and modified and may well be easier to integrate than screen- or stencil-printed electrodes.

Chapter 9: Summary and Conclusions

This dissertation describes the development of an electrocatalyst screening platform based on bipolar electrochemistry. The platform began as a simple proof of concept and was extended and scaled up to evaluate many different electrocatalyst candidate compositions. Other advances presented here include the development of an electrode array from a single substrate based on localizing faradaic reactions, the optical tracking of the interactions of insulating particles with an ultramicroelectrode, and the development of wire, mesh, and fiber electrodes for paper-based electrochemical devices.

Chapter 3 describes the initial proof of concept experiment where model nanoparticle systems were deposited onto the cathodic poles of an array of BPEs and their relative effectiveness for driving the ORR was evaluated based on the dissolution of Ag microbands. The number of Ag microbands that dissolved over the course of the experiment was directly related to the onset potentials of the ORR measured from traditional 3-electrode electrochemical experiments.

Chapter 4 describes how the general experimental scheme presented in Chapter 3 could be expanded to test combinatorial libraries of electrocatalyst candidates for

the ORR by making several key modifications to the experimental design: (1) replacing Ag with Cr, (2) scaling up the size of the array, and (3) adopting piezodispensing as a technique to prepare materials with varied compositions. Several Pd-M (M = Au, Co, W) were evaluated and several Pd-Co species were identified as being more active than pure Pd.

Chapter 5 describes the continued extension of the BPE screening platform to non-noble metal electrocatalyst candidates for the HER. This required several additional modifications to the system such as a plastic purging box, more precise control of the timing of the experiments, and direct measurement of key experimental parameters *in situ*. Furthermore, the system was expanded to evaluate trimetallic systems, requiring a denser electrode array. Non-noble metal compositions consisting of Co, Fe, Mo, Ni, and W were tested. The bimetallic system of Ni-Mo was found to be the most promising and was tested in a 3-electrode configuration.

Chapter 6 describes a technique for localizing faradaic reactions at different locations on a single conductive substrate. This was achieved by manipulating two orthogonally applied potential biases in a cross-channel microfluidic space. By controlling the relative magnitudes of the two biases, reactions can be made to move around the

perimeter of the BPE. This was followed by using a light-generating electrochemical reaction, such as ECL.

Chapter 7 describes a technique for optically tracking the interactions between insulating microbeads and an active ultramicroelectrode. The microbeads were fluorescently labeled, which allowed direct fluorescence imaging of the particles interacting with the electrode surface. The intensity of the resulting signal coming from the collision of the particles with the electrode surface was shown to be strongly related to where the particle reached the surface. Also, several previously predicted bead movements on the surface of the electrode and the collision of bead aggregates where directly confirmed using fluorescence microscopy.

Chapter 8 describes the incorporation of wires, fibers, and meshes with dimensions on the micron to tens of micron scales into paper-based analytical devices. The use of the electrode materials has a number of key advantages over traditional screen- or stencil-printed carbon electrodes: (1) ability to select electrode material based on analysis requirements, (2) increased mass transport from non-linear diffusion, (3) easily configurable placement within devices, and (4) ease of cleaning and modification exterior to the device.

References

1. Backhurst, J. R.; Coulson, J. M.; Goodridge, F.; Plimley, R. E.; Fleischmann, M. A Preliminary Investigation of Fluidized Bed Electrodes. *J. Electrochem. Soc.* **1969**, *116*, 1600-1607.
2. Fleischmann, M.; Oldfield, J. W. Fluidized bed electrodes. I. Polarization predicted by simplified models. *J. Electroanal. Chem. Interfacial Electrochem.* **1971**, *29*, 211-30.
3. Goodridge, F.; King, C. J. H.; Wright, A. R. The behaviour of bipolar packed-bed electrodes. *Electrochim. Acta* **1977**, *22*, 347-352.
4. Goodridge, F.; King, C. J. H.; Wright, A. R. Performance Studies on a Bipolar Fluidized-Bed Electrode. *Electrochim. Acta* **1977**, *22*, 1087-1091.
5. Plimley, R. E.; Wright, A. R. A Bipolar Mechanism for Charge-Transfer in a Fluidized-Bed Electrode. *Chem. Eng. Sci.* **1984**, *39*, 395-405.
6. Fleischmann, M.; Ghoroghchian, J.; Rolison, D.; Pons, S. Electrochemical behavior of dispersions of spherical ultramicroelectrodes. *J. Phys. Chem.* **1986**, *90*, 6392-6400.
7. Ellis, K. G.; Jansson, R. E. W. Further studies on the epoxidation of propylene in a bipolar trickle bed. *J. Appl. Electrochem.* **1981**, *11*, 531-535.
8. Manji, A.; Oloman, C. W. Electrosynthesis of propylene oxide in a bipolar trickle-bed reactor. *J. Appl. Electrochem.* **1987**, *17*, 532-544.
9. Lee, J. K.; Shemilt, L. W.; Chun, H. S. Studies of bipolarity in fluidized bed electrodes. *J. Appl. Electrochem.* **1989**, *19*, 877-881.
10. Smotkin, E.; Bard, A. J.; Campion, A.; Fox, M. A.; Mallouk, T.; Webber, S. E.; White, J. M. Bipolar titanium dioxide/platinum semiconductor photoelectrodes and multielectrode arrays for unassisted photolytic water splitting. *J. Phys. Chem.* **1986**, *90*, 4604-4607.
11. Cervera-March, S.; Smotkin, E. S.; Bard, A. J.; Campion, A.; Fox, M. A.; Mallouk, T.; Webber, S. E.; White, J. M. Modeling of Bipolar Semiconductor Photoelectrode Arrays for Electrolytic Processes. *J. Electrochem. Soc.* **1988**, *135*, 567-573.

12. Wiesener, K.; Ohms, D.; Benczúr-Ürmössy, G.; Berthold, M.; Haschka, F. High power metal hydride bipolar battery. *J. Power Sources* **1999**, *84*, 248-258.
13. Steele, B. C. H.; Heinzel, A. Materials for fuel-cell technologies. *Nature* **2001**, *414*, 345-352.
14. Hermann, A.; Chaudhuri, T.; Spagnol, P. Bipolar plates for PEM fuel cells: A review. *Int. J. Hydrogen Energy* **2005**, *30*, 1297-1302.
15. Amatore, C.; Brown, A. R.; Thouin, L.; Warkocz, J.-S. Mimicking neuronal synaptic behavior: Processing of information with 'AND' or 'OR' Boolean logic via paired-band microelectrode assemblies. *C.R. Acad. Sci., Ser. IIc: Chim.* **1998**, *1*, 509-515.
16. Chow, K.-F.; Mavré, F.; Crooks, J. A.; Chang, B.-Y.; Crooks, R. M. A Large-Scale, Wireless Electrochemical Bipolar Electrode Microarray. *J. Am. Chem. Soc.* **2009**, *131*, 8364-8365.
17. Paxton, W. F.; Kistler, K. C.; Olmeda, C. C.; Sen, A.; St. Angelo, S. K.; Cao, Y.; Mallouk, T. E.; Lammert, P. E.; Crespi, V. H. Catalytic Nanomotors: Autonomous Movement of Striped Nanorods. *J. Am. Chem. Soc.* **2004**, *126*, 13424-13431.
18. Kline, T. R.; Paxton, W. F.; Mallouk, T. E.; Sen, A. Catalytic nanomotors: Remote-controlled autonomous movement of striped metallic nanorods. *Angew. Chem., Int. Ed.* **2005**, *44*, 744-746.
19. Wang, J.; Manesh, K. M. Motion Control at the Nanoscale. *Small* **2010**, *6*, 338-345.
20. Sengupta, S.; Ibele, M. E.; Sen, A. Fantastic Voyage: Designing Self-Powered Nanorobots. *Angew. Chem., Int. Ed.* **2012**, *51*, 8434-8445.
21. Loget, G.; Kuhn, A. Electric field-induced chemical locomotion of conducting objects. *Nat. Commun.* **2011**, *2*.
22. Loget, G.; Kuhn, A. Bipolar electrochemistry for cargo-lifting in fluid channels. *Lab Chip* **2012**, *12*, 1967-71.
23. Sentic, M.; Loget, G.; Manojlovic, D.; Kuhn, A.; Sojic, N. Light-Emitting Electrochemical "Swimmers". *Angew. Chem., Int. Ed.* **2012**, *51*, 11284-11288.
24. Inagi, S.; Ishiguro, Y.; Atobe, M.; Fuchigami, T. Bipolar Patterning of Conducting Polymers by Electrochemical Doping and Reaction. *Angew. Chem., Int. Ed.* **2010**, *49*, 10136-10139.

25. Ishiguro, Y.; Inagi, S.; Fuchigami, T. Gradient Doping of Conducting Polymer Films by Means of Bipolar Electrochemistry. *Langmuir* **2011**, *27*, 7158-7162.
26. Laws, D. R.; Hlushkou, D.; Perdue, R. K.; Tallarek, U.; Crooks, R. M. Bipolar Electrode Focusing: Simultaneous Concentration Enrichment and Separation in a Microfluidic Channel Containing a Bipolar Electrode. *Anal. Chem.* **2009**, *81*, 8923-8929.
27. Perdue, R. K.; Laws, D. R.; Hlushkou, D.; Tallarek, U.; Crooks, R. M. Bipolar Electrode Focusing: The Effect of Current and Electric Field on Concentration Enrichment. *Anal. Chem.* **2009**, *81*, 10149-10155.
28. Anand, R. K.; Sheridan, E.; Hlushkou, D.; Tallarek, U.; Crooks, R. M. Bipolar electrode focusing: tuning the electric field gradient. *Lab Chip* **2011**, *11*, 518-527.
29. Anand, R. K.; Sheridan, E.; Knust, K. N.; Crooks, R. M. Bipolar Electrode Focusing: Faradaic Ion Concentration Polarization. *Anal. Chem.* **2011**, *83*, 2351-2358.
30. Sheridan, E.; Knust, K. N.; Crooks, R. M. Bipolar electrode depletion: membraneless filtration of charged species using an electrogenerated electric field gradient. *Analyst* **2011**, *136*, 4134-4137.
31. Knust, K. N.; Sheridan, E.; Anand, R. K.; Crooks, R. M. Dual-channel bipolar electrode focusing: simultaneous separation and enrichment of both anions and cations. *Lab Chip* **2012**, *12*, 4107-4114.
32. Scida, K.; Sheridan, E.; Crooks, R. M. Electrochemically-gated delivery of analyte bands in microfluidic devices using bipolar electrodes. *Lab Chip* **2012**.
33. Sheridan, E.; Hlushkou, D.; Knust, K. N.; Tallarek, U.; Crooks, R. M. Enrichment of Cations via Bipolar Electrode Focusing. *Anal. Chem.* **2012**, *84*, 7393-7399.
34. Knust, K. N.; Hlushkou, D.; Anand, R. K.; Tallarek, U.; Crooks, R. M. Electrochemically Mediated Seawater Desalination. *Angew. Chem., Int. Ed.* **2013**, *52*, 8107-8110.
35. Zhan, W.; Alvarez, J.; Crooks, R. M. Electrochemical sensing in microfluidic systems using electrogenerated chemiluminescence as a photonic reporter of redox reactions. *J. Am. Chem. Soc.* **2002**, *124*, 13265-13270.
36. Chow, K.-F.; Mavré, F.; Crooks, R. M. Wireless electrochemical DNA microarray sensor. *J. Am. Chem. Soc.* **2008**, *130*, 7544-7545.

37. Mavré, F.; Chow, K.-F.; Sheridan, E.; Chang, B.-Y.; Crooks, J. A.; Crooks, R. M. A Theoretical and Experimental Framework for Understanding Electrogenerated Chemiluminescence (ECL) Emission at Bipolar Electrodes. *Anal. Chem.* **2009**, *81*, 6218-6225.
38. Chang, B.-Y.; Crooks, J. A.; Chow, K.-F.; Mavré, F.; Crooks, R. M. Design and Operation of Microelectrochemical Gates and Integrated Circuits. *J. Am. Chem. Soc.* **2010**, *132*, 15404-15409.
39. Chow, K.-F.; Chang, B.-Y.; Zaccheo, B. A.; Mavré, F.; Crooks, R. M. A Sensing Platform Based on Electrodissolution of a Ag Bipolar Electrode. *J. Am. Chem. Soc.* **2010**, *132*, 9228-9229.
40. Chang, B.-Y.; Mavré, F.; Chow, K.-F.; Crooks, J. A.; Crooks, R. M. Snapshot Voltammetry Using a Triangular Bipolar Microelectrode. *Anal. Chem.* **2010**, *82*, 5317-5322.
41. Fosdick, S. E.; Crooks, J. A.; Chang, B.-Y.; Crooks, R. M. Two-Dimensional Bipolar Electrochemistry. *J. Am. Chem. Soc.* **2010**, *132*, 9226-9227.
42. Dumitrescu, I.; Anand, R. K.; Fosdick, S. E.; Crooks, R. M. Pressure-Driven Bipolar Electrochemistry. *J. Am. Chem. Soc.* **2011**, *133*, 4687-4689.
43. Fosdick, S. E.; Crooks, R. M. Bipolar Electrodes for Rapid Screening of Electrocatalysts. *J. Am. Chem. Soc.* **2012**, *134*, 863-866.
44. Chang, B.-Y.; Chow, K.-F.; Crooks, J. A.; Mavré, F.; Crooks, R. M. Two-channel microelectrochemical bipolar electrode sensor array. *Analyst* **2012**, *137*, 2827-2833.
45. Fosdick, S. E.; Berglund, S. P.; Mullins, C. B.; Crooks, R. M. Parallel Screening of Electrocatalyst Candidates Using Bipolar Electrochemistry. *Anal. Chem.* **2013**, *85*, 2493-2499.
46. Arora, A.; Eijkel, J. C. T.; Morf, W. E.; Manz, A. A Wireless Electrochemiluminescence Detector Applied to Direct and Indirect Detection for Electrophoresis on a Microfabricated Glass Device. *Anal. Chem.* **2001**, *73*, 3282-3288.
47. Terrill, R. H.; Balss, K. M.; Zhang, Y. M.; Bohn, P. W. Dynamic monolayer gradients: Active spatiotemporal control of alkanethiol coatings on thin gold films. *J. Am. Chem. Soc.* **2000**, *122*, 988-989.

48. Duval, J.; Kleijn, J. M.; van Leeuwen, H. P. Bipolar electrode behaviour of the aluminium surface in a lateral electric field. *J. Electroanal. Chem.* **2001**, *505*, 1-11.
49. Mavré, F.; Anand, R. K.; Laws, D. R.; Chow, K.-F.; Chang, B.-Y.; Crooks, J. A.; Crooks, R. M. Bipolar Electrodes: A Useful Tool for Concentration, Separation, and Detection of Analytes in Microelectrochemical Systems. *Anal. Chem.* **2010**, *82*, 8766-8774.
50. Duval, J. F. L.; Huijs, G. K.; Threels, W. F.; Lyklema, J.; van Leeuwen, H. P. Faradaic depolarization in the electrokinetics of the metal-electrolyte solution interface. *J. Colloid Interface Sci.* **2003**, *260*, 95-106.
51. Duval, J. F. L.; Minor, M.; Cecilia, J.; van Leeuwen, H. P. Coupling of lateral electric field and transversal faradaic processes at the conductor/electrolyte solution interface. *J. Phys. Chem. B* **2003**, *107*, 4143-4155.
52. Duval, J. F. L.; van Leeuwen, H. P.; Cecilia, J.; Galceran, J. Rigorous analysis of reversible faradaic depolarization processes in the electrokinetics of the metal/electrolyte solution interface. *J. Phys. Chem. B* **2003**, *107*, 6782-6800.
53. Duval, J. F. L. Electrokinetics of the amphifunctional metal/electrolyte solution interface in the presence of a redox couple. *J. Colloid Interface Sci.* **2004**, *269*, 211-223.
54. Duval, J. F. L.; Buffle, J.; van Leeuwen, H. P. Quasi-reversible faradaic depolarization processes in the electrokinetics of the metal/solution interface. *J. Phys. Chem. B* **2006**, *110*, 6081-6094.
55. Bard, A. J.; Faulkner, L. R. *Electrochemical Methods: Fundamentals and Applications*; 2nd ed. John Wiley & Sons: New York, 2001.
56. Ndungu, P. G., *The Use of Bipolar Electrochemistry in Nanoscience: Contact Free Methods for the Site Selective Modification of Nanostructured Carbon Materials*. 2004, Drexel University: Philadelphia, PA.
57. Plana, D.; Shul, G.; Stephenson, M. J.; Dryfe, R. A. W. The voltammetric response of bipolar cells: Mechanistic investigations of electroless deposition. *Electrochem. Commun.* **2009**, *11*, 61-64.
58. Plana, D.; Jones, F. G. E.; Dryfe, R. A. W. The voltammetric response of bipolar cells: Reversible electron transfer. *J. Electroanal. Chem.* **2010**, *646*, 107-113.

59. Guerrette, J. P.; Oja, S. M.; Zhang, B. Coupled Electrochemical Reactions at Bipolar Microelectrodes and Nanoelectrodes. *Anal. Chem.* **2012**, *84*, 1609-1616.
60. Cox, J. T.; Guerrette, J. P.; Zhang, B. Steady-state voltammetry of a microelectrode in a closed bipolar cell. *Anal. Chem.* **2012**, *84*, 8797-804.
61. Klett, O.; Nyholm, L. Separation High Voltage Field Driven On-Chip Amperometric Detection in Capillary Electrophoresis. *Anal. Chem.* **2003**, *75*, 1245-1250.
62. Wang, J. Electrochemical detection for microscale analytical systems: a review. *Talanta* **2002**, *56*, 223-231.
63. Ordeig, O.; Godino, N.; del Campo, J.; Muñoz, F. X.; Nikolajeff, F.; Nyholm, L. On-Chip Electric Field Driven Electrochemical Detection Using a Poly(dimethylsiloxane) Microchannel with Gold Microband Electrodes. *Anal. Chem.* **2008**, *80*, 3622-3632.
64. Bard, A. J. *Electrogenerated Chemiluminescence*. Marcel Dekker, Inc.: New York, 2004.
65. Wu, M.-S.; Qian, G.-s.; Xu, J.-J.; Chen, H.-Y. Sensitive Electrochemiluminescence Detection of c-Myc mRNA in Breast Cancer Cells on a Wireless Bipolar Electrode. *Anal. Chem.* **2012**, *84*, 5407-5414.
66. Wu, M. S.; Yuan, D. J.; Xu, J. J.; Chen, H. Y. Electrochemiluminescence on bipolar electrodes for visual bioanalysis. *Chem Sci* **2013**, *4*, 1182-1188.
67. Zhan, W.; Crooks, R. M. Microelectrochemical logic circuits. *J. Am. Chem. Soc.* **2003**, *125*, 9934-9935.
68. Juskova, P.; Neuzil, P.; Manz, A.; Foret, F. Detection of electrochemiluminescence from floating metal platelets in suspension. *Lab Chip* **2013**, *13*, 781-4.
69. Bard, A. J. Inner-Sphere Heterogeneous Electrode Reactions. Electrocatalysis and Photocatalysis: The Challenge. *J. Am. Chem. Soc.* **2010**, *132*, 7559-7567.
70. Smotkin, E. S.; Díaz-Morales, R. R. New Electrocatalysts by Combinatorial Methods. *Annu. Rev. Mater. Res.* **2003**, *33*, 557-579.
71. Jeon, M. K.; Lee, C. H.; Park, G. I.; Kang, K. H. Combinatorial search for oxygen reduction reaction electrocatalysts: A review. *J. Power Sources* **2012**, *216*, 400-408.
72. Fernández, J. L.; Walsh, D. A.; Bard, A. J. Thermodynamic guidelines for the design of bimetallic catalysts for

oxygen electroreduction and rapid screening by scanning electrochemical microscopy. M-Co (M : Pd, Ag, Au). *J. Am. Chem. Soc.* **2005**, *127*, 357-365.
73. Fernández, J. L.; White, J. M.; Sun, Y. M.; Tang, W. J.; Henkelman, G.; Bard, A. J. Characterization and theory of electrocatalysts based on scanning electrochemical microscopy screening methods. *Langmuir* **2006**, *22*, 10426-10431.
74. Reddington, E.; Sapienza, A.; Gurau, B.; Viswanathan, R.; Sarangapani, S.; Smotkin, E. S.; Mallouk, T. E. Combinatorial Electrochemistry: A Highly Parallel, Optical Screening Method for Discovery of Better Electrocatalysts. *Science* **1998**, *280*, 1735-1737.
75. Sullivan, M. G.; Utomo, H.; Fagan, P. J.; Ward, M. D. Automated Electrochemical Analysis with Combinatorial Electrode Arrays. *Anal. Chem.* **1999**, *71*, 4369-4375.
76. Strasser, P.; Fan, Q.; Devenney, M.; Weinberg, W. H.; Liu, P.; Nørskov, J. K. High Throughput Experimental and Theoretical Predictive Screening of Materials – A Comparative Study of Search Strategies for New Fuel Cell Anode Catalysts. *J. Phys. Chem. B* **2003**, *107*, 11013-11021.
77. Guerin, S.; Hayden, B. E.; Lee, C. E.; Mormiche, C.; Owen, J. R.; Russell, A. E.; Theobald, B.; Thompsett, D. Combinatorial Electrochemical Screening of Fuel Cell Electrocatalysts. *J. Comb. Chem.* **2004**, *6*, 149-158.
78. Neyerlin, K. C.; Bugosh, G.; Forgie, R.; Liu, Z. C.; Strasser, P. Combinatorial Study of High-Surface-Area Binary and Ternary Electrocatalysts for the Oxygen Evolution Reaction. *J. Electrochem. Soc.* **2009**, *156*, B363-B369.
79. Woodhouse, M.; Parkinson, B. A. Combinatorial Discovery and Optimization of a Complex Oxide with Water Photoelectrolysis Activity. *Chem. Mat.* **2008**, *20*, 2495-2502.
80. Ye, H.; Lee, J.; Jang, J. S.; Bard, A. J. Rapid Screening of BiVO4-Based Photocatalysts by Scanning Electrochemical Microscopy (SECM) and Studies of Their Photoelectrochemical Properties. *J. Phys. Chem. C* **2010**, *114*, 13322-13328.
81. Shan, X. N.; Diez-Perez, I.; Wang, L. J.; Wiktor, P.; Gu, Y.; Zhang, L. H.; Wang, W.; Lu, J.; Wang, S. P.; Gong, Q. H.; Li, J. H.; Tao, N. J. Imaging the electrocatalytic

activity of single nanoparticles. *Nat. Nanotechnol.* **2012**, *7*, 668-672.
82. Fosdick, S. E.; Berglund, S. P.; Mullins, C. B.; Crooks, R. M. Evaluating Electrocatalysts for the Hydrogen Evolution Reaction based on Bi- and Trimetallic Combinations of Co, Fe, Ni, Mo, and W using Bipolar Electrode Arrays. *ACS Catalysis* **2014**, *submitted*.
83. Fosdick, S. E.; Anderson, M. J.; Nettleton, E. G.; Crooks, R. M. Correlated Electrochemical and Optical Tracking of Discrete Collision Events. *J. Am. Chem. Soc.* **2013**, *135*, 5994-5997.
84. Fosdick, S. E.; Anderson, M. J.; Renault, C.; DeGregory, P. R.; Loussaert, J. A.; Crooks, R. M. Wire, Mesh, and Fiber Electrodes for Paper-based Electroanalytical Devices. *Anal. Chem.* **2014**, *submitted*.
85. Xiang, C.; Suram, S. K.; Haber, J. A.; Guevarra, D. W.; Jin, J.; Gregoire, J. M. A High Throughput Bubble Screening Method for Combinatorial Discovery of Electrocatalysts for Water Splitting. *ACS Comb. Sci.* **2013**, *ASAP*.
86. Ye, H.; Crooks, J. A.; Crooks, R. M. Effect of particle size on the kinetics of the electrocatalytic oxygen reduction reaction catalyzed by Pt dendrimer-encapsulated nanoparticles. *Langmuir* **2007**, *23*, 11901-11906.
87. Kim, Y. G.; Oh, S. K.; Crooks, R. M. Preparation and characterization of 1-2 nm dendrimer-encapsulated gold nanoparticles having very narrow size distributions. *Chem. Mat.* **2004**, *16*, 167-172.
88. Myers, V. S.; Weir, M. G.; Carino, E. V.; Yancey, D. F.; Pande, S.; Crooks, R. M. Dendrimer-encapsulated nanoparticles: New synthetic and characterization methods and catalytic applications. *Chem Sci* **2011**, *2*, 1632-1646.
89. Yancey, D. F.; Carino, E. V.; Crooks, R. M. Electrochemical Synthesis and Electrocatalytic Properties of Au@Pt Dendrimer-Encapsulated Nanoparticles. *J. Am. Chem. Soc.* **2010**, *132*, 10988-10989.
90. Schlapak, R.; Armitage, D.; Saucedo-Zeni, N.; Latini, G.; Gruber, H. J.; Mesquida, P.; Samotskaya, Y.; Hohage, M.; Cacialli, F.; Howorka, S. Preparation and Characterization of Dense Films of Poly(amidoamine) Dendrimers on Indium Tin Oxide. *Langmuir* **2007**, *23*, 8916-8924.

91. Armstrong, N. R.; Lin, A. W. C.; Fujihira, M.; Kuwana, T. Electrochemical and surface characteristics of tin oxide and indium oxide electrodes. *Anal. Chem.* **1976**, *48*, 741-750.
92. Duval, J. F. L.; Kleijn, J. M.; van Leeuwen, H. P. Bipolar electrode behaviour of the aluminium surface in a lateral electric field. *J. Electroanal. Chem.* **2001**, *505*, 1-11.
93. Lin, X.; Zheng, L.; Gao, G.; Chi, Y.; Chen, G. Electrochemiluminescence Imaging-Based High-Throughput Screening Platform for Electrocatalysts Used in Fuel Cells. *Anal. Chem.* **2012**, *84*, 7700-7707.
94. Walsh, D. A.; Fernández, J. L.; Bard, A. J. Rapid screening of bimetallic electrocatalysts for oxygen reduction in acidic media by scanning electrochemical microscopy. *J. Electrochem. Soc.* **2006**, *153*, E99-E103.
95. Bard, A. J.; Parsons, R.; Jordan, J.; Eds. *Standard Potentials in Aqueous Solutions*. Marcel Dekker: New York, 1985.
96. Berglund, S. P.; Lee, H. C.; Nuñez, P. D.; Mullins, C. B. Screening of Transition and Post- Transition Metals to Incorporate into Copper Oxide and Copper Bismuth Oxide for Photoelectrochemical Oxygen Evolution. *Phys. Chem. Chem. Phys.* **2013**, *submitted*.
97. Lin, C.-L.; Sánchez-Sánchez, C. M.; Bard, A. J. Methanol Tolerance of Pd–Co Oxygen Reduction Reaction Electrocatalysts Using Scanning Electrochemical Microscopy. *Electrochem. Solid-State Lett.* **2008**, *11*, B136-B139.
98. Yu, T. H.; Sha, Y.; Merinov, B. V.; Goddard, W. A. Improved Non-Pt Alloys for the Oxygen Reduction Reaction at Fuel Cell Cathodes Predicted from Quantum Mechanics. *J. Phys. Chem. C* **2010**, *114*, 11527-11533.
99. Lee, K. R.; Jung, Y.; Woo, S. I. Combinatorial Screening of Highly Active Pd Binary Catalysts for Electrochemical Oxygen Reduction. *ACS Comb. Sci.* **2011**, *14*, 10-16.
100. Mustain, W. E.; Kepler, K.; Prakash, J. CoPdx oxygen reduction electrocatalysts for polymer electrolyte membrane and direct methanol fuel cells. *Electrochim. Acta* **2007**, *52*, 2102-2108.
101. Koenigsmann, C.; Sutter, E.; Chiesa, T. A.; Adzic, R. R.; Wong, S. S. Highly Enhanced Electrocatalytic Oxygen Reduction Performance Observed in Bimetallic Palladium-

Based Nanowires Prepared under Ambient, Surfactantless Conditions. *Nano Lett.* **2012**, *12*, 2013-2020.
102. Shao, M.; Liu, P.; Zhang, J.; Adzic, R. Origin of Enhanced Activity in Palladium Alloy Electrocatalysts for Oxygen Reduction Reaction†. *J. Phys. Chem. B* **2007**, *111*, 6772-6775.
103. Li, W.; Fan, F.-R. F.; Bard, A. J. The application of scanning electrochemical microscopy to the discovery of Pd-W electrocatalysts for the oxygen reduction reaction that demonstrate high activity, stability, and methanol tolerance. *J. Solid State Electrochem.* **2012**, *16*, 2563-2568.
104. Loget, G.; Kuhn, A. Shaping and exploring the micro- and nanoworld using bipolar electrochemistry. *Anal. Bioanal. Chem.* **2011**, *400*, 1691-1704.
105. Loget, G.; Zigah, D.; Bouffier, L.; Sojic, N.; Kuhn, A. Bipolar Electrochemistry: From Materials Science to Motion and Beyond. *Acc. Chem. Res.* **2013**, *46*, 2513-2523.
106. Fosdick, S. E.; Knust, K. N.; Scida, K.; Crooks, R. M. Bipolar Electrochemistry. *Angew. Chem., Int. Ed.* **2013**, *52*, 10438-10456.
107. He, T.; Kreidler, E.; Xiong, L.; Ding, E. Combinatorial screening and nano-synthesis of platinum binary alloys for oxygen electroreduction. *J. Power Sources* **2007**, *165*, 87-91.
108. Lee, K. R.; Jeon, M. K.; Woo, S. I. Composition optimization of PtRuM/C (M = Fe and Mo) catalysts for methanol electro-oxidation via combinatorial method. *Appl. Catal., B* **2009**, *91*, 428-433.
109. Dang, T.; Ramsaran, R.; Roy, S.; Froehlich, J.; Wang, J.; Kubiak, C. P. Design of a High Throughput 25-Well Parallel Electrolyzer for the Accelerated Discovery of CO2 Reduction Catalysts via a Combinatorial Approach. *Electroanalysis* **2011**, *23*, 2335-2342.
110. Zhang, Y.; McGinn, P. J. Combinatorial screening for methanol oxidation catalysts in alloys of Pt, Cr, Co and V. *J. Power Sources* **2012**, *206*, 29-36.
111. Liu, G.; Bard, A. J. Rapid Preparation and Photoelectrochemical Screening of CuInSe2 and CuInMSe2 Arrays by Scanning Electrochemical Microscopy. *J. Phys. Chem. C* **2010**, *114*, 17509-17513.
112. Berglund, S. P.; Lee, H. C.; Nunez, P. D.; Bard, A. J.; Mullins, C. B. Screening of transition and post-transition metals to incorporate into copper oxide and copper bismuth

oxide for photoelectrochemical hydrogen evolution. *Phys. Chem. Chem. Phys.* **2013**, *15*, 4554-65.
113. Liu, G.; Liu, C.; Bard, A. J. Rapid synthesis and screening of ZnxCd1-xSySe1-y photocatalysts by scanning electrochemical microscopy. *J. Phys. Chem. C* **2010**, *114*, 20997-21002.
114. Ye, H.; Park, H. S.; Bard, A. J. Screening of Electrocatalysts for Photoelectrochemical Water Oxidation on W-Doped BiVO4 Photocatalysts by Scanning Electrochemical Microscopy. *J. Phys. Chem. C* **2011**, *115*, 12464-12470.
115. Zhang, F.; Roznyatovskiy, V.; Fan, F.-R. F.; Lynch, V.; Sessler, J. L.; Bard, A. J. A Method for Rapid Screening of Photosensitizers by Scanning Electrochemical Microscopy (SECM) and the Synthesis and Testing of a Porphyrin Sensitizer. *J. Phys. Chem. C* **2011**, *115*, 2592-2599.
116. Weng, Y.-C.; Hsieh, C.-T. Scanning electrochemical microscopy characterization of bimetallic Pt-M (M = Pd, Ru, Ir) catalysts for hydrogen oxidation. *Electrochim. Acta* **2010**, *56*, 1932-1940.
117. Fernández, J. L.; Raghuveer, V.; Manthiram, A.; Bard, A. J. Pd–Ti and Pd–Co–Au Electrocatalysts as a Replacement for Platinum for Oxygen Reduction in Proton Exchange Membrane Fuel Cells. *J. Am. Chem. Soc.* **2005**, *127*, 13100-13101.
118. Johnson, L.; Walsh, D. A. Tip generation–substrate collection–tip collection mode scanning electrochemical microscopy of oxygen reduction electrocatalysts. *J. Electroanal. Chem.* **2012**, *682*, 45-52.
119. Chai, G. S.; Yu, J.-S. Highly efficient Pt-Ru-Co-W quaternary anode catalysts for methanol electrooxidation discovered by combinatorial analysis. *J. Mater. Chem.* **2009**, *19*, 6842-6848.
120. Welsch, F. G.; Stowe, K.; Maier, W. F. Fluorescence-based high throughput screening for noble metal-free and platinum-poor anode catalysts for the direct methanol fuel cell. *ACS Comb. Sci.* **2011**, *13*, 518-529.
121. Jaramillo, T. F.; Ivanovskaya, A.; McFarland, E. W. High-Throughput Screening System for Catalytic Hydrogen-Producing Materials. *J. Comb. Chem.* **2001**, *4*, 17-22.
122. Brace, K. M.; Hayden, B. E.; Russell, A. E.; Owen, J. R. A Parallel Optical Screen for the Rapid Combinatorial

Electrochromic Analysis of Electrochemical Materials. *Adv. Mater.* **2006**, *18*, 3253-3257.
123. Xiang, C.; Suram, S. K.; Haber, J. A.; Guevarra, D. W.; Jin, J.; Gregoire, J. M. A High Throughput Bubble Screening Method for Combinatorial Discovery of Electrocatalysts for Water Splitting. *ACS Comb. Sci.* **2013**.
124. Guerrette, J. P.; Percival, S. J.; Zhang, B. Fluorescence coupling for direct imaging of electrocatalytic heterogeneity. *J. Am. Chem. Soc.* **2013**, *135*, 855-61.
125. Fosdick, S. E.; Crooks, R. M. Bipolar Electrodes for Rapid Screening of Electrocatalysts. *J. Am. Chem. Soc.* **2012**, *134*, 863-866.
126. Yang, C.-J. An impending platinum crisis and its implications for the future of the automobile. *Energy Policy* **2009**, *37*, 1805-1808.
127. Raj, I. A. Nickel-based, binary-composite electrocatalysts for the cathodes in the energy-efficient industrial production of hydrogen from alkaline-water electrolytic cells. *J Mater Sci* **1993**, *28*, 4375-4382.
128. Trasatti, S. Work function, electronegativity, and electrochemical behaviour of metals: III. Electrolytic hydrogen evolution in acid solutions. *J. Electroanal. Chem. Interfacial Electrochem.* **1972**, *39*, 163-184.
129. Miles, M. H. Evaluation of electrocatalysts for water electrolysis in alkaline solutions. *J. Electroanal. Chem. Interfacial Electrochem.* **1975**, *60*, 89-96.
130. Fan, C.; Piron, D. L.; Paradis, P. Hydrogen evolution on electrodeposited nickel-cobalt-molybdenum in alkaline water electrolysis. *Electrochim. Acta* **1994**, *39*, 2715-2722.
131. Highfield, J. G.; Claude, E.; Oguro, K. Electrocatalytic synergism in Ni/Mo cathodes for hydrogen evolution in acid medium: a new model. *Electrochim. Acta* **1999**, *44*, 2805-2814.
132. Jakšić, J. M.; Vojnović, M. V.; Krstajić, N. V. Kinetic analysis of hydrogen evolution at Ni–Mo alloy electrodes. *Electrochim. Acta* **2000**, *45*, 4151-4158.
133. Gennero de Chialvo, M. R.; Chialvo, A. C. Hydrogen evolution reaction on smooth Ni(1−x)+Mo(x) alloys (0≤x≤0.25). *J. Electroanal. Chem.* **1998**, *448*, 87-93.
134. Navarro-Flores, E.; Chong, Z.; Omanovic, S. Characterization of Ni, NiMo, NiW and NiFe electroactive

coatings as electrocatalysts for hydrogen evolution in an acidic medium. *J. Mol. Catal. A: Chem.* **2005**, *226*, 179-197.
135. Dumitrescu, I.; Yancey, D. F.; Crooks, R. M. Dual-electrode microfluidic cell for characterizing electrocatalysts. *Lab Chip* **2012**, *12*, 986-993.
136. Arce-Estrada, E.; Lopez-Hirata, V.; Martinez-Lopez, L.; Dorantes-Rosales, H.; Saucedo-Muñoz, M.; Hernández-Santiago, F. Electrocatalytic properties of mechanically alloyed Co-20wt%Ni-10wt%Mo and Co-70wt%Ni-10wt%Mo alloy powders. *J. Mater. Sci.* **2003**, *38*, 275-278.
137. Raj, I. A.; Vasu, K. I. Transition metal-based cathodes for hydrogen evolution in alkaline solution: Electrocatalysis on nickel-based ternary electrolytic codeposits. *J. Appl. Electrochem.* **1992**, *22*, 471-477.
138. McKone, J. R.; Sadtler, B. F.; Werlang, C. A.; Lewis, N. S.; Gray, H. B. Ni-Mo Nanopowders for Efficient Electrochemical Hydrogen Evolution. *ACS Catalysis* **2013**, *3*, 166-169.
139. Greeley, J.; Nørskov, J. K. Large-scale, density functional theory-based screening of alloys for hydrogen evolution. *Surf. Sci.* **2007**, *601*, 1590-1598.
140. Trasatti, S.; Petrii, O. A. Real surface area measurements in electrochemistry. *J. Electroanal. Chem.* **1992**, *327*, 353-376.
141. Ulrich, C.; Andersson, O.; Nyholm, L.; Björefors, F. Formation of molecular gradients on bipolar electrodes. *Angew. Chem., Int. Ed.* **2008**, *47*, 3034-3036.
142. Ulrich, C.; Andersson, O.; Nyholm, L.; Björefors, F. Potential and Current Density Distributions at Electrodes Intended for Bipolar Patterning. *Anal. Chem.* **2009**, *81*, 453-459.
143. Ramakrishnan, S.; Shannon, C. Display of Solid-State Materials Using Bipolar Electrochemistry. *Langmuir* **2010**, *26*, 4602-4606.
144. Bradley, J.-C.; Ma, Z. M. Contactless electrodeposition of palladium catalysts. *Angew. Chem., Int. Ed.* **1999**, *38*, 1663-1666.
145. Chow, K. F.; Mavré, F.; Crooks, J. A.; Chang, B. Y.; Crooks, R. M. A Large-Scale, Wireless Electrochemical Bipolar Electrode Microarray. *J. Am. Chem. Soc.* **2009**, *131*, 8364-8365.

146. Quinn, B. M.; van 't Ho, P. G.; Lemay, S. G. Time-Resolved Electrochemical Detection of Discrete Adsorption Events. *J. Am. Chem. Soc.* **2004**, *126*, 8360-8361.
147. Boika, A.; Thorgaard, S. N.; Bard, A. J. Monitoring the Electrophoretic Migration and Adsorption of Single Insulating Nanoparticles at Ultramicroelectrodes. *J. Phys. Chem. B* **2012**, *ASAP*, DOI: 10.1021/jp306934g.
148. Bard, A. J.; Zhou, H. J.; Kwon, S. J. Electrochemistry of Single Nanoparticles via Electrocatalytic Amplification. *Isr. J. Chem.* **2010**, *50*, 267-276.
149. Xiao, X. Y.; Bard, A. J. Observing single nanoparticle collisions at an ultramicroelectrode by electrocatalytic amplification. *J. Am. Chem. Soc.* **2007**, *129*, 9610-9612.
150. Zhou, Y. G.; Rees, N. V.; Compton, R. G. The Electrochemical Detection and Characterization of Silver Nanoparticles in Aqueous Solution. *Angew. Chem., Int. Ed.* **2011**, *50*, 4219-4221.
151. Kleijn, S. E. F.; Lai, S. C. S.; Miller, T. S.; Yanson, A. I.; Koper, M. T. M.; Unwin, P. R. Landing and Catalytic Characterization of Individual Nanoparticles on Electrode Surfaces. *J. Am. Chem. Soc.* **2012**, *134*, 18558-18561.
152. Xiao, X. Y.; Fan, F. R. F.; Zhou, J. P.; Bard, A. J. Current Transients in Single Nanoparticle Collision Events. *J. Am. Chem. Soc.* **2008**, *130*, 16669-16677.
153. Xiao, X. Y.; Pan, S. L.; Jang, J. S.; Fan, F. R. F.; Bard, A. J. Single Nanoparticle Electrocatalysis: Effect of Monolayers on Particle and Electrode on Electron Transfer. *J. Phys. Chem. C* **2009**, *113*, 14978-14982.
154. Kwon, S. J.; Fan, F. R. F.; Bard, A. J. Observing Iridium Oxide (IrOx) Single Nanoparticle Collisions at Ultramicroelectrodes. *J. Am. Chem. Soc.* **2010**, *132*, 13165-13167.
155. Zhou, H. J.; Fan, F. R. F.; Bard, A. J. Observation of Discrete Au Nanoparticle Collisions by Electrocatalytic Amplification Using Pt Ultramicroelectrode Surface Modification. *J. Phys. Chem. Lett.* **2010**, *1*, 2671-2674.
156. Kwon, S. J.; Zhou, H.; Fan, F.-R. F.; Vorobyev, V.; Zhang, B.; Bard, A. J. Stochastic electrochemistry with electrocatalytic nanoparticles at inert ultramicroelectrodes-theory and experiments. *Phys. Chem. Chem. Phys.* **2011**, *13*, 5394-5402.

157. Kwon, S. J.; Bard, A. J. DNA Analysis by Application of Pt Nanoparticle Electrochemical Amplification with Single Label Response. *J. Am. Chem. Soc.* **2012**, *134*, 10777-10779.
158. Kwon, S. J.; Bard, A. J. Analysis of Diffusion-Controlled Stochastic Events of Iridium Oxide Single Nanoparticle Collisions by Scanning Electrochemical Microscopy. *J. Am. Chem. Soc.* **2012**, *134*, 7102-7108.
159. Zhou, H. J.; Park, J. H.; Fan, F. R. F.; Bard, A. J. Observation of Single Metal Nanoparticle Collisions by Open Circuit (Mixed) Potential Changes at an Ultramicroelectrode. *J. Am. Chem. Soc.* **2012**, *134*, 13212-13215.
160. Zhou, Y. G.; Rees, N. V.; Compton, R. G. Nanoparticle-electrode collision processes: The electroplating of bulk cadmium on impacting silver nanoparticles. *Chem. Phys. Lett.* **2011**, *511*, 183-186.
161. Zhou, Y. G.; Rees, N. V.; Compton, R. G. Nanoparticle-Electrode Collision Processes: The Underpotential deposition of Thallium on Silver Nanoparticles in Aqueous Solution. *ChemPhysChem* **2011**, *12*, 2085-2087.
162. Zhou, Y. G.; Stuart, E. J. E.; Pillay, J.; Vilakazi, S.; Tshikhudo, R.; Rees, N. V.; Compton, R. G. Electrode-nanoparticle collisions: The measurement of the sticking coefficients of gold and nickel nanoparticles from aqueous solution onto a carbon electrode. *Chem. Phys. Lett.* **2012**, *551*, 68-71.
163. Zhou, Y.-G.; Rees, N. V.; Compton, R. G. The electrochemical detection of tagged nanoparticles via particle-electrode collisions: nanoelectroanalysis beyond immobilisation. *Chem. Commun.* **2012**, *48*, 2510-2512.
164. Dasari, R.; Robinson, D. A.; Stevenson, K. J. Ultrasensitive Electroanalytical Tool for Detecting, Sizing, and Evaluating the Catalytic Activity of Platinum Nanoparticles. *J. Am. Chem. Soc.* **2012**, *135*, 570-573.
165. Alligrant, T. M.; Nettleton, E. G.; Crooks, R. M. Electrochemical detection of individual DNA hybridization events. *Lab Chip* **2013**, *13*, 349-354.
166. Zevenbergen, M. A. G.; Singh, P. S.; Goluch, E. D.; Wolfrum, B. L.; Lemay, S. G. Electrochemical Correlation Spectroscopy in Nanofluidic Cavities. *Anal. Chem.* **2009**, *81*, 8203-8212.

167. Bergren, A. J.; Porter, M. D. Selectivity mechanisms at self-assembled monolayers on gold: Implications in redox recycling amplification systems. *J. Electroanal. Chem.* **2007**, *599*, 12-22.
168. Perera, D. M. N. T.; Ito, T. Cyclic voltammetry on recessed nanodisk-array electrodes prepared from track-etched polycarbonate membranes with 10-nm diameter pores. *Analyst* **2010**, *135*, 172-176.
169. Wang, J.; Tian, B.; Nascimento, V. B.; Angnes, L. Performance of screen-printed carbon electrodes fabricated from different carbon inks. *Electrochim. Acta* **1998**, *43*, 3459-3465.
170. Fanjul-Bolado, P.; Hernández-Santos, D.; Lamas-Ardisana, P. J.; Martín-Pernía, A.; Costa-García, A. Electrochemical characterization of screen-printed and conventional carbon paste electrodes. *Electrochim. Acta* **2008**, *53*, 3635-3642.
171. Töbjork, D.; Österbacka, R. Paper electronics. *Adv. Mater.* **2011**, *23*, 1935-61.
172. Ge, S.; Ge, L.; Yan, M.; Song, X.; Yu, J.; Huang, J. A disposable paper-based electrochemical sensor with an addressable electrode array for cancer screening. *Chem. Commun.* **2012**, *48*, 9397-9399.
173. Wu, Y.; Xue, P.; Hui, K. M.; Kang, Y. A paper-based microfluidic electrochemical immunodevice integrated with amplification-by-polymerization for the ultrasensitive multiplexed detection of cancer biomarkers. *Biosens. Bioelectron.* **2014**, *52*, 180-187.
174. Martinez, A. W.; Phillips, S. T.; Butte, M. J.; Whitesides, G. M. Patterned Paper as a Platform for Inexpensive, Low-Volume, Portable Bioassays. *Angew. Chem., Int. Ed.* **2007**, *46*, 1318-1320.
175. Martinez, A. W.; Phillips, S. T.; Whitesides, G. M. Three-dimensional microfluidic devices fabricated in layered paper and tape. *Proc. Natl. Acad. Sci. U. S. A.* **2008**, *105*, 19606-19611.
176. Li, X.; Ballerini, D. R.; Shen, W. A perspective on paper-based microfluidics: Current status and future trends. *Biomicrofluidics* **2012**, *6*, 11301.
177. Parolo, C.; Merkoci, A. Paper-based nanobiosensors for diagnostics. *Chem. Soc. Rev.* **2013**, *42*, 450-457.

178. Yetisen, A. K.; Akram, M. S.; Lowe, C. R. Paper-based microfluidic point-of-care diagnostic devices. *Lab Chip* **2013**, *13*, 2210-2251.
179. Dungchai, W.; Chailapakul, O.; Henry, C. S. Use of multiple colorimetric indicators for paper-based microfluidic devices. *Anal. Chim. Acta* **2010**, *674*, 227-33.
180. Vella, S. J.; Beattie, P.; Cademartiri, R.; Laromaine, A.; Martinez, A. W.; Phillips, S. T.; Mirica, K. A.; Whitesides, G. M. Measuring Markers of Liver Function Using a Micropatterned Paper Device Designed for Blood from a Fingerstick. *Anal. Chem.* **2012**, *84*, 2883-2891.
181. Mentele, M. M.; Cunningham, J.; Koehler, K.; Volckens, J.; Henry, C. S. Microfluidic Paper-Based Analytical Device for Particulate Metals. *Anal. Chem.* **2012**, *84*, 4474-4480.
182. Carrilho, E.; Phillips, S. T.; Vella, S. J.; Martinez, A. W.; Whitesides, G. M. Paper Microzone Plates. *Anal. Chem.* **2009**, *81*, 5990-5998.
183. Allen, P. B.; Arshad, S. A.; Li, B.; Chen, X.; Ellington, A. D. DNA circuits as amplifiers for the detection of nucleic acids on a paperfluidic platform. *Lab Chip* **2012**, *12*, 2951-2958.
184. Scida, K.; Li, B.; Ellington, A. D.; Crooks, R. M. DNA Detection Using Origami Paper Analytical Devices. *Anal. Chem.* **2013**, *85*, 9713-9720.
185. Dungchai, W.; Chailapakul, O.; Henry, C. S. Electrochemical Detection for Paper-Based Microfluidics. *Anal. Chem.* **2009**, *81*, 5821-5826.
186. Carvalhal, R. F.; Simão Kfouri, M.; de Oliveira Piazetta, M. H.; Gobbi, A. L.; Kubota, L. T. Electrochemical Detection in a Paper-Based Separation Device. *Anal. Chem.* **2010**, *82*, 1162-1165.
187. Noiphung, J.; Songjaroen, T.; Dungchai, W.; Henry, C. S.; Chailapakul, O.; Laiwattanapaisal, W. Electrochemical detection of glucose from whole blood using paper-based microfluidic devices. *Anal. Chim. Acta* **2013**, *788*, 39-45.
188. Nie, Z.; Deiss, F.; Liu, X.; Akbulut, O.; Whitesides, G. M. Integration of paper-based microfluidic devices with commercial electrochemical readers. *Lab Chip* **2010**, *10*, 3163-9.

189. Maxwell, J. E.; Mazzeo, A. D.; Whitesides, G. M. Paper-based electroanalytical devices for accessible diagnostic testing. *MRS Bulletin* **2013**, *38*, 309-314.
190. Nie, Z.; Nijhuis, C. A.; Gong, J.; Chen, X.; Kumachev, A.; Martinez, A. W.; Narovlyansky, M.; Whitesides, G. M. Electrochemical sensing in paper-based microfluidic devices. *Lab Chip* **2010**, *10*, 477-483.
191. Liu, H.; Xiang, Y.; Lu, Y.; Crooks, R. M. Aptamer-based origami paper analytical device for electrochemical detection of adenosine. *Angew. Chem., Int. Ed.* **2012**, *51*, 6925-8.
192. Thom, N. K.; Yeung, K.; Pillion, M. B.; Phillips, S. T. "Fluidic batteries" as low-cost sources of power in paper-based microfluidic devices. *Lab Chip* **2012**, *12*, 1768-1770.
193. Wang, P.; Ge, L.; Yan, M.; Song, X.; Ge, S.; Yu, J. Paper-based three-dimensional electrochemical immunodevice based on multi-walled carbon nanotubes functionalized paper for sensitive point-of-care testing. *Biosens. Bioelectron.* **2012**, *32*, 238-243.
194. Michael, A. C.; Wightman, R. M., *Microelectrodes*, in *Laboratory Techniques in Electroanalytical Chemistry, Second Edition, Revised and Expanded*, P. Kissinger and W.R. Heineman, Editors. 1996, Taylor & Francis. p. 367-402.
195. Santhiago, M.; Wydallis, J. B.; Kubota, L. T.; Henry, C. S. Construction and Electrochemical Characterization of Microelectrodes for Improved Sensitivity in Paper-Based Analytical Devices. *Anal. Chem.* **2013**, *85*, 5233-5239.
196. Nuwer, M. J.; Osteryoung, J. Electrochemical behavior of N-acetylpenicillamine thionitrite at glassy carbon and carbon fiber electrodes. *Anal. Chem.* **1989**, *61*, 1954-1959.
197. Liu, Y.; Vickers, J. A.; Henry, C. S. Simple and Sensitive Electrode Design for Microchip Electrophoresis/Electrochemistry. *Anal. Chem.* **2004**, *76*, 1513-1517.
198. Salaün, P.; Gibbon-Walsh, K.; van den Berg, C. M. G. Beyond the Hydrogen Wave: New Frontier in the Detection of Trace Elements by Stripping Voltammetry. *Anal. Chem.* **2011**, *83*, 3848-3856.
199. Alves, G. M. S.; Magalhães, J. M. C. S.; Tauler, R.; Soares, H. M. V. M. Simultaneous Anodic Stripping Voltammetric Determination of Pb and Cd, Using a Vibrating

Gold Microwire Electrode, Assisted by Chemometric Techniques. *Electroanalysis* **2013**, *25*, 1895-1906.
200. Yu, A.; Shang, J.; Cheng, F.; Paik, B. A.; Kaplan, J. M.; Andrade, R. B.; Ratner, D. M. Biofunctional Paper via the Covalent Modification of Cellulose. *Langmuir* **2012**, *28*, 11265-11273.
201. Araújo, A. C.; Song, Y.; Lundeberg, J.; Ståhl, P. L.; Brumer, H. Activated Paper Surfaces for the Rapid Hybridization of DNA through Capillary Transport. *Anal. Chem.* **2012**, *84*, 3311-3317.
202. Cheng, C.-M.; Martinez, A. W.; Gong, J.; Mace, C. R.; Phillips, S. T.; Carrilho, E.; Mirica, K. A.; Whitesides, G. M. Paper-Based ELISA. *Angew. Chem., Int. Ed.* **2010**, *49*, 4771-4774.
203. Wang, P.; Ge, L.; Ge, S.; Yu, J.; Yan, M.; Huang, J. A paper-based photoelectrochemical immunoassay for low-cost and multiplexed point-of-care testing. *Chem. Commun.* **2013**, *49*, 3294-3296.
204. Renault, C.; Li, X.; Fosdick, S. E.; Crooks, R. M. Hollow-Channel Paper Analytical Devices. *Anal. Chem.* **2013**, *85*, 7976-7979.
205. Cannes, C.; Kanoufi, F.; Bard, A. J. Cyclic voltammetry and scanning electrochemical microscopy of ferrocenemethanol at monolayer and bilayer-modified gold electrodes. *J. Electroanal. Chem.* **2003**, *547*, 83-91.
206. Liu, H.; Crooks, R. M. Three-Dimensional Paper Microfluidic Devices Assembled Using the Principles of Origami. *J. Am. Chem. Soc.* **2011**, *133*, 17564-17566.
207. Lu, Y.; Shi, W.; Jiang, L.; Qin, J.; Lin, B. Rapid prototyping of paper-based microfluidics with wax for low-cost, portable bioassay. *Electrophoresis* **2009**, *30*, 1497-1500.
208. Renault, C.; Anderson, M. J.; Crooks, R. M. Electrochemistry and Mass Transfer in Hollow-Channel Paper Analytical Devices. *J. Am. Chem. Soc.* **2014**, *in revision*.
209. Glavan, A. C.; Martinez, R. V.; Maxwell, E. J.; Subramaniam, A. B.; Nunes, R. M. D.; Soh, S.; Whitesides, G. M. Rapid Fabrication of Pressure-driven Open-Channel Microfluidic Devices in Omniphobic RF Paper. *Lab Chip* **2013**, *13*, 2922-30.
210. Molina, A.; Gonzalez, J.; Henstridge, M. C.; Compton, R. G. Voltammetry of Electrochemically Reversible Systems at

Electrodes of Any Geometry: A General, Explicit Analytical Characterization. *J. Phys. Chem. C* **2011**, *115*, 4054-4062.
211. Szabo, A.; Cope, D. K.; Tallman, D. E.; Kovach, P. M.; Wightman, R. M. Chronoamperometric current at hemicylinder and band microelectrodes: Theory and experiment. *J. Electroanal. Chem. Interfacial Electrochem.* **1987**, *217*, 417-423.
212. Chidsey, C. E. D.; Bertozzi, C. R.; Putvinski, T. M.; Mujsce, A. M. Coadsorption of ferrocene-terminated and unsubstituted alkanethiols on gold: electroactive self-assembled monolayers. *J. Am. Chem. Soc.* **1990**, *112*, 4301-4306.
213. Collard, D. M.; Fox, M. A. Use of electroactive thiols to study the formation and exchange of alkanethiol monolayers on gold. *Langmuir* **1991**, *7*, 1192-1197.
214. Uosaki, K.; Sato, Y.; Kita, H. Electrochemical characteristics of a gold electrode modified with a self-assembled monolayer of ferrocenylalkanethiols. *Langmuir* **1991**, *7*, 1510-1514.
215. Cruanes, M. T.; Drickamer, H. G.; Faulkner, L. R. Characterization of Charge Transfer Processes in Self-Assembled Monolayers by High-Pressure Electrochemical Techniques. *Langmuir* **1995**, *11*, 4089-4097.
216. Takehara, K.; Takemura, H.; Ide, Y. Electrochemical studies of the terminally substituted alkanethiol monolayers formed on a gold electrode: Effects of the terminal group on the redox responses of Fe(CN)3−6, Ru(NH3)3+6 and ferrocenedimethanol. *Electrochim. Acta* **1994**, *39*, 817-822.
217. Cattabriga, M.; Ferri, V.; Tran, E.; Galloni, P.; Rampi, M. A. Electrochemical characterization of redox centers organized at Hg surfaces. *Inorg. Chim. Acta* **2007**, *360*, 1095-1101.
218. Sun, L.; Johnson, B.; Wade, T.; Crooks, R. M. Selective electrostatic binding of ions by monolayers of mercaptan derivatives adsorbed to gold substrates. *J. Phys. Chem.* **1990**, *94*, 8869-8871.
219. Tokuhisa, H.; Zhao, M.; Baker, L. A.; Phan, V. T.; Dermody, D. L.; Garcia, M. E.; Peez, R. F.; Crooks, R. M.; Mayer, T. M. Preparation and Characterization of Dendrimer Monolayers and Dendrimer−Alkanethiol Mixed Monolayers Adsorbed to Gold. *J. Am. Chem. Soc.* **1998**, *120*, 4492-4501.

220. Yang, M.; Zhang, Z. Impediment to heterogeneous electron transfer reactions of redox-active species by alkanedithiol self-assembled monolayers with and without an adlayer of Au nanoparticles. *Electrochim. Acta* **2004**, *49*, 5089-5095.
221. Campiña, J. M.; Martins, A.; Silva, F. Probing the Organization of Charged Self-Assembled Monolayers by Using the Effects of pH, Time, Electrolyte Anion, and Temperature, on the Charge Transfer of Electroactive Probes. *J. Phys. Chem. C* **2009**, *113*, 2405-2416.
222. Pardo-Yissar, V.; Katz, E.; Lioubashevski, O.; Willner, I. Layered Polyelectrolyte Films on Au Electrodes: Characterization of Electron-Transfer Features at the Charged Polymer Interface and Application for Selective Redox Reactions. *Langmuir* **2001**, *17*, 1110-1118.
223. Bradbury, C. R.; Zhao, J. J.; Fermin, D. J. Distance-independent charge-transfer resistance at gold electrodes modified by thiol monolayers and metal nanoparticles. *J. Phys. Chem. C* **2008**, *112*, 10153-10160.